Investigation of Novel Configurations for High Power Microwave Generation

by

David Michael French

A dissertation submitted in partial fulfillment
of the requirements for the degree of
Doctor of Philosophy
(Nuclear Science)
in the University of Michigan
2011

Doctoral Committee:

Professor Yue Y. Lau, Co-Chair
Professor Ronald M. Gilgenbach, Co-Chair
Professor Michael D. Uhler
Assistant Professor John E. Foster
Donald A. Shiffler, Air Force Research Laboratory

For Mom and Dad

ACKNOWLEDGEMENTS

This thesis has been the work of many dedicated and talented people. I would like to begin by thanking Professors Y.Y. Lau and Ron Gilgenbach for letting me work with them on the research projects in this thesis. These professors have a theoretical and experimental research program that is unmatched and I am glad that I could be a part of it. I would like to thank Professor Michael Uhler from the Biochemistry department who was instrumental in completing the first experiments for this thesis. I would also like to thank Professor John Foster who was an excellent instructor for the plasma courses and was a welcome addition to my committee.

My coworkers in the lab: Dr. Nick Jordan, Dr. Brad Hoff, Matt Gomez, and Jacob Zier helped with a lot of the research in this thesis, as well as some that did not make it. Mark Perrault does all the behind the scenes work in the lab and nothing would get done without him. Much of this thesis work took place working alongside the new generation of students: Matt Franzi, Ian Rittersdorf, and David Simon.

I met a lot of great people at Air Force Research Laboratory during my summer internships and would like to thank Dr. Keith Cartwright, Dr. Susan Heidger, and Dr. Don Shiffler for being such great bosses. Dr. John Luginsland has been a great coworker, mentor, and friend throughout my time in graduate school and helped in little ways on

many of the projects that I worked on. Dr. Lars Ludeking from ATK was a great help with the MAGIC code which seems to have been used on almost everything I have done.

The students that came before me and helped me along with my coursework Dr. Wilkin Tang and Dr. Du Pengvanich were a great help. I had fun taking courses and hanging out with students from the other plasma labs: Chris McGuffy, Will Schumaker, Aimee Hubble, Eric Gilman, Brad Sommers, Ben Yee, Brandon Weatherford, and Paul Cummings.

I thank God for my wonderful family who has given me love and support throughout my time in graduate school. My parents, Alice and David, have always been there for anything I have ever needed. My brother Joey has always answered my phone calls to talk about the latest movie, TV show, book, or random girlfriend. My sister Colleen is off traveling the world with her family and has kept the grandkid heat off of me so I could finish school.

This research was supported by an NDSEG Fellowship, Air Force Office of Scientific Research, AFOSR-MURIs, Air Force Research Laboratory, Office of Naval Research, L-3 Communications Electron Devices, and Northrop-Grumman Corporation, and AFOSR support of the MAGIC Users Group administered by ATK Mission Systems.

TABLE OF CONTENTS

LIST OF FIGURES

LIST OF TABLES

CHAPTER 1

INTRODUCTION

Most definitions of high power microwaves (HPMs) cover the range of frequencies from 0.3-30 GHz, and power levels ranging from 1 MW to 10s of GW [1-3]. This differentiates HPM from commonplace microwaves with power levels ranging from 10^{-3}-10^{4} watts used for applications such as cooking, radar, signal broadcast, cellular telephones, and communication systems.

Applications of HPM include radar, power beaming, heating of fusion plasmas, particle accelerators, and directed energy [1-3]. HPM based radar has advantages such as narrow bandwidth, high power, and short pulses that allow for small targets to be identified from large distances. RF tomography applications include ground penetrating radar (GPR) [4] which could be used for mapping the location of improvised explosive devices (IEDs) in combat. Power beaming is an application that would allow for the efficient transfer of power from one location to another without the need for power transmission lines [5]. Space solar power (SSP) systems would use a geosynchronous orbiting power station that collects power using large arrays of solar panels and beams the power back to earth in the form of microwaves. The power, 10 GW in some concepts, could be beamed to a receiving station a few km in diameter. In contrast, a 2 GW ground based solar power plant would be

approximately 7.5 x 7.5 km using the scaling from the largest solar plant currently in the US, the DeSoto Next Generation Solar Energy Center [6]. A key difference between these two solar generation methods is the capacity factor, average/peak power. Ground based solar plant capacity factor is typically 25% whereas for space based it is over 90%, the space based systems therefore can provide significantly more energy than ground based plant. Thermonuclear fusion requires temperatures sufficiently high that particles undergoing collisions have energies such that their distance of closest approach can surpass the Coulombic barrier and come within range of the strong nuclear force. In typical deuterium tritium plasmas in magnetic confinement fusion devices, this requires a temperature on the order of 10 keV or 116 million degrees Celsius. In order to achieve the requisite temperatures, cyclotron resonance heating can be used to transfer energy from a circularly polarized microwave beam to electrons or ions in a magnetized fusion plasma. ITER, the newest large tokamak fusion device currently being built in France, will use an array of gyrotrons to produce 24 MW of 170 GHz microwave radiation to be used for electron cyclotron resonance heating of the plasma [7]. Large scale nuclear physics experiments such as the search for the Higgs boson at the Large Hadron Collider (LHC) [8] and next generation light sources such as the Linac Coherent Light Source (LCLS) [9] at SLAC require high energy particle beams. High energy particle accelerators such as the LHC [10] or the SLAC linac require high microwave power to drive particles to high energy.

High power microwaves are typically generated with a vacuum electronic device [1-3]. These devices generate microwaves by the interaction of an energetic electron beam with a wave, where the interaction leads to a transfer of energy from the beam to the wave. Most

HPM devices are pulsed as the power levels are sufficiently high that no continuous power supplies exist. The pulsed power driver stores energy over a time period of seconds to minutes and releases the energy over a time period of nanoseconds to microseconds. The compression in time leads an increase in power to MW or GW levels, enabling the production of very high power electron beams. In these devices, the electron beam is accelerated by applying a large pulsed DC voltage, typically 10s-100s of kV. The electron beam currents in these devices range from 0.1-10s of kA. The beam-wave interaction in the HPM device occurs in one of several ways. In the case of the Vircator (VIRtual CAthode oscillaTOR) [11], a very high current electron beam guided by a magnetic field is injected into an interaction cavity. If the current exceeds the space charge limited condition (Child-Langmuir current [12],[13]) an oscillating space charge wave at a frequency approximately equal to the relativistic plasma frequency will be generated. The electron plasma oscillations produce high power microwave radiation in the cavity. The klystron is a linear beam device which can be used as an oscillator or amplifier [14]. The klystron uses a ballistic electron beam guided by a magnetic field which passes a microwave cavity driven by a small amplitude input signal. The oscillating electric field of the cavity leads to modulation of the beam. Subsequent "buncher" cavities will be driven by the modulated beam and reinforce the AC current of the beam. Microwave power is extracted from the final cavity driven by the heavily modulated beam, thus the input signal can be amplified to high power levels. In an oscillator configuration the cavities can be coupled together such that some of the output is fed back into the input of the device and the klystron can be made to oscillate at a specific frequency. The gyrotron [15] uses a rotating annular electron beam which, upon entering an

increasing magnetic field along the propagation direction, is adiabatically increased in perpendicular velocity at the expense of linear velocity. Due to beam instabilities covered in depth in Chapter 3, the beam bunches azimuthally. The rotating charge bunches transfer energy to a rotating electric field. This produces microwave radiation at high frequency, up to 100s of GHz. The magnetron [16] is a crossed-field device which uses an electron beam rotating in crossed electric and magnetic fields to transfer energy to microwaves by interacting with a corrugated slow wave structure. The slow wave structure slows down the microwaves such that they co-move with the electrons and the electrons can give up energy to the waves. The operation of the magnetron will be covered in depth in Chapter 2. A new type of HPM device is the nonlinear transmission line (NLTL) [17-19]. The NLTL is a solid state HPM source which requires no vacuum, electron beam, or guiding magnetic field. In the NLTL, a high power pulse is injected into a dispersive transmission line containing nonlinear elements. The nonlinear interaction leads to electromagnetic shockwave formation at the leading edge of the pulse [20]. Energy is transferred to an RF wave that co-moves with the shockwave as it travels down the transmission line. The NLTL may have a number of advantages over existing vacuum electronic based HPM sources and is discussed in depth in Chapter 4.

In Chapter 2 the basic theory of electron behavior in the presence of magnetic and electric fields is covered. This behavior will lead to the discussion of magnetron operation. Discussion of the operation of the magnetron will lead to the introduction of the recirculating planar magnetron. Chapter 3 will introduce the negative mass instability and detail a comprehensive analysis of the beam dynamics and stability in crossed-field devices.

Chapter 4 introduces the nonlinear transmission line (NLTL) and proceeds to show the results of experiments and simulations on three different NLTLs. Chapter 5 summarizes work on bioelectromagnetism, a nonstandard HPM application. The electroporation experiments undertaken in Chapter 5 essentially use a single cycle HPM pulse for the manipulation of biological cells. Chapter 6 summarizes the thesis and outlines future work.

CHAPTER 2

RECIRCULATING PLANAR MAGNETRON

2.1 Electron Motion

The motion of electrons acted on by electric and magnetic fields is governed by the Lorentz force equation,

$$\vec{F} = q\left[\vec{E} + \vec{v} \times \vec{B}\right]. \tag{2.1}$$

We begin with the motion of a particle of mass m and charge q in the presence of a uniform magnetic field B oriented along the $+\hat{z}$ axis an electron will execute a circular orbit in the $\hat{x} - \hat{y}$ plane with angular frequency of $\omega_c = qB/m$, the cyclotron frequency. The centripetal acceleration of the electron in an equilibrium orbit, $a_{centipetal} = v^2/r$, is balanced by the acceleration from the force of the magnetic field given by equation (2.1), $a_{v\times B} = qvB/m$. The equations of motion for the charged particle are

$$\frac{dv_x}{dt} = \frac{qB}{m} v_y,$$
$$\frac{dv_y}{dt} = -\frac{qB}{m} v_x. \tag{2.2a,b}$$

Differentiating equation (2.2a), substituting from (2.2b) to put in terms of v_x and realizing $\omega_c = qB/m$

$$\frac{d^2 v_x}{dt^2} + \omega_c^2 v_x = 0. \tag{2.3}$$

The solutions for v_x and v_y are

$$\begin{aligned} v_x &= v_\perp \sin(\omega_c t + \phi), \\ v_y &= v_\perp \cos(\omega_c t + \phi), \end{aligned} \tag{2.4}$$

where $v_\perp$ is the particle's tangential velocity and ϕ is an arbitrary initial phase. Integrating equations (2.4) from x_0, y_0 to x, y and choosing $\phi = 0$ gives the coordinates of the particle at time t,

$$\begin{aligned} x - x_0 &= -\frac{v_\perp}{\omega_c} \cos(\omega_c t), \\ y - y_0 &= \frac{v_\perp}{\omega_c} \sin(\omega_c t). \end{aligned} \tag{2.5}$$

The x and y coordinates define a circular orbit. The radius of the orbit is

$$r_L = \frac{v_\perp}{\omega_c} = \text{Larmor radius} \tag{2.6}$$

Equation (2.5) describes a charged particle with a circular orbit centered at (x_0, y_0). Carrying out this analysis for a charged particle in a finite electric field will lead to the basic description of the single particle dynamics in a crossed-field device, the $E \times B$ drift.

Considering the force on a charged particle given by equation (2.1) with an electric field E_x the equations of motion become

$$\frac{dv_x}{dt} = \frac{q}{m}E_x + \omega_c v_y,$$
$$\frac{dv_y}{dt} = 0 - \omega_c v_x. \tag{2.7a,b}$$

Differentiating (2.7a) while assuming E_x is constant and substituting (2.7b) gives

$$\frac{d^2v_x}{dt^2} = -\omega_c^2 v_x, \tag{2.8}$$

whose solution is

$$v_x = v_\perp \sin(\omega_c t + \phi),$$
$$v_y = v_\perp \cos(\omega_c t + \phi) - \frac{E_x}{B}, \tag{2.9}$$

where the last expression for v_y is obtained from (2.7a), using the solution for v_x. This analysis shows that in addition to the circular orbit there will be an additional constant velocity of E_x/B in the $-\hat{y}$ direction, known as the $E \times B$ drift.

To find the $E \times B$ drift in general we write, $\vec{v} = \vec{v}_0 + \vec{v}_1$ where $\vec{v}_0$ is a constant and $\vec{v}_1$ describes the Larmor orbit motion,

$$\frac{d\vec{v}_1}{dt} = \frac{q}{m}\{[\vec{E} + \vec{v}_0 \times \vec{B}] + \vec{v}_1 \times \vec{B}\}. \tag{2.10}$$

To solve for the drift motion, $\vec{v}_0$, we then set $[\vec{E} + \vec{v}_0 \times \vec{B}] = 0$. Taking the cross product with $\vec{B}$ gives

$$\vec{E} \times \vec{B} = \vec{B} \times (\vec{v}_0 \times \vec{B}) = \vec{v}_0 B^2 - \vec{B}(\vec{v}_0 \cdot \vec{B}). \quad (2.11)$$

The second term on the right side is equal to zero for motion transverse to $\vec{B}$, thus the drift motion is given by

$$\vec{v}_0 = \frac{\vec{E} \times \vec{B}}{B^2} \equiv \vec{v}_{E\times B}. \quad (2.12)$$

The $E \times B$ drift, $v_{E\times B}$, is the guiding center drift velocity of a charged particle in crossed electric and magnetic fields. The drift velocity depends only the electric and magnetic fields, it is independent of charge, mass, and cyclotron motion. The $E \times B$ motion of the particle is of crucial importance for examining the behavior of particles in the magnetron. This is the velocity component that must couple to the RF wave so that microwaves can be generated.

2.2 Electrons in a Crossed-Field Gap

The behavior of electrons in the crossed-field gap shown in Figure 2-1 with anode-cathode spacing of D voltage of V in a uniform magnetic field B can easily be determined from the above analysis.

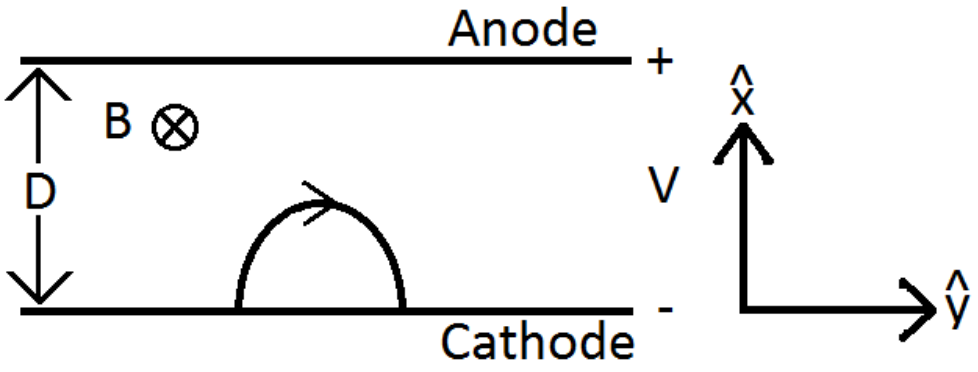

Figure 2-1. Basic crossed-field system

Using the boundary condition that the particle leaves the cathode with zero initial velocity the particle's velocity in $\hat{y}$ is given by

$$v_y = \frac{E_x}{B}[1 - \cos(\omega_c t)]\,. \tag{2.13}$$

Since $\dot{v}_y = \omega_c v_x$, this can be integrated to find the position in $\hat{x}$

$$x = \frac{v_y}{\omega_c} = \frac{1}{\omega_c}\frac{E_x}{B}[1 - \cos(\omega_c t)]\,. \tag{2.14}$$

x is maximized when $\cos(\omega_c t) = -1$, the maximum value of x for the geometry in Figure 2-1 is D. To solve for the voltage at which the electron will just touch the anode, the electric field, $E = V/D$, is substituted into equation (2.14) and the electron position, x, is set to its maximum value of D which occurs when the bracketed term is equal to 2,

$$x_{max} = D = \frac{2}{\omega_c}\frac{V_H/D}{B}. \tag{2.15}$$

V_H is known as the Hull cutoff voltage, given equation (2.16) below, and plotted in Figure 2-2 as a function of B.

$$V_H = \frac{1}{2}B\omega_c D^2 = \frac{1}{2}\frac{m}{e}(\omega_c D)^2. \tag{2.16}$$

When the voltage is less than the Hull cutoff voltage electrons leaving the surface of the cathode will be unable to reach the anode due to "magnetic insulation", $V < V_H$. Magnetic insulation is used to prevent electrons from crossing from cathode to anode in a number of high power devices that lack conventional insulation such as a liquid, gas, or solid dielectric layer. Magnetically insulated transmission lines are used in systems requiring low

impedance power transmission [21] and microwave devices such as the magnetically insulated line oscillator (MILO) [22] and magnetron [16] operate under magnetic insulation.

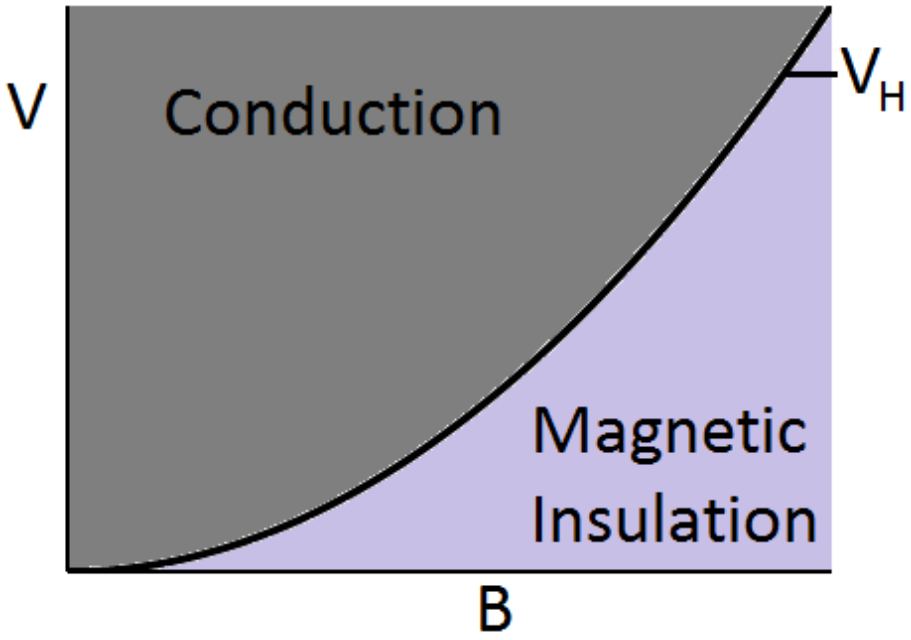

Figure 2-2. Plot of V_H as a function of B. Operation in the dark shaded region allows electrons to move from cathode to anode. In the light shaded region electrons emitted from the cathode will be unable to reach the anode.

2.3 Magnetron

The magnetron oscillator is a vacuum electronic device in which electron transport takes place in crossed electric and magnetic fields. Figure 2-3 shows diagrams of conventional cylindrical and planar magnetrons. In the magnetron, electrons emitted from the cathode are insulated from reaching the anode by the presence of a magnetic field, Figure 2-3. The electrons execute an $E \times B$ drift parallel to the surface of the cathode. The slow wave structure (corrugations on the anode) will cause RF waves to travel at a velocity much lower than c, the speed of light. The presence of the slow wave structure leads to an

RF electric field with a component parallel to the cathode surface. If the velocity of the wave coincides with the $E \times B$ motion of the electrons, the electrons can transfer energy to the wave as they move from a region of high potential energy (near the cathode) to a region of low potential energy (near the anode). The physical mechanism is that the tangential RF electric field, together with the external magnetic field, provides a $E_{RF} \times B$ drift from cathode to anode which brings the electrons to the anode. The potential energy lost by the electron is converted to RF energy [16],[23]. The magnetron device therefore converts electron potential energy to energy in an RF wave as the electron moves from cathode to anode.

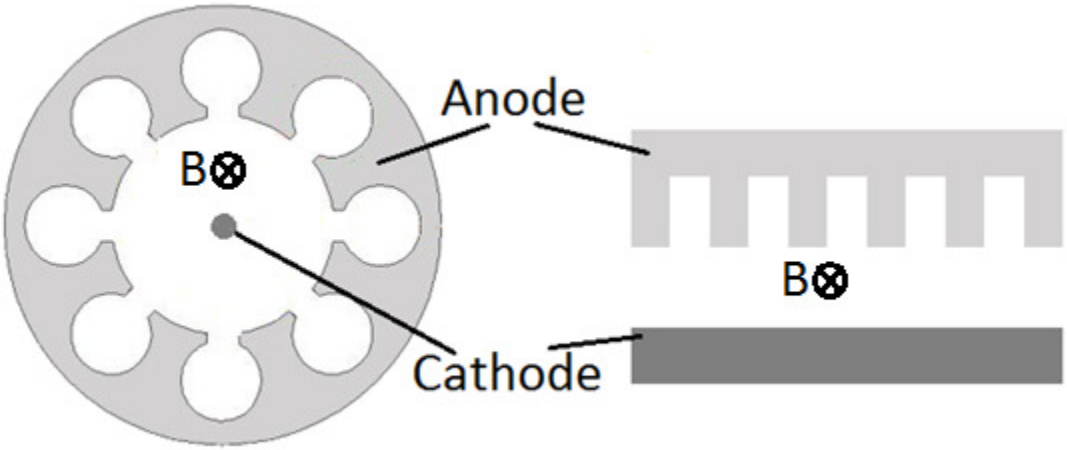

Figure 2-3. Conventional cylindrical magnetron (left) with the cathode in the center and the anode on the outside. Planar magnetron (right).

2.4 Buneman-Hartree Condition

The synchronism of electrons and RF wave is known as the Buneman-Hartree condition [1],[16],[23],[24]. The phase velocity of a wave in the crossed-field gap is $v_{ph} = \omega/k$. In the moving frame of the wave the initial energy of an electron is $E_{initial} = \frac{1}{2}mv_{ph}^2$.

E_{final} consists of the energy associated with the potential drop from the initial to final location added to the work done by the Lorentz force in moving the electron from the cathode to the anode, $W = F_{lorentz}D$, where D is the anode-cathode gap. The final energy is, $E_{final} = 0 - eV + \left(ev_{ph}B\right)D$, if the electron is trapped by the wave, i.e. the electron co-moves with the wave; so that its final velocity is zero in the frame of the wave. Equating the initial and final energies, the voltage in terms of the magnetic field B, the anode-cathode gap D and the phase velocity of the wave, v_{ph}, gives $V = V_{B-H}$, the Buneman-Hartree voltage,

$$V_{B-H} = v_{ph}BD - \frac{1}{2}\frac{m}{e}v_{ph}^2. \tag{2.17}$$

Equation (2.17) is Buneman-Hartree condition for synchronicity between the electron and wave in a magnetron. The Buneman-Hartree line is plotted along with the Hull cutoff line in Figure 2-4. The region of magnetron operation is shown in the gray region. Below this region no oscillation will occur because the electrons will not be traveling in synchronism with the RF wave. Above this region the electrons are not magnetically insulated and will travel from cathode to anode without undergoing a circular orbit, therefore these electrons are unable to participate in energy transfer to the RF wave.

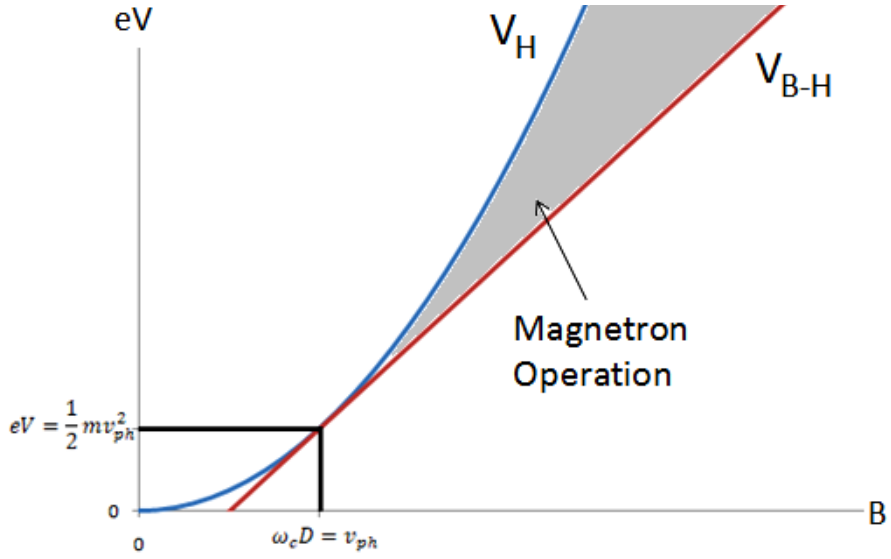

Figure 2-4. Plot showing the Hull cutoff voltage and Buneman-Hartree voltage and the region of magnetron operation in gray.

2.5 Operational Considerations

There are several limiting characteristics of existing magnetron designs. One disadvantage of the conventional cylindrical magnetron is the small cathode size. This limits the electron current that can be drawn, thus limiting the total power the magnetron can produce. Another disadvantage of the conventional magnetron that limits the absolute energy efficiency is endloss current. Endloss current is the electron current that moves from cathode to anode outside of the interaction region along the external magnetic field lines, as shown in the left pane of Figure 2-5. The electrons that escape the interaction region do not contribute energy to the RF wave, however, they do contribute to the total current that moves from cathode to anode, and hence represents a significant DC power loss. This power loss can be appreciable in relativistic magnetrons. Figure 2-6 shows entrance current, endloss current, voltage, and total power from a shot on the UM relativistic magnetron

experiment [25]. Prior to the startup of microwave emission in the magnetron (green trace), virtually all of the current (purple trace) drawn by the system is endloss current (gray trace). Endloss current can be nearly eliminated in the inverted magnetron configuration, right pane of Figure 2-5, where the cathode and anode positions are reversed. Since the grounded cathode is on the outside of the anode structure, electrons that leave the interaction region will return to another part of the grounded structure, therefore they do not contribute to power drawn by the magnetron. The inverted design therefore may have substantially higher absolute energy efficiency than the conventional design. This represents a significant advantage of the inverted magnetron, particularly in compact configurations where large current losses are unacceptable.

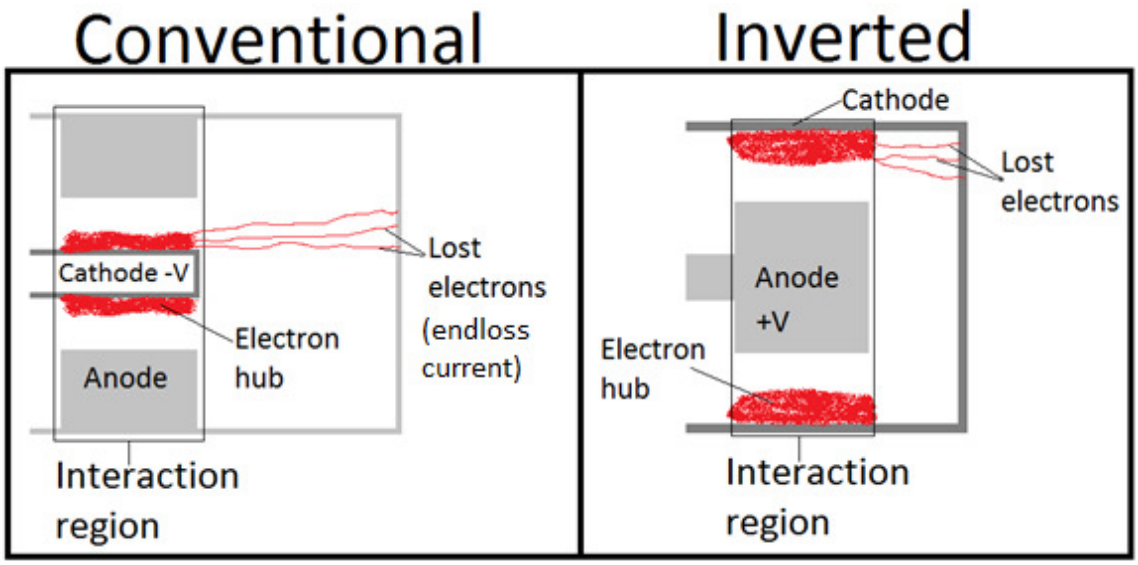

Figure 2-5. Diagrams for conventional and inverted magnetrons showing the path of electrons lost from the interaction region. Lost electrons do not draw power in the inverted configuration.

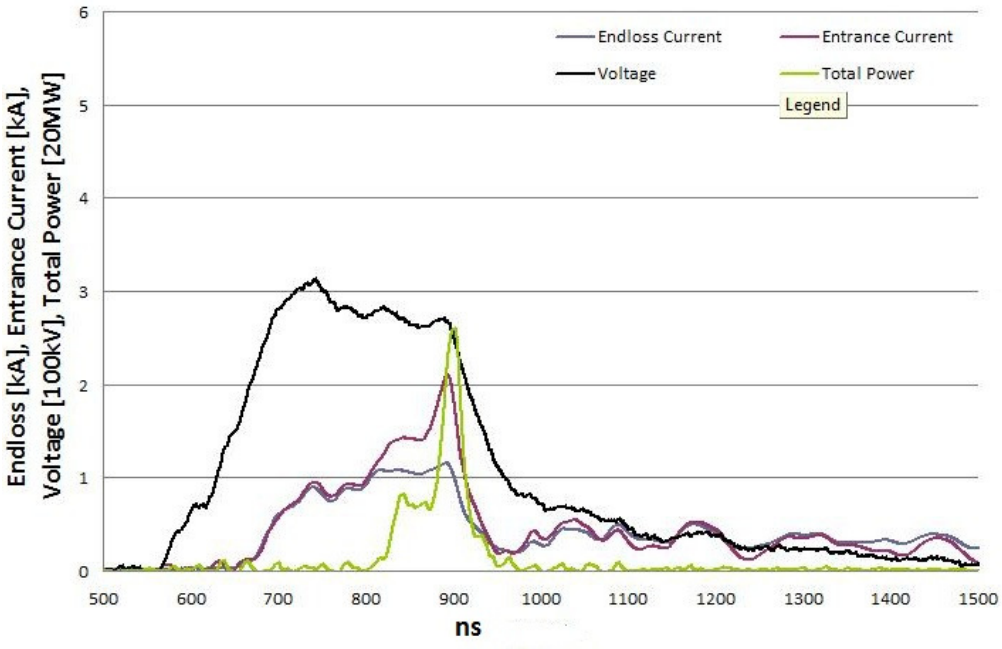

Figure 2-6. UM relativistic magnetron shot #12446 data showing the endloss current (blue) accounts for a large fraction of the total current (brown).

The planar magnetron, Figure 2-3 (right), has the advantage of very large cathode and anode areas. The large area cathode can provide substantial current without the need for exotic high current density cathodes. The large anode area allows for simple thermal management if needed for high power operation. Additionally, there are many options for extracting power from the planar magnetron. There is substantial access to the anode structure, therefore virtually any extraction technique can be used on the planar magnetron. A significant disadvantage of the planar magnetron is its inherent single pass operation. There is no recirculation of electrons or microwave energy in contrast to the cylindrical magnetron which recirculates both electrons and microwaves. The electron beam is dumped at the end of the planar magnetron; therefore, a substantial fraction of the total current drawn from the cathode is wasted since it does not contribute to RF generation.

Considering the advantages of planar and cylindrical magnetrons, a new design that combines the advantageous features of existing magnetrons promises to eliminate many of the disadvantages of the existing designs.

2.6 Recirculating Planar Magnetron

The recirculating planar magnetron (RPM) [26] seeks to maximize the advantages of existing magnetron designs by combining the geometries of the planar and cylindrical magnetrons. There are two different basic designs in which a recirculating planar magnetron can be realized, the axial B-field and radial B-field [26]. The axial B-field RPM is comprised of two planar magnetrons on opposite sides of a common oval shaped anode (inverted, Figure 2-7) or cathode (conventional, Figure 2-8). The short circular sections on each side of the RPM connect the two planar magnetrons to form a single RF circuit allowing the RF wave to travel from one planar magnetron to the other.

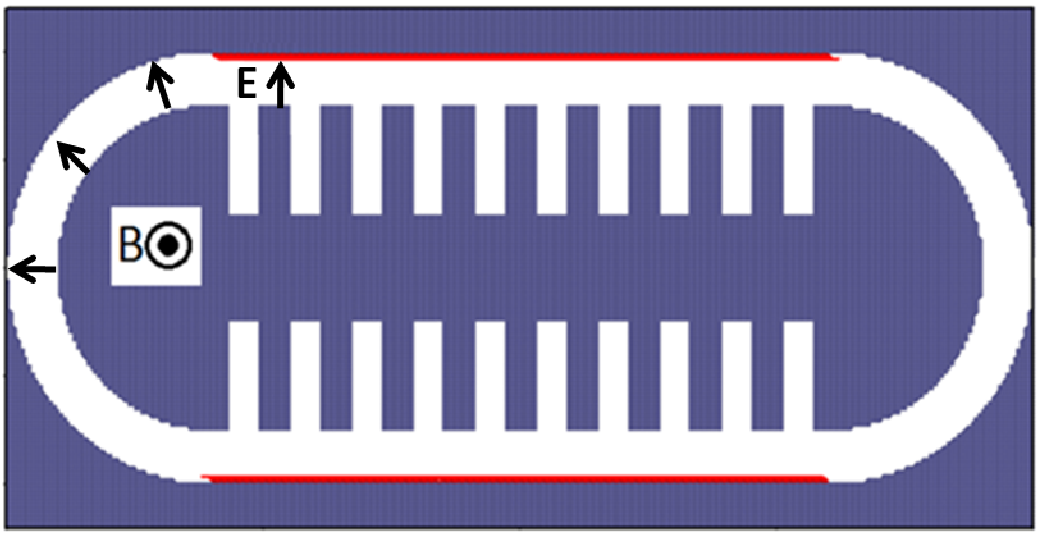

Figure 2-7. Inverted axial B-field RPM with the anode slow wave structure in center and large cathode area on outside.

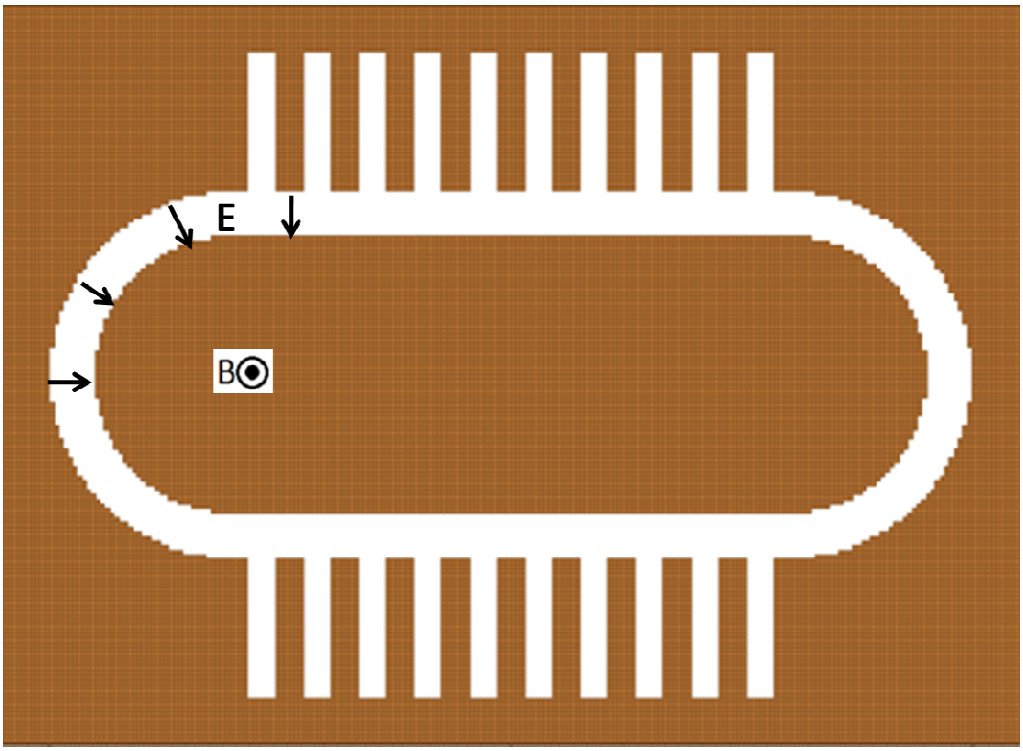

Figure 2-8. Conventional axial B-field RPM with anode slow wave structure on the outside of a central cathode.

Since the RPM has a common anode and cathode for the two planar magnetrons as well as in the bends, magnetic insulation insures that the cathode electron flow is recycled from one planar magnetron into the other. This is in contrast to a non-reentrant planar magnetron design where the electron flow is dumped at the end of the magnetron leading to decreased energy efficiency.

The radial B-field design is different in that it uses a single planar magnetron section that is circular in shape with vanes oriented radially. This design uses a radial magnetic field, which can be provided by permanent magnets, and an axial electric field. The geometry of the radial B-field RPM is shown in Figure 2-9. The left pane shows the field orientations and the direction of $E \times B$ electron flow around the circular device. The right

pane of Figure 2-9 shows the field orientations and anode and cathode in a slice of the circle where the anode slow-wave structure is on the top and the cathode is at the bottom. In this version of the RPM, the number of cavities can be adjusted by changing the radius of the device. The simple anode design can be much more easily manufactured out of a single piece of material than in some conventional designs which require that multiple pieces be brazed together. This can allow for significantly tighter manufacturing tolerances which is crucial for high frequency operation. A variation of the radial B-field design is the racetrack geometry, shown in Figure 2-10. In this configuration the two planar magnetron sections are situated adjacent to each other. This is unlike the axial B-field configuration where the two planar magnetrons are on opposite sides of a common anode or cathode. In the racetrack geometry the two planar magnetrons are connected by circular planar sections in which the radial magnetic and axial electric fields guide the electrons around the bends in the same way as the radial B-field design. This design may have advantages in certain cases over the standard circular RPM.

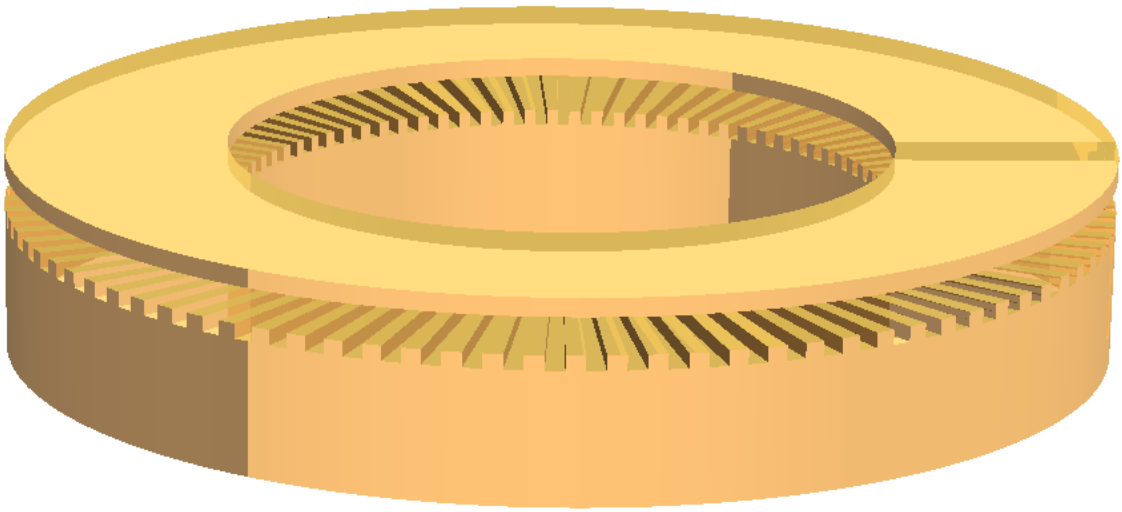

Figure 2-9. Radial magnetic field RPM.

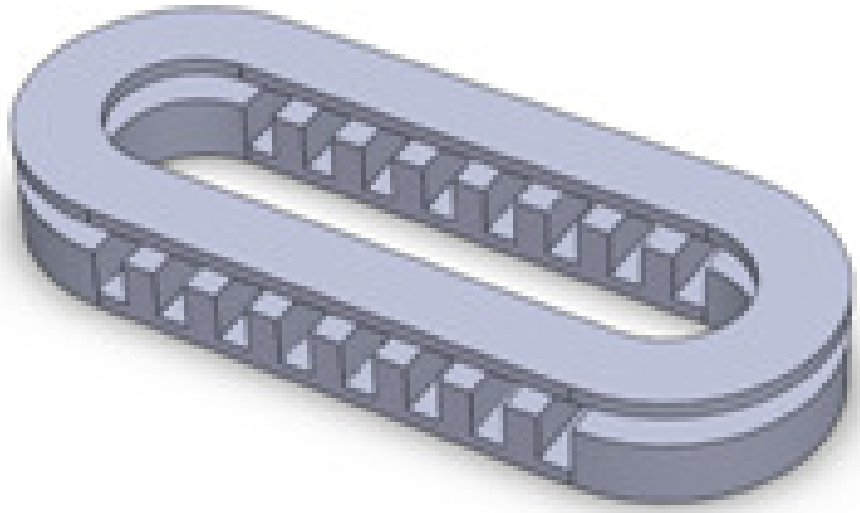

Figure 2-10. Racetrack RPM.

2.7 RPM Advantages

The RPM design has several advantages over existing magnetron designs. The large area cathode in the RPM allows for substantial electron current to be drawn from the cathode at low current density. The large cathode area therefore reduces the requirement for high current density cathodes. Some of the high current density experimental cathodes previously developed at UM such as the metal oxide junction MOJ cathodes [27] have a useful service life of only 10s of shots, requiring frequent service. Instead, a long lifetime cathode can be used, increasing the useful service life of the magnetron. The large anode area of the RPM provides many options for thermal management if high average power operation is desired. In addition, the planar anode design can simplify the manufacturing of the slow-wave structure. Since the structure can be machined from a single piece of material, very high levels of manufacturing tolerance are possible, an important concern for high frequency magnetrons with small structure size. The inverted axial B-field geometry also has the advantage of minimizing the endloss current since electrons lost from the interaction region can travel along magnetic field lines and return to ground. Due to the orientation of the electric and magnetic fields in the cylindrical portion of the inverted RPM, the electrons have a tendency to bunch as a result of the negative mass instability [28]. This tendency for bunching can greatly reduce the startup time of the RPM in the inverted configuration in comparison to the conventional configuration and will be examined in greater detail in Chapter 3.

2.8 Simulations

Proof-of-concept simulations of the axial B-field RPM were performed in MAGIC2D [29] to determine if electrons would be recirculated around the bends and if the RPM would start oscillation and form spokes. Due to the lack of a slow wave structure around the bends, it was unclear if electron spokes would persist due to the difference in velocity of the wave, $\sim c$, and the electron velocity, $\sim E/B$. The first simulations were carried out on the inverted RPM with subsequent simulations on the conventional, axial B-field RPM. Simulations of the radial B-field RPM in MAGIC were performed by Brad Hoff [26]; a synopsis of this work is included in section 2.14.

2.9 Inverted Axial B-Field RPM

The first simulations of the RPM were done on the geometry of Figure 2-7. The parameters of this simulation were made to be close to those of a MELBA type experiment [30] with a uniform 2.25 kG magnetic field and a voltage of 200 kV. The anode cathode gap is 1 cm, the slow wave structure consists of 10 slots 6 mm wide 2 cm deep on each side of the anode. Electrons are emitted using explosive emission with a threshold field of 100 kV/cm. The emission region is restricted to the flat regions opposite the vanes of the slow wave structure. In an actual device this region could be patterned or be covered in field or thermionic emission surfaces [31]. This inverted RPM started oscillating in less than 10ns in this idealized 2D simulation which had a voltage risetime of 0.25 ns; in order to shorten the runtime of the simulation. This proof-of-concept simulation showing that the RPM could

oscillate even though the two separate planar magnetrons are connected by nonresonant sections was a crucial step in realizing a functional RPM. The voltage across slot-5 was recorded to monitor the magnetron oscillation, slot-5 was chosen as it is in the center of the anode structure. Figure 2-12 shows the slot-5 voltage trace indicating that initial magnetron oscillation begins at approximately 5 ns with strong oscillation occurring by 10 ns. The spoke interaction with the vanes shown in Figure 2-11 is extremely strong with the spokes extending nearly to the base of the vanes by the end of the bottom planar magnetron; (electrons move clockwise). In this particular case, the top and bottom planar sections are out of phase such that the electron spokes appear different from top to bottom. Since the two planar sections are essentially independent there is no reason for them to run in the same mode or for any phase correlation between them. In principle this can be corrected by providing some type of communication between the two planar sections, such as coupling slots through the central anode. A fast Fourier transform (FFT) of the voltage signal plotted in Figure 2-12 is shown in Figure 2-13 indicating the peak π-mode oscillation at 3.09 GHz.

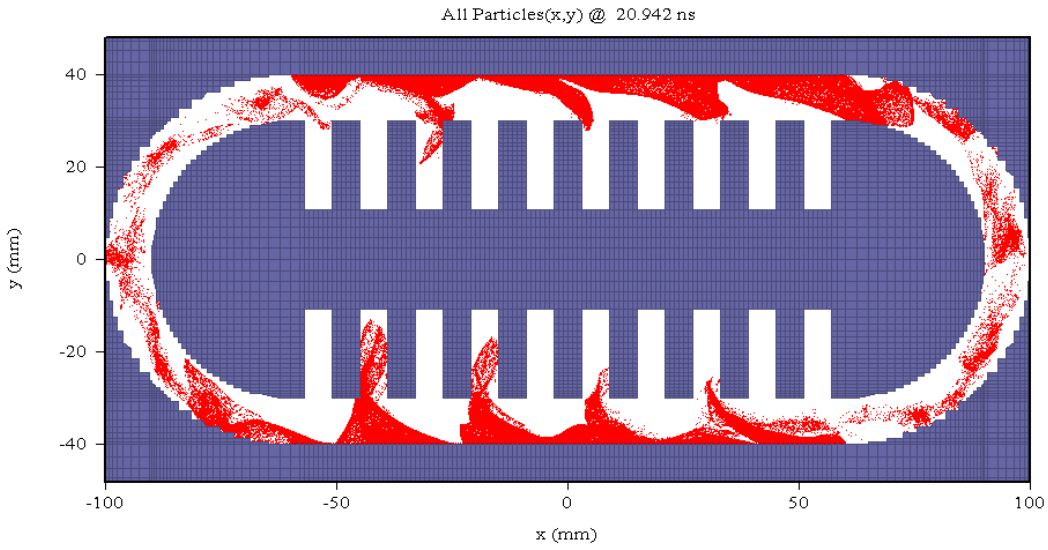

Figure 2-11. Inverted RPM oscillation primarily in π-mode, where spokes form in every other vane. Power extraction was included in later 3D simulations.

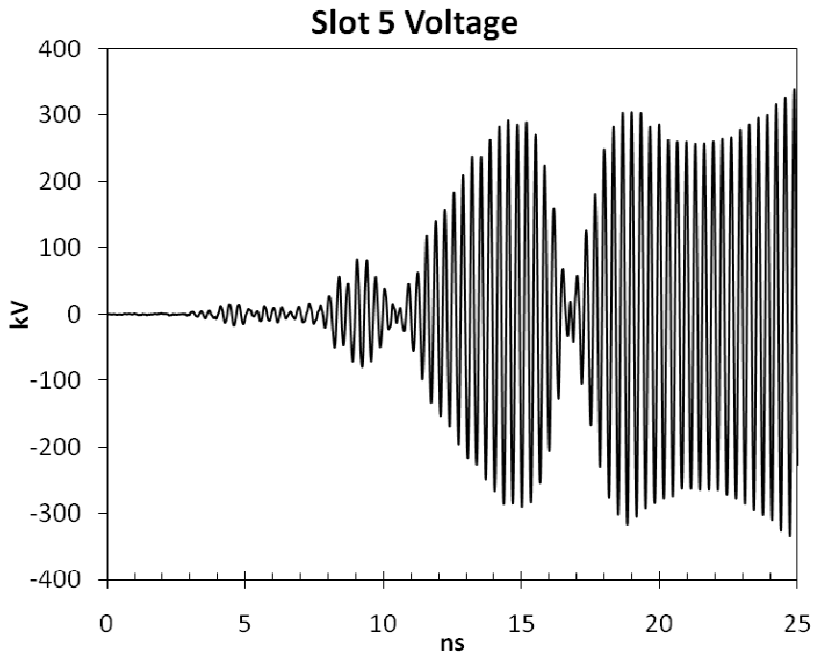

Figure 2-12. Voltage measured across slot-5 of the inverted RPM. Competition between the two planar sections is responsible for the large power fluctuations seen in the voltage trace.

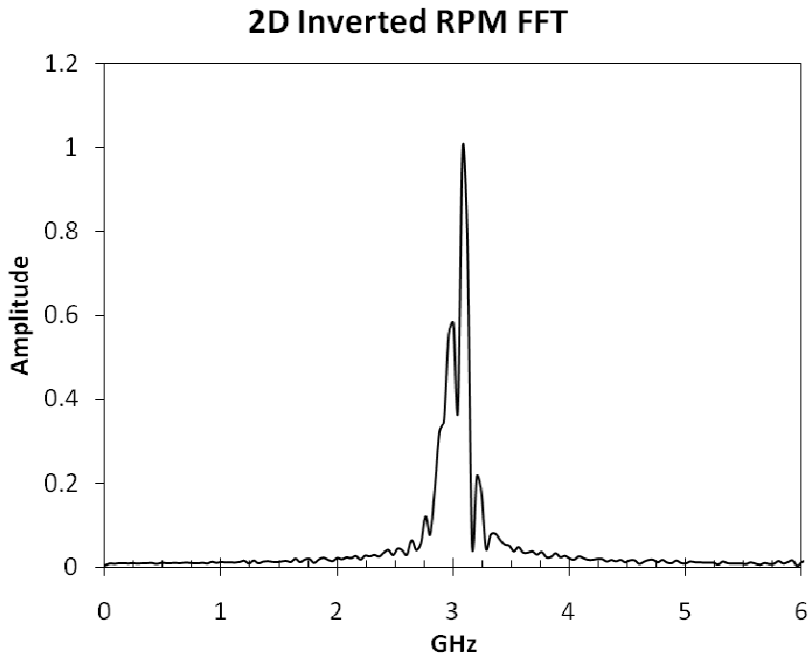

Figure 2-13. FFT of the slot-5 voltage signal showing a peak oscillation frequency of 3.09 GHz and some neighboring modes. The presence of these modes is likely the cause of the significant amplitude modulation seen in Figure 2-12.

2.10 3D Inverted Axial B-Field RPMs

Several different MAGIC3D [29] inverted RPM simulations were run in order to determine the feasibility of an axial extraction technique into a single waveguide. A challenge with 3D simulations is the long runtime of the simulation due to the large number of cells. Typical simulations would take several days to run on available computing resources. These simulations were typically run at very low resolution, often with only 3 cells across vanes, in order to have them run in a reasonable amount of time. Data generated from these simulations is therefore considered extremely preliminary and is used primarily in order to gauge the feasibility of a concept rather than acting as a design tool.

The first simulation on a 3D inverted RPM used a central waveguide inserted into the anode structure with coupling slots into vanes of the top and bottom planar sections. A slice of the anode structure showing coupling slots into the central axial waveguide is shown in Figure 2-14. Using an axial extraction technique for the inverted RPM is desirable as it allows for a very compact design. Typically, microwave extraction from relativistic A6 magnetrons is accomplished using radial waveguides from one or more, commonly three, of the anode cavities [2]. Radial extraction adds substantially to the size of the system. The use of multiple extraction points also requires that the power from these be combined before going to an antenna. This requires a substantial amount of waveguide plumbing and space to accomplish. Also, it necessitates the use of a Helmholtz type magnet system to generate a uniform magnetic field in the interaction region. The magnetic field in the case of axial extraction could be generated by a compact coil wrapped directly around the cathode so that outside dimensions are very close to that of the cathode dimensions. The smaller size of the magnet for this configuration may also allow the use of permanent magnets. Several different geometries using coupling slots into a central axial waveguide were simulated; the geometry of Figure 2-14 is outlined here. Figure 2-15 shows a 3D view of the entire RPM system with the front portion of the cathode block removed so that the anode and extraction waveguide are visible. The coupling slots from the anode into the central waveguide are visible in Figure 2-16. Fields from the slow-wave structure couple into the central waveguide which is terminated in a lossy load. The load used in MAGIC is a volume of "freespace." The conductivity of "freespace" is tapered and increases in the wave propagation direction in order to minimize reflections.

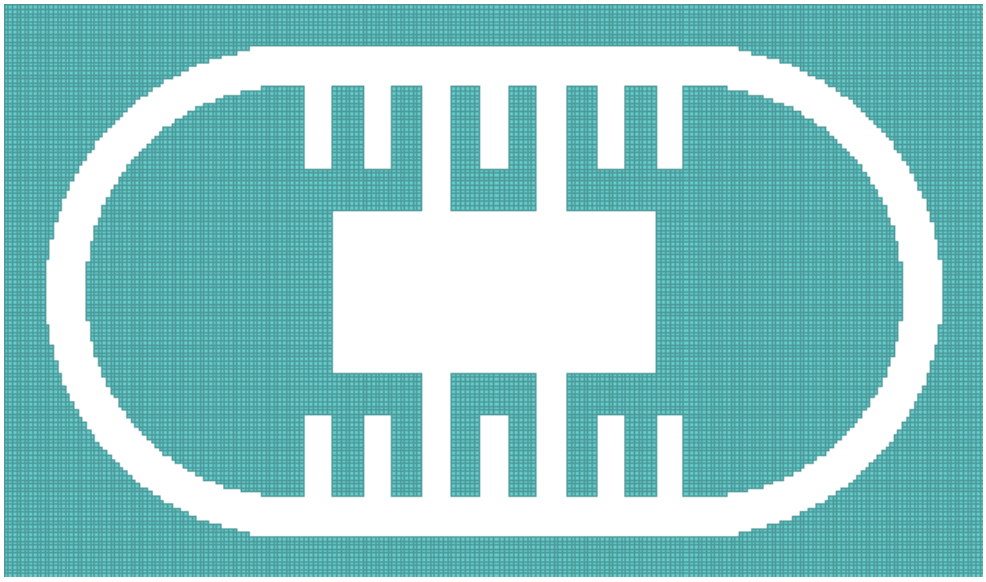

Figure 2-14. 2D slice of anode section of 3D inverted RPM showing the coupling slots into the central waveguide. The desired output mode is the fundamental TE_{10} rectangular waveguide mode.

In Figure 2-14 the slots from both the top and bottom slow-wave structures are coupled into the waveguide. In addition to extracting power from both the top and bottom planar magnetron sections, this allows for the planar magnetron sections to "talk" to one another such that they will be in phase. In most of the simulations with a central waveguide the waveguide was filled with "freespace" in both axial directions away from the coupling slots for easy evaluation of the power that was extracted into the waveguide. In practice, precise sizing of the waveguide behind the coupling slots, typically ¼ wavelength, would be necessary in order to properly and efficiently launch a mode down the extraction waveguide. The design of the slots used for power coupling is important to avoid breakdown in this region of high power density [32].

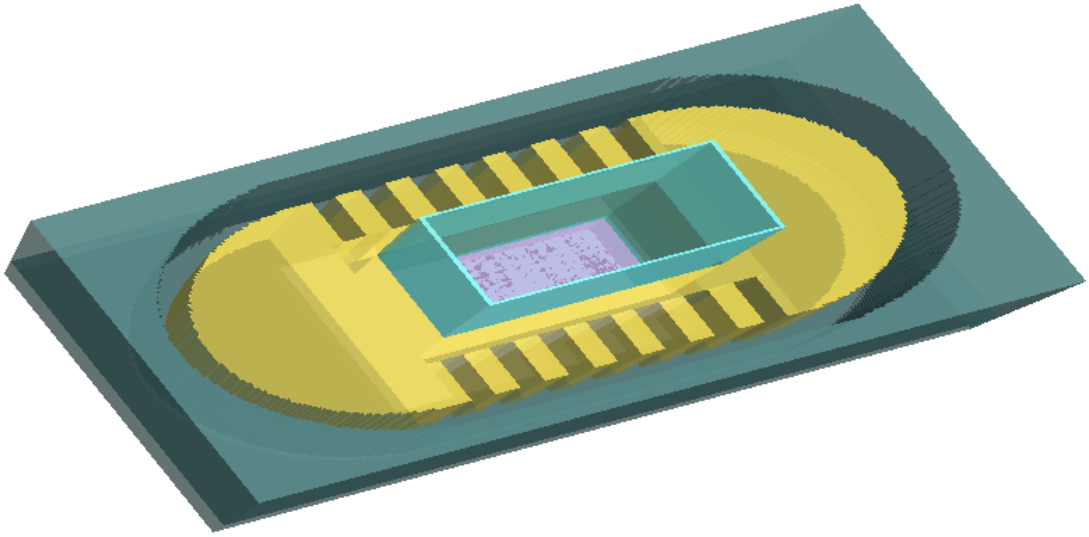

Figure 2-15. 3D perspective view of inverted RPM showing the cathode (blue) anode block (yellow) and axial extraction waveguide (light blue).

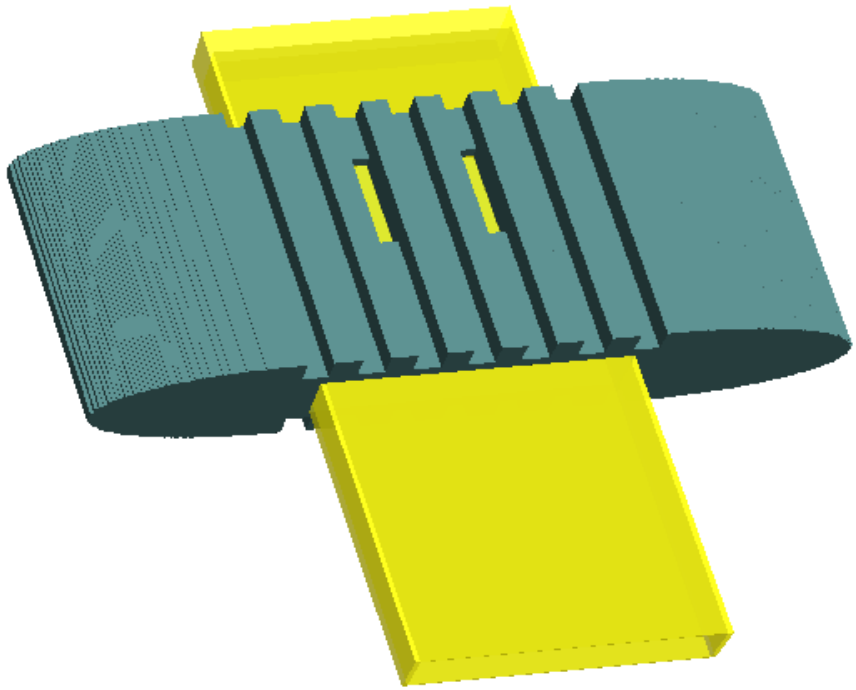

Figure 2-16. 3D perspective view of inverted RPM anode block (blue) coupling slots into the axial extraction waveguide (yellow) are visible in the slots to the left and right of the center slot.

There are several engineering challenges associated with this type of axial extraction method when used with an inverted magnetron. One method of operation is to maintain the cathode at ground potential and pulse the anode to a positive potential, Figure 2-17a. A problem with this approach is that the extraction waveguide will be at a large positive potential, connected directly to the pulsed power driver. A break in the waveguide will be necessary to extract the power from the waveguide without having the antenna and all other components connected to the waveguide being pulsed up to the anode potential. A break in the extraction waveguide will lead to reflections or breakdown in the region of the break due to the large fields that are present in an HPM extraction waveguide. Another method for operating the magnetron involves pulsing the cathode up to a large negative potential while keeping the anode at ground potential, Figure 2-17b. This method requires no breaks in the extraction waveguide, however, introduces several additional problems. Due to the 100s of kV on the cathode it would have to be surrounded by and insulated from a grounded shield. It could be insulated by either oil or vacuum. If it were insulated by oil, additional oil-vacuum interfaces would be necessary with their associated concerns about leaking and breakdown. If it were insulated by vacuum, the size of the device would be significantly increased in order to have a large enough gap between the cathode and the outer ground shield to avoid emission from the outside of the cathode. The increase in device size would necessitate larger magnetic field coils adding difficulty to producing the necessary magnetic field for magnetron operation. In this case electrons lost from the interaction region may move to a grounded region away from the anode drawing current from the device; therefore, electron endloss may be a concern.

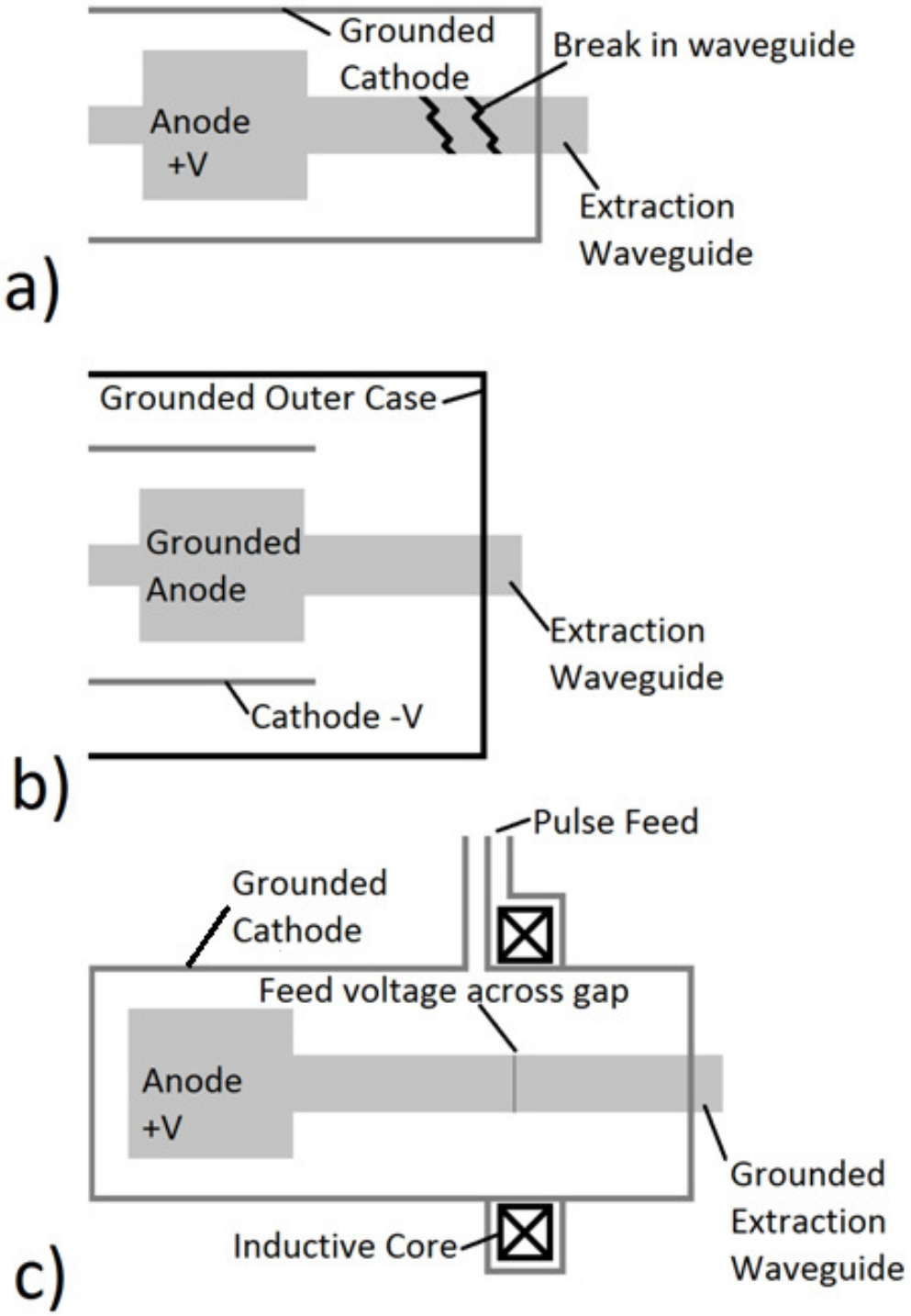

Figure 2-17. Axial waveguide extraction geometries.

An alternative method of driving the system could utilize inductive voltage adder technology [33] and eliminate several problems with the aforementioned driving techniques. With the extraction waveguide connected directly to the grounded cathode, the anode can be driven to a large positive potential on the extraction waveguide itself, Figure 2-17c. In this configuration the anode waveguide acts as the secondary winding of a transformer where the primary is the pulsed feed current around the inductive core. There will be a voltage drop on the waveguide across the core equal to the pulsed feed voltage. This configuration offers several advantages over configurations (a) and (b). Since the entire cathode structure is maintained at ground potential the electron endloss of configuration (b) is not a concern. The anode is driven to a high positive potential inside of the grounded cathode, therefore, the cathode shell requires no external grounded shell or the associated insulation. Since the waveguide potential goes to zero on the extraction side of the accelerator gap it can be passed through the outer case, also at ground potential, without the need for a break in the waveguide that could lead to reflections or breakdown. This type of driver for an axially extracted inverted magnetron offers many advantages over the other configurations and can use existing inductive accelerator technology such as that used in the Linear Transformer Driver (LTD) pulsed power drivers in an inductive voltage adder configuration [34].

2.11 Mode Launcher

A different type of extraction scheme involving axial extraction from an inverted configuration was tested in MAGIC 3D simulations. The mode launcher geometry was the

most successful technique in extracting power from an inverted RPM. This extraction technique uses the grounded cathode case as the extraction waveguide with a mode launched into it from the front of the anode. The anode design that was simulated is shown in Figure 2-18. The slow-wave structure is strapped for the π-mode on the top and bottom, with the top and bottom straps connected to alternating vane tips. Assuming the device runs in π-mode and the top and bottom are in phase, the top and bottom straps would be at opposite potentials. This would lead to an AC electric field between the two straps on the front of the anode structure. The AC field leads to an electromagnetic mode being launched off the front of the anode structure down the cathode case. The cathode case size was apertured down to a rectangular waveguide in an attempt to launch a fundamental TE_{10} mode, shown in Figure 2-19.

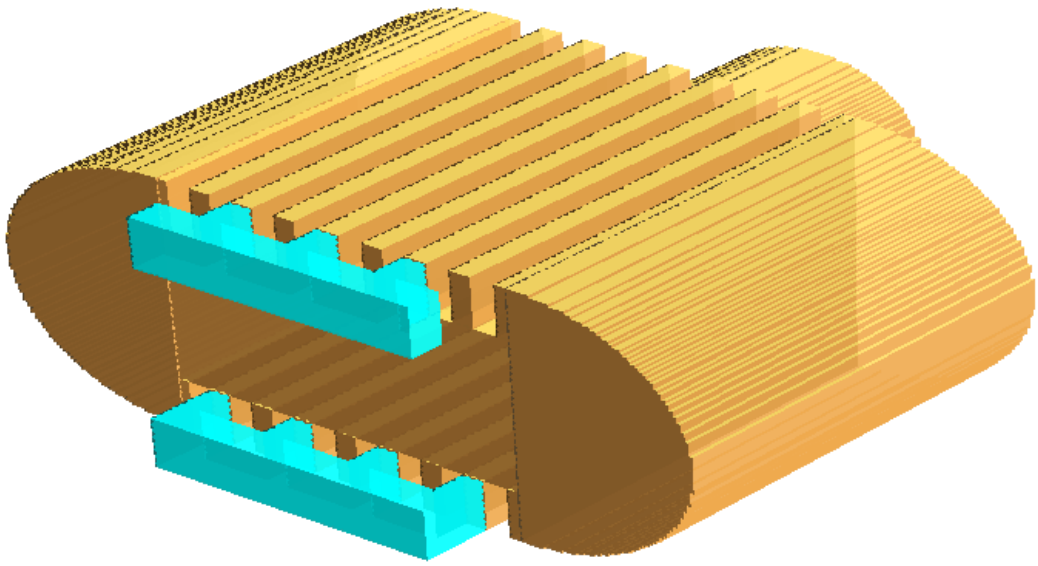

Figure 2-18. Inverted RPM with mode launching straps on the front.

The mode launcher geometry simulation parameters are 200 kV, 0.22 T, 1 cm anode-cathode gap, 0.65 cm vane spacing, and 2 cm vane depth. Figure 2-20 shows the voltage measured across slot-4 and Figure 2-21 shows a frequency of 2.96 GHz. Figure 2-22 shows the current drawn by the device. The input power is 1.5 GW assuming an average current of 7.5 kA with the 200 kV drive voltage. The output waveguide was loaded with "freespace" absorber material so that the power absorbed, J·E, could be measured. Figure 2-23 shows the power absorbed into the "freespace." The large modulation in the output power corresponds with a modulation seen in the voltage measurement of Figure 2-20. This mode launcher geometry requires that the two planar sections are in phase to properly couple power into the waveguide. The modulation in output power could therefore be caused by a relative phase change between the two planar sections. With a peak "freespace" power of 40 MW the peak device efficiency is 2.6%. While this efficiency is a factor of 10 below the typically quoted relativistic magnetron efficiency of 30% [2], it demonstrates that the device has the potential as a HPM source, particularly considering this was a completely non-optimized and under-resolved simulation. These 3D simulations typically had only two or three cells between different parts of the structure such as vane tips and strap to vane interfaces.

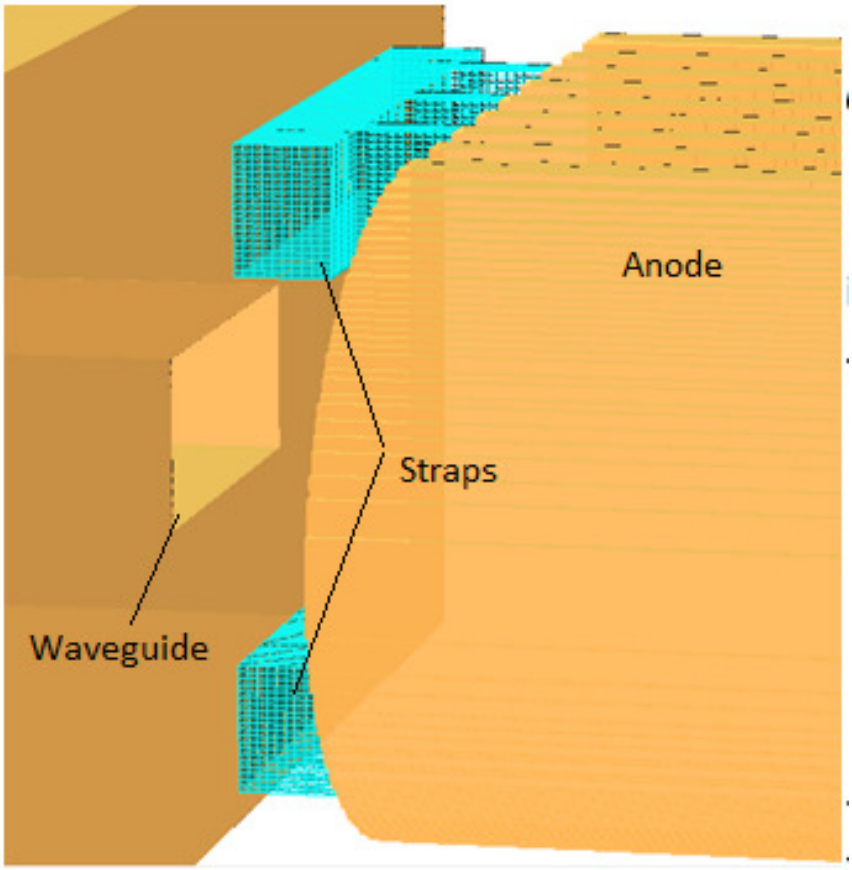

Figure 2-19. Detail of the mode launching straps in close proximity to the output waveguide.

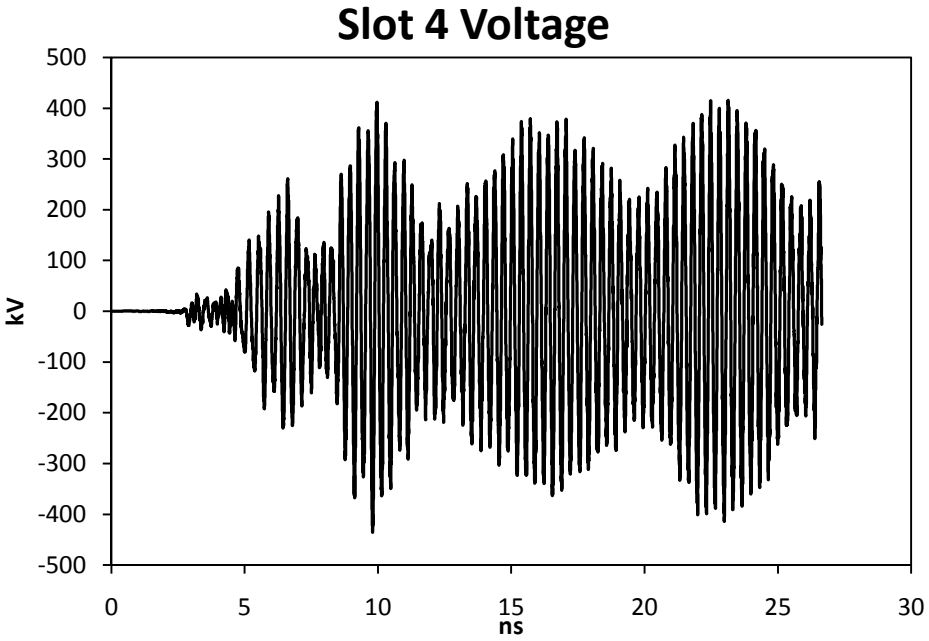

Figure 2-20. Voltage across slot 4 in the inverted RPM with axial mode launcher. The same type of power modulation seen in other simulations is present in this 3D simulation.

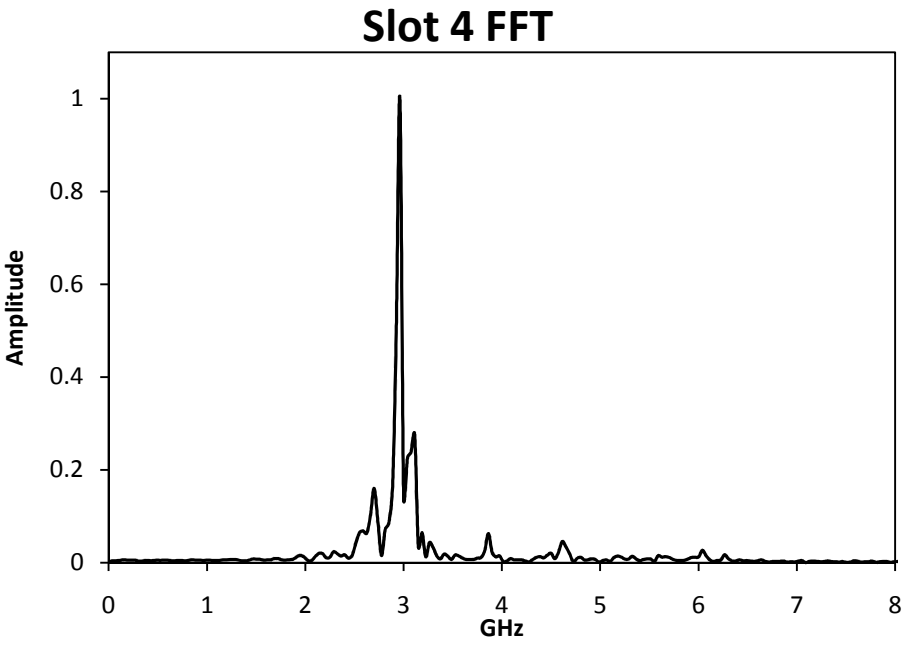

Figure 2-21.FFT of slot 4 voltage trace showing operation at 2.96 GHz with competition from some neighboring modes.

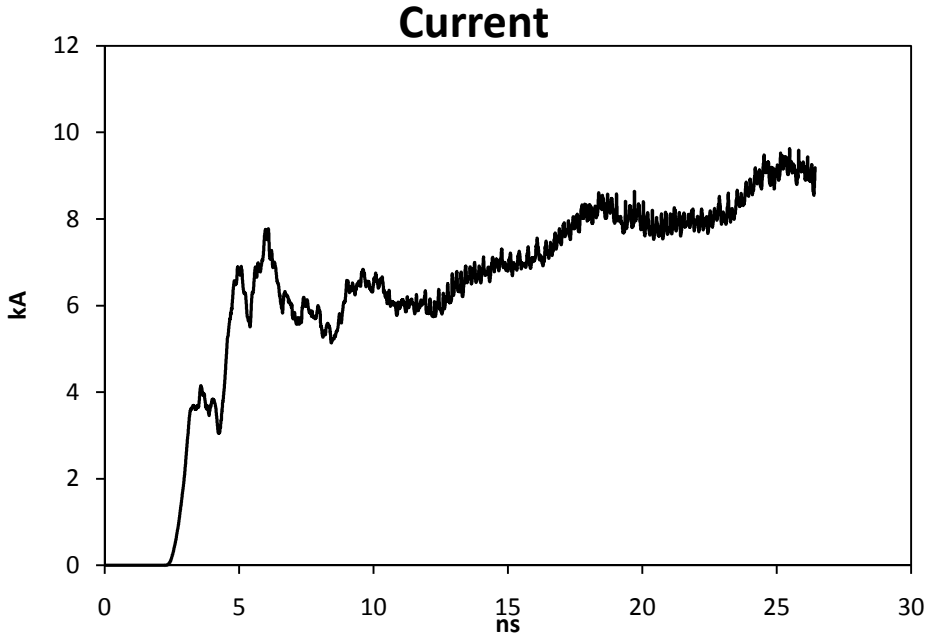

Figure 2-22. Current drawn by inverted RPM.

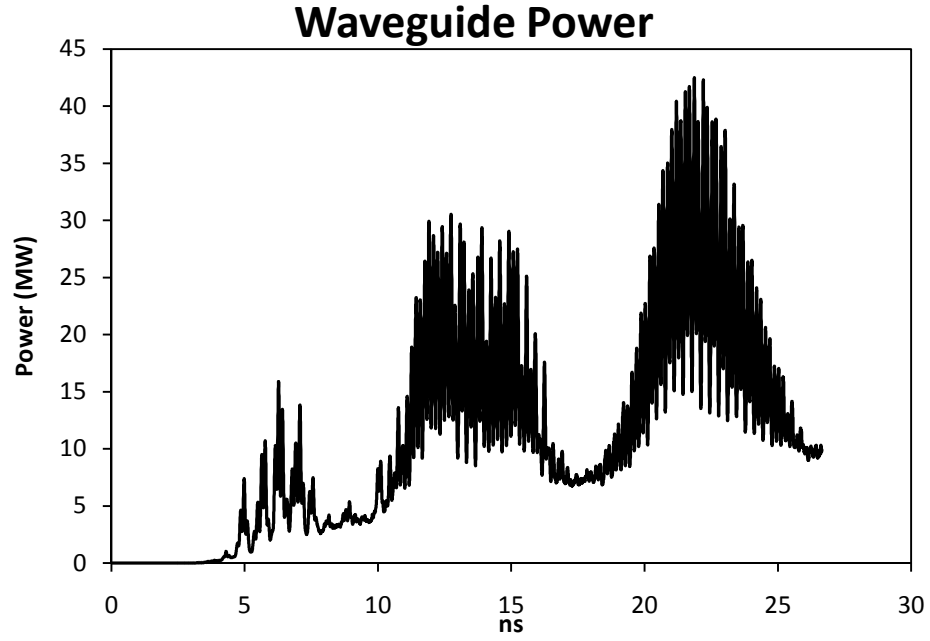

Figure 2-23. Power output into waveguide.

2.12 Conventional Axial B-Field RPM

Simulations of a conventional, cathode in the center, recirculating planar magnetron was run with MELBA parameters in order to have a baseline design around which an experiment could be built. The geometry of one such simulation is shown in Figure 2-24. This double, five-vane design uses a 1.8 kG magnetic field, 2 cm anode-cathode gap, and drive voltage of 300 kV with a 60 ns risetime. The outside dimensions are 16 cm x 25 cm which would easily fit in an existing vacuum chamber for use on the MELBA accelerator. The RPM started up at about 70 ns when the voltage reached 300 kV at which point it operated in π-mode for the remainder of the 300 ns simulation time. Figure 2-25 presents a sequence of images showing the startup of the RPM.

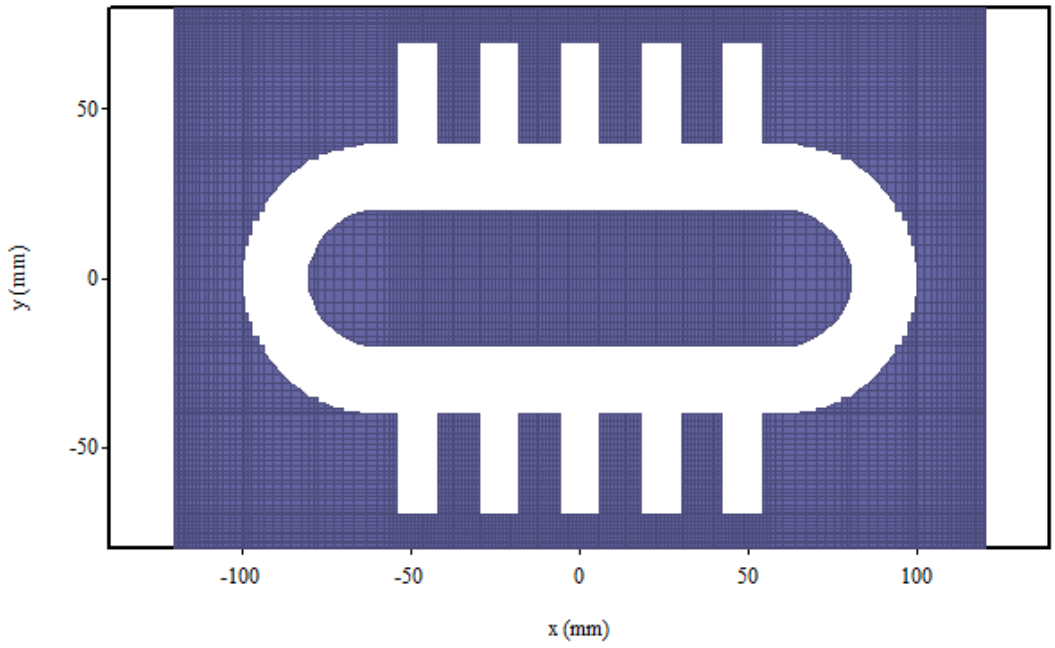

Figure 2-24. Conventional RPM design for MELBA parameters.

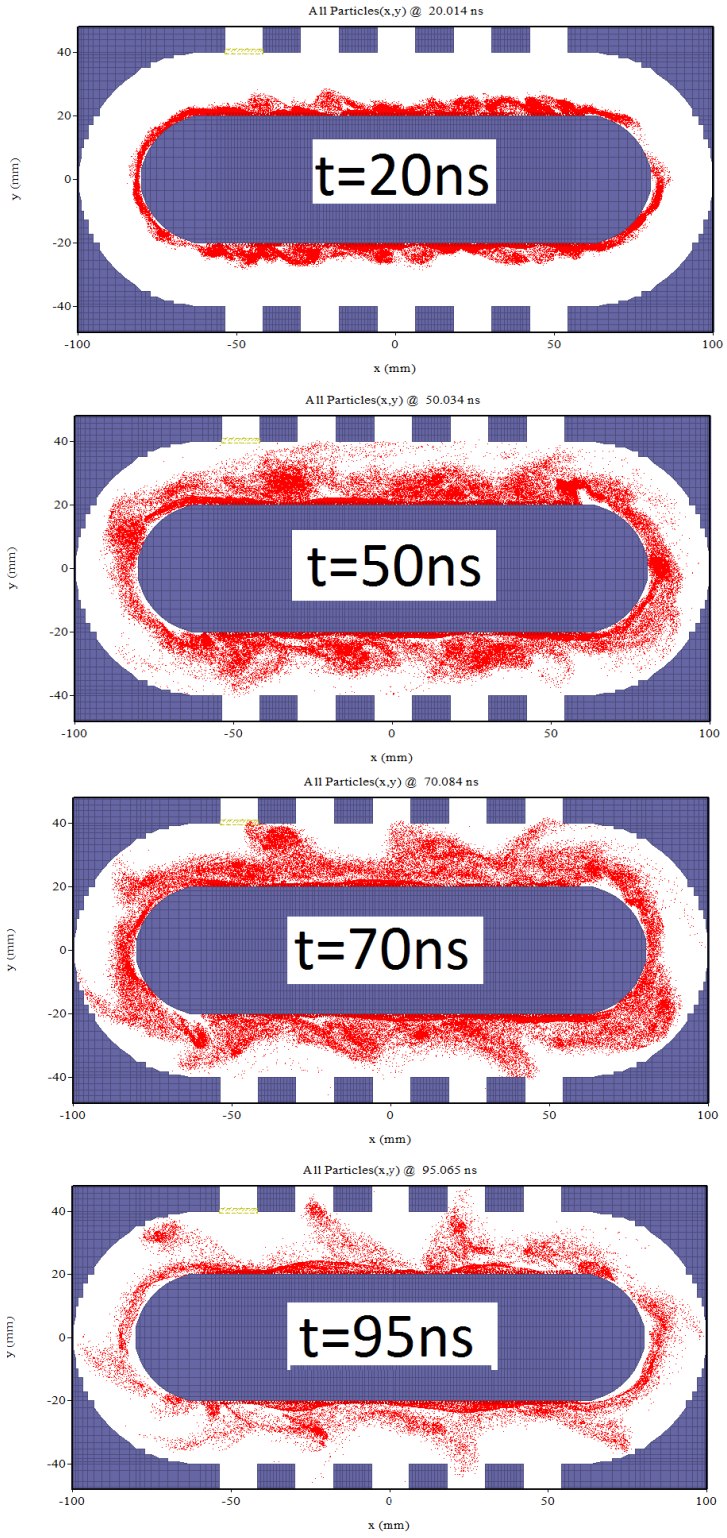

Figure 2-25. Electron plots at 25, 50, 70, and 95 ns showing the conventional RPM startup into π-mode .

This conventional RPM design showed significant fluctuation in the oscillations until ~200ns, after which it was stable, Figure 2-26. The frequency of these fluctuations is approximately 50 MHz. Figure 2-27 shows an FFT of the voltage trace showing π-mode oscillation at approximately 2 GHz, another mode is present in the FFT at 1.94 GHz . The time frequency analysis (TFA) presented in Figure 2-28 shows a nominally single mode of operation. The modes are spaced so closely that they are beyond the resolution of the TFA. Since the frequency difference between the modes in the FFT is the same as the frequency of the power modulation it is concluded that mode competition is responsible for the power modulation.

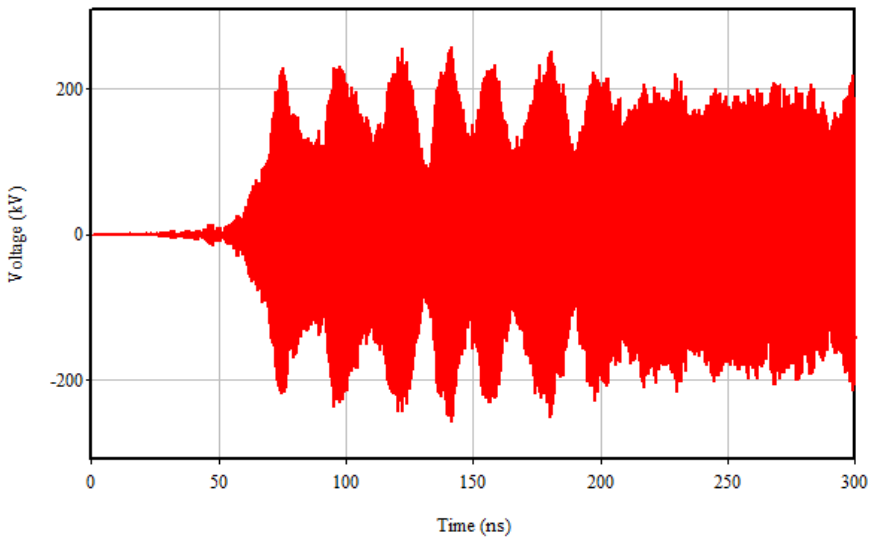

Figure 2-26. Voltage across slot 2 of conventional RPM; there is significant power modulation from shortly after startup at 75 ns until 200 ns after which the power stabilizes, this is likely due to competition between closely spaced modes.

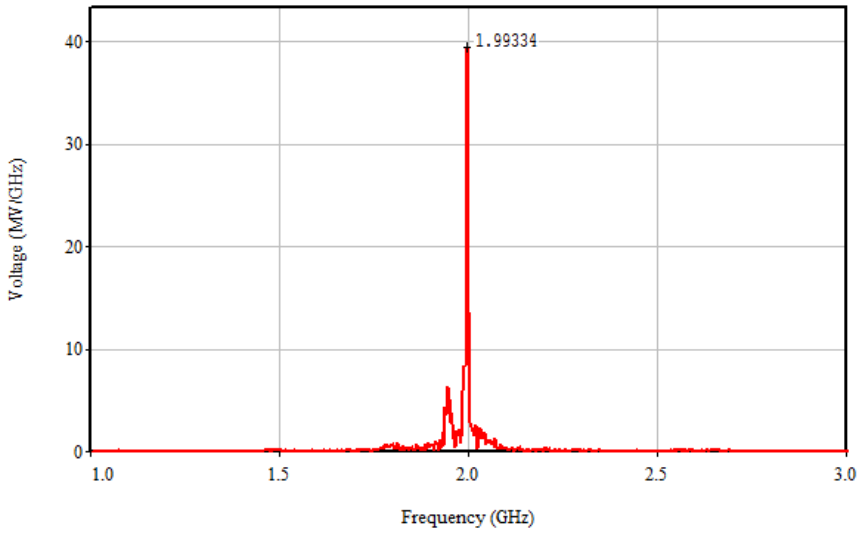

Figure 2-27. FFT of the voltage trace from slot 2 showing the peak frequency at 2 GHz.

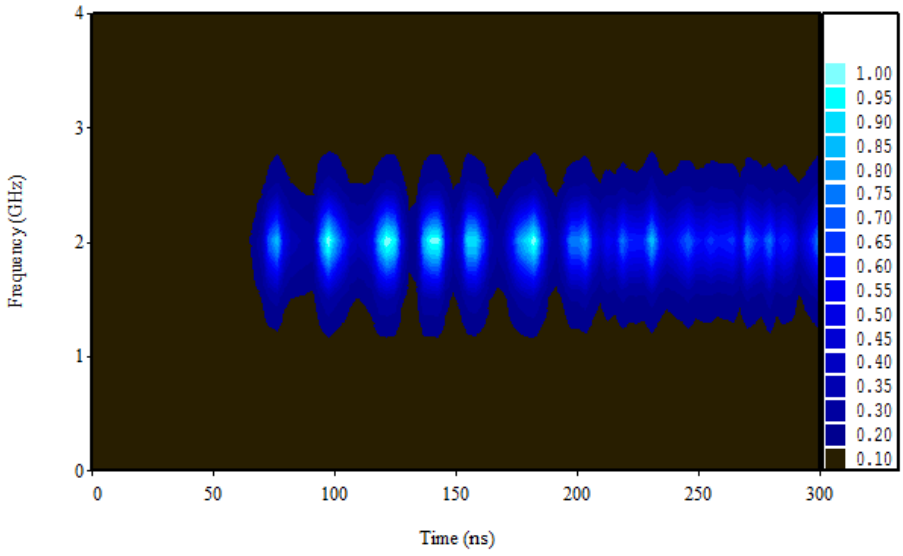

Figure 2-28. Time frequency analysis (TFA) showing single mode operation.

Due to the relatively simple geometry of this device and the ability to leverage existing hardware for the magnetic field, pulsed power driver, and microwave diagnostics, a conventional RPM of this general geometry will be the first one tested experimentally at UM. The present polarity of the MELBA accelerator is negative therefore the conventional

geometry would be tested first. Once an initial slow wave structure is tested and the microwave generation capability is demonstrated, future work should include efficient power extraction from the conventional geometry, and once the polarity of the MELBA accelerator is reversed, an inverted configuration can be tested experimentally. The problem of power extraction has not been solved on these devices. The highest extracted power on the axial-B field configuration as of the writing of this thesis is 2.6%. At this time it is unclear if the low extraction efficiency is due to the lack of sufficient resolution 3D simulations where maximization of extracted power was the goal, or if it is something specific to this particular design.

2.13 Effects of a Solenoidal Magnetic Field

In all of the preliminary simulations for the axial-B field RPM, the magnetic field was set as a constant. In reality, the magnetic field is generated by a Helmholtz coil arrangement. The magnetic field witnessed by an electron moving along the planar magnetron section will thus not be constant in the experimental device. The change in magnetic field will lead to a change in drift velocity as the electron moves down the planar section. To determine the degree to which the magnetic field would vary in an experimental RPM on the MELBA facility, the actual magnetic field was modeled with the Field Precision Magnum code. Figure 2-29 shows a lineout of the magnetic field with the planar region, where beam-wave interaction takes place, indicated. The magnetic field magnitude changes by 3.2% across the planar region of the device and reaches not less than 90% of the peak value in the circular region. Although the effects of the field nonuniformity will not be

known without simulation of the actual field, some previous simulations have shown improved performance when a nonuniform magnetic field was used [25].

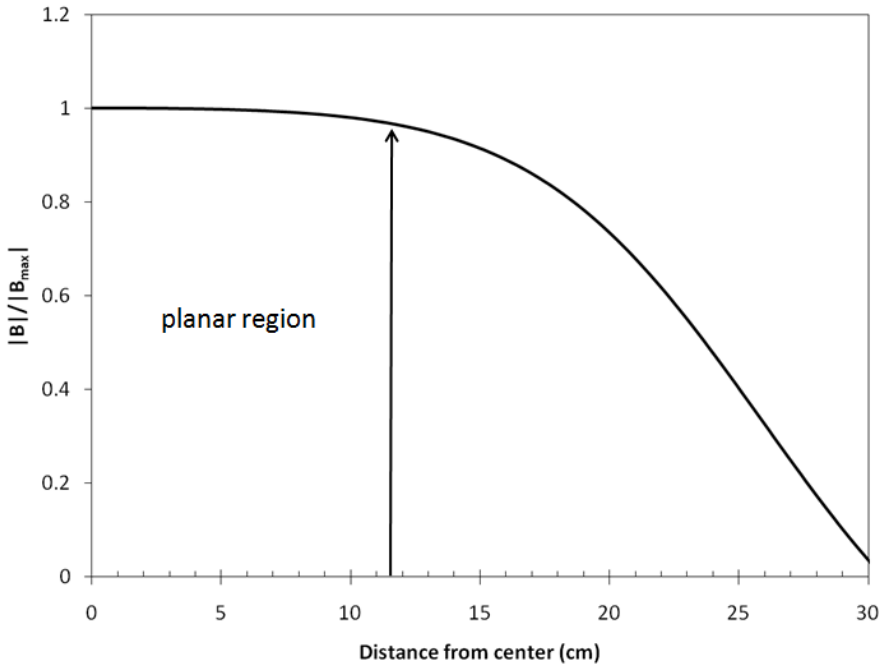

Figure 2-29. Lineout of the magnetic field. The planar region extends from 0 to 11.4 cm, the magnetic field changes by 3.2% in this region.

2.14 Radial B-Field RPM

The designs and data presented in this section are the work of Brad Hoff and are included in this chapter for completeness in introducing the RPM concept. The initial radial B-field RPM simulations were performed in MAGIC3D. The radial B-field RPM is inherently 3D, therefore the initial simulation studies required significantly more computational time than the initial simulations of the axial B-field RPM.

The basic geometry of the proof-of-concept radial B-field RPM is shown in Figure 2-30. The system is radial with 90 vanes in the slow-wave structure; a 3D view of this structure is shown in Figure 2-31. The anode and cathode of the RPM have inner radii of 7.5 cm and outer radii of 12.5 cm. The anode-cathode spacing is 1 cm and the vane spacing at radius of 10 cm is 3.5 mm. To avoid electrons exiting the interaction region radially, the equivalent of endloss for the radial B-field RPM, electrostatic confining rails are present. These rails at radii of 6 cm and 14 cm are shown in Figure 2-30 (b). Since these rails are at the same potential as the cathode, electrons will be reflected away from them and remain in the interaction region. The output of the device was measured in a piece of perfectly matched layer (PML) extending from a single vane of the 90 vane slow-wave structure indicated in Figure 2-30 (a). The voltage wave ports, indicated in Figure 2-30 (c), were used to bias the anode and cathode to the desired voltages with respect to the grounded wall.

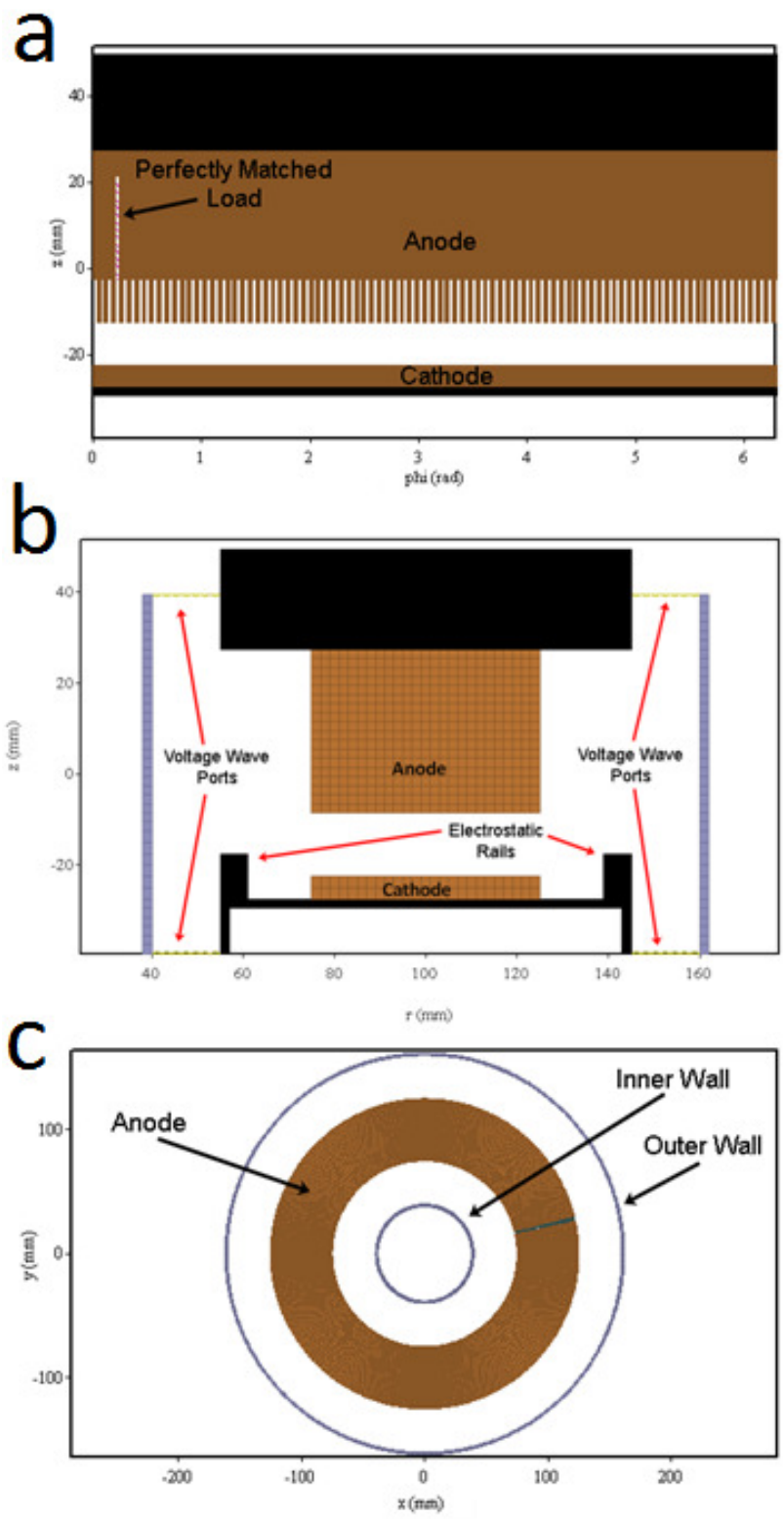

Figure 2-30. 2-D slices of the RPM simulation geometry in planes.

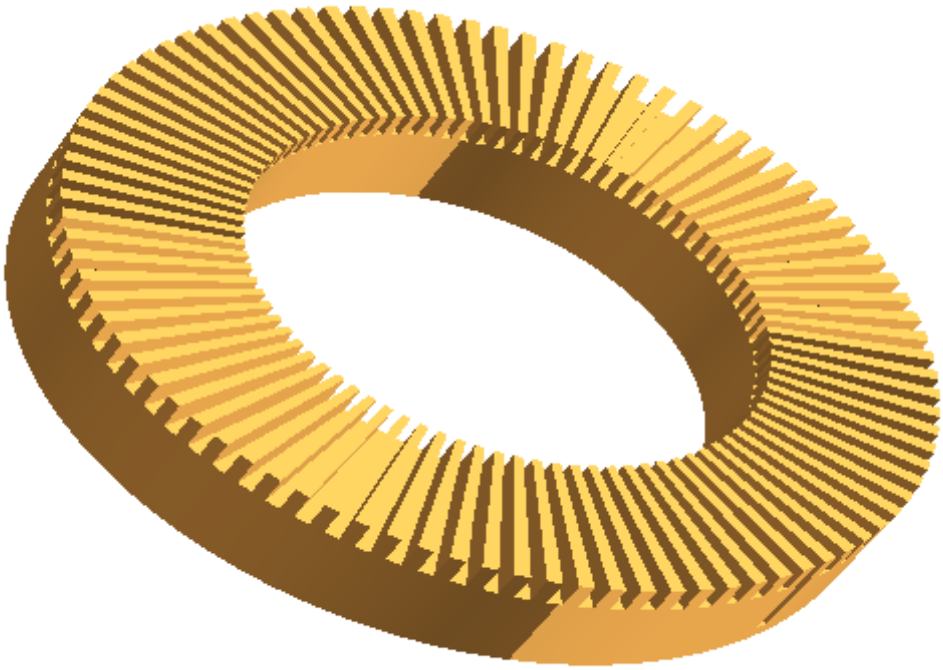

Figure 2-31. Three-dimensional rendering of the 90-vane RPM anode.

The radial magnetic field, required for operation of the RPM, was formed using two sets of "pancake" coils. The upper and lower coil sets, depicted in Figure 2-32, were axially separated from the middle of the A-K gap (Z = 0) by 5 cm. The field coils were energized such that the resulting magnetic field was oriented axially toward the A-K gap, thus forming a radially oriented cusping field in the RPM interaction region. Figure 2-33 shows a vector field plot of magnetic field within the A-K gap. Figure 2-34 depicts the radial magnetic field as a function of radius at the center of the A-K gap.

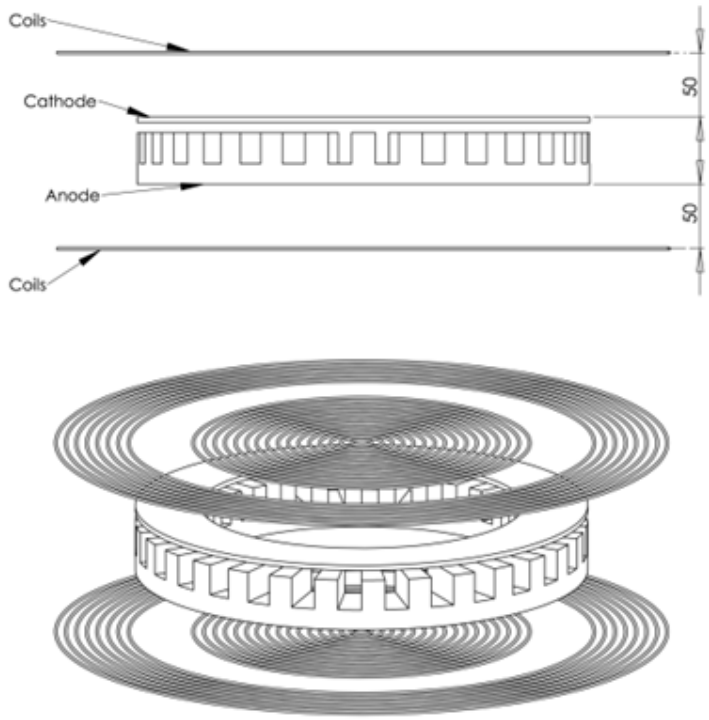

Figure 2-32. Three-dimensional side views of the anode and cathode assembly and magnetic field coils used in the MAGIC PIC RPM simulation.

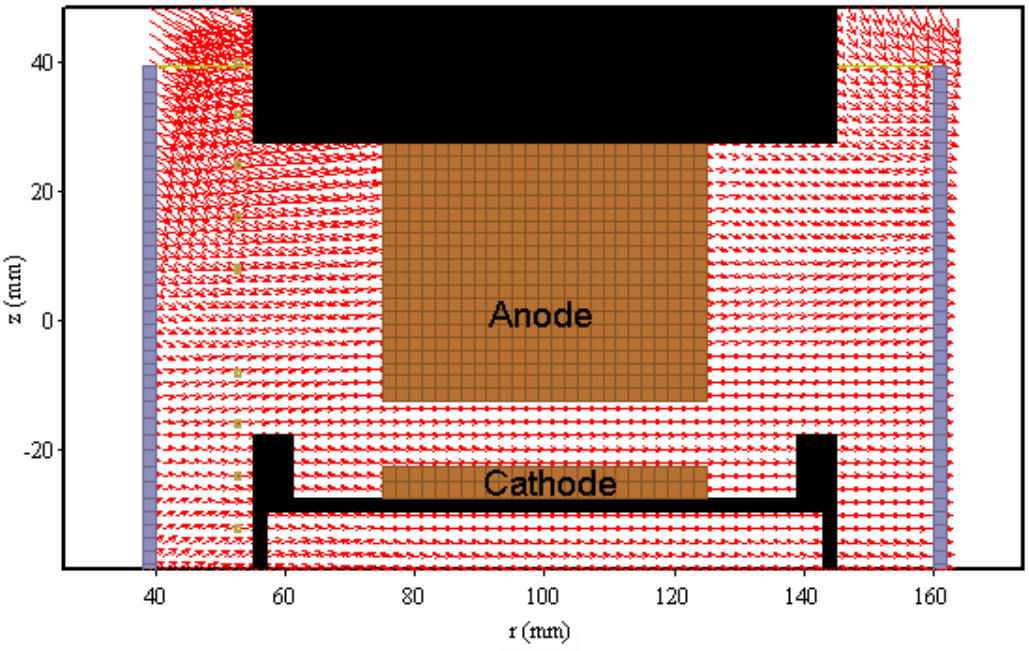

Figure 2-33 Vector field plot in the r-z plane, showing the magnetic field orientation in and around the A-K gap.

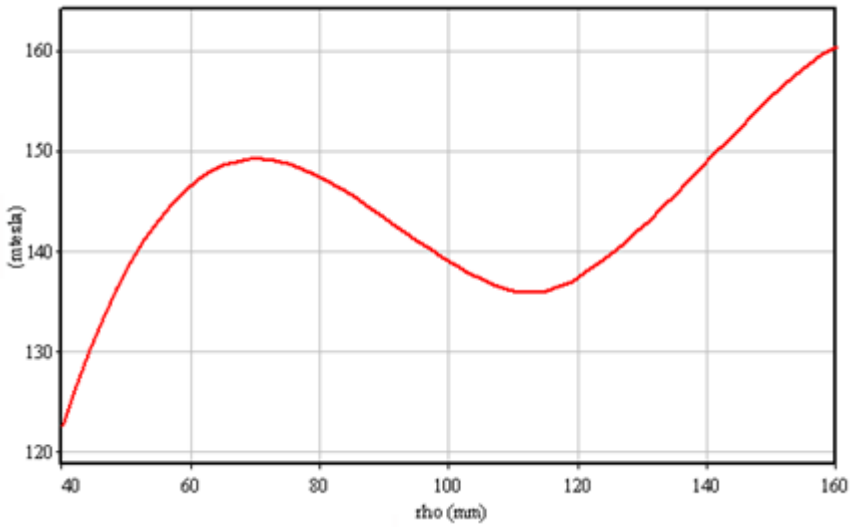

Figure 2-34. The radial magnetic field radius at the center of the A-K gap.

Plots for the current, voltage, and single vane extracted power, for the magnetic field parameters indicated in Figure 2-34, above, are depicted in Figure 2-35. Microwave power, extracted from a single vane, is 3 MW, resulting in an extracted electronic efficiency of this unoptimized simulation of less than 1%. Future simulation work will focus on developing an efficient extraction technique for this device. An electron phase space plot for the RPM simulation at a time of 20 ns is shown in Figure 2-36. The spoke positioning in the phase space plot indicates that, although the primary operating mode of the RPM is the π-mode, a noticeable amount of mode competition is present. An FFT of the time-varying voltage in one of the RPM cavities, displayed in Figure 2-37, shows the π-mode peak at approximately 6 GHz as well as two strong competing modes at 5.7 GHz and 8.1 GHz. Implementing the well-known techniques of magnetron strapping or using a "rising-sun" anode cavity geometry would likely help to suppress the competing modes.

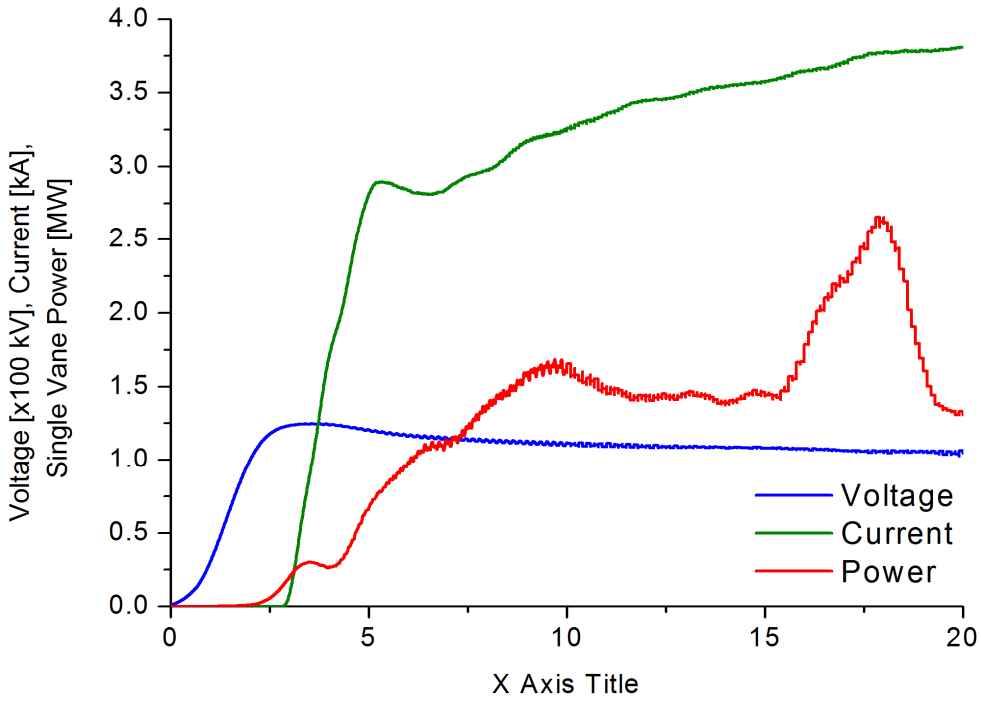

Figure 2-35. Current, voltage, and single vane extracted power plots for the RPM with radial magnetic field.

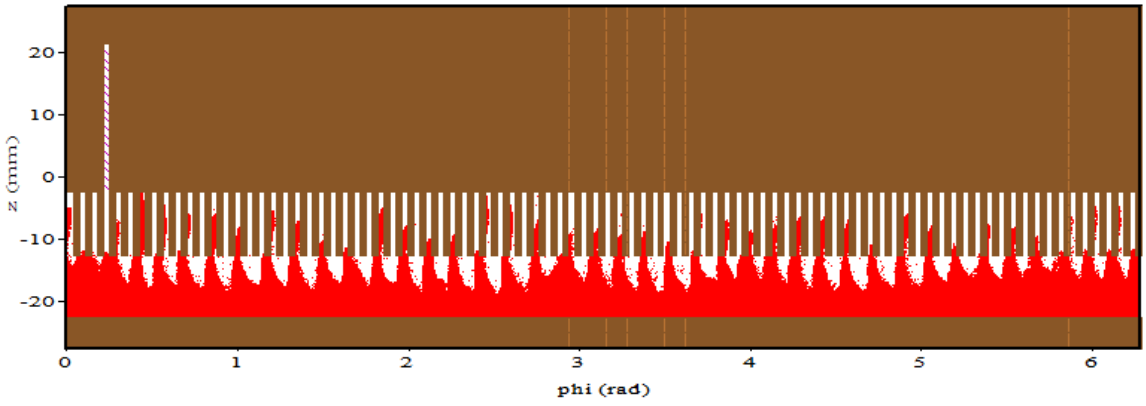

Figure 2-36. RPM electron plot at t = 20 ns.

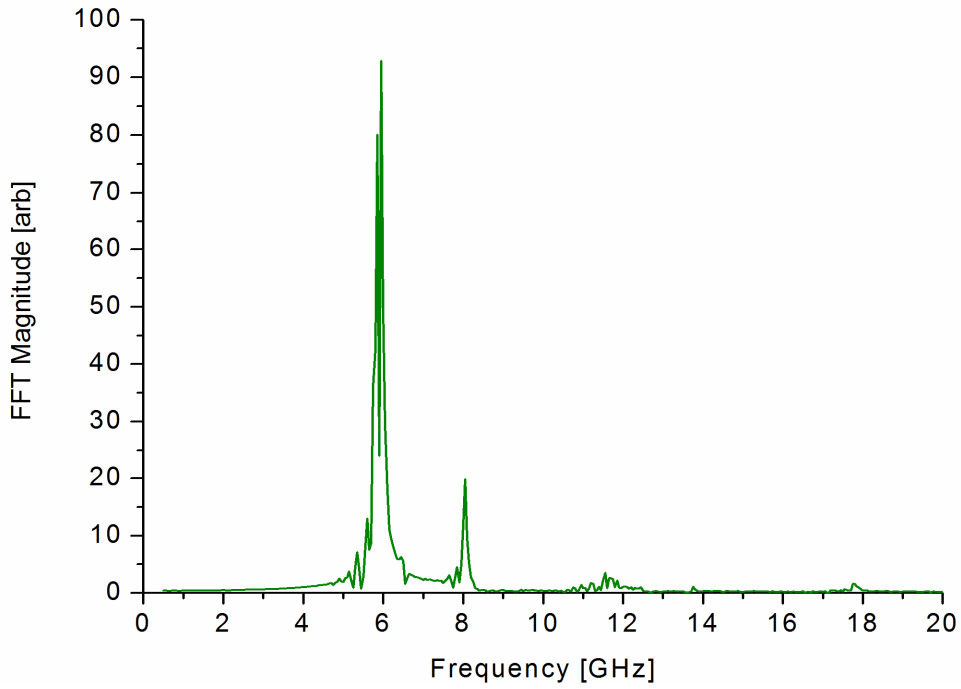

Figure 2-37. Operational mode spectrum for the RPM.

2.15 Conclusion

A new type of magnetron device, the recirculating planar magnetron, has been developed. This magnetron has several advantages over existing geometries. Baseline simulations of the RPM have been performed to determine the feasibility of such a device. The simulations indicate that the RPM will recirculate electrons and offer all the advantages of a planar magnetron over cylindrical designs. The axial B-field configuration has been successfully simulated in both conventional and inverted geometries. A 2D baseline simulation for a relativistic conventional magnetron with MELBA type parameters was done and showed π-mode operation at 2 GHz. The 2D proof-of-concept simulation of the inverted RPM showed startup and operation. The inverted design offers the advantage of rapid startup due to the negative mass instability (covered in detail in Chapter 3). Several

different 3D geometries of the inverted RPM were done with MELBA type parameters and showed that axial extraction from such a device is possible. Radial B-field simulations were done by Brad Hoff showing the feasibility of this configuration are included for completeness. Future work should include testing the devices experimentally and working through the challenges of efficient microwave extraction.

CHAPTER 3

NEGATIVE MASS INSTABILITY

3.1 Introduction

This chapter provides a critical examination of why the inverted magnetron configuration has a fast startup. In any coherent radiation source, the startup of oscillation depends crucially on the electron's response to the RF electric field of the operating mode. Three situations are possible. The first case, which is typical, is where the RF electric field has a tendency to re-enforce the perturbations that excite the RF mode. A prominent example being the gyrotron [1],[15], where the relativistic effect leads to enhanced bunching on the electron beam that rotates about a uniform magnetic field, as if the electrons have a negative effective mass [35]. The second case is where the RF mode tends to disperse the charge perturbations, the prime example being the space charge waves in the drift tube of the klystron [36], where the charge perturbation executes simple plasma oscillations in the moving frame of the electrons, whose effective mass is positive. The third case is the most unusual, occurring for a particular combination of the crossed electric and magnetic field, in which the electrons hardly respond to the RF mode at all, as if the effective mass of the electron is infinite [28].

An electron rotating under a general combination of an axial magnetic field and a radial electric field may exhibit negative, positive, and infinite effective mass behavior [1],[28]. The simulation study presented here is the first to provide a systematic study of the behavior of a rotating electron beam for general magnetic and electric fields [37]. Previous simulation based studies of the negative mass behavior of a rotating electron beam were concerned with a beam that is subject to a magnetic field with no applied radial electric field such as in the case of the gyrotron or betatron [38-41]. The general simulation was motivated by the electron behavior in the inverted recirculating planar magnetron, where rapid start up utilizes the negative mass instability, in addition to the promise of greatly reduced electron endloss from the inverted geometry. Some recent simulations [42] also confirmed that the inverted magnetron configuration (that has a positive radial electric field together with an axial magnetic field [43]) has a faster startup than the conventional magnetron (that has a negative radial electric field together with an axial magnetic field).

A thin annular electron layer is subject to instabilities that can lead to layer breakup and clumping. These include cyclotron maser, diocotron, and negative mass instabilities. It has been shown that these effects can all be derived from a single dispersion relation [44]. The geometry is shown in Figure 3-1, with an annular beam in a coaxial geometry rotating in equilibrium at a fixed radius with relativistic azimuthal velocity v_θ. The instability can be understood by considering the 3 charges shown as dots in the upper right pane of Figure 3-1.

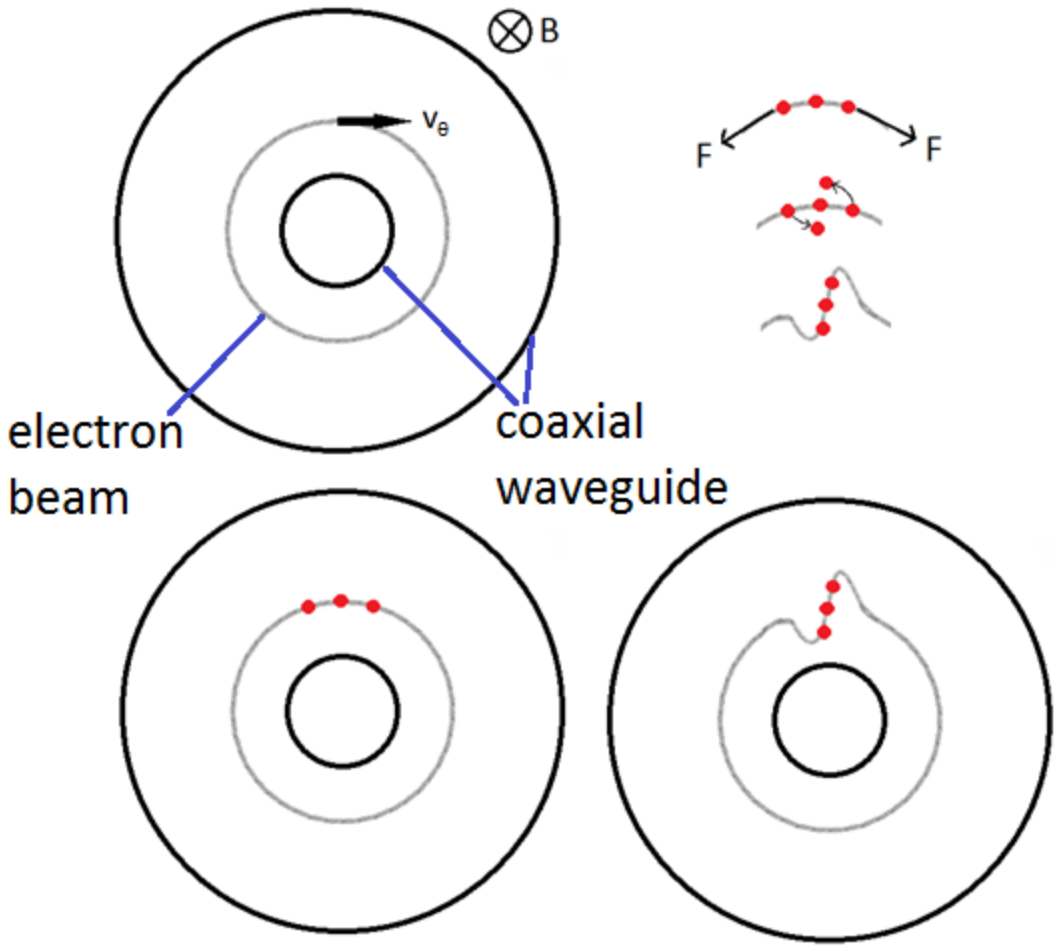

Figure 3-1: Negative mass instability on an annular beam in coaxial geometry.

Consider an annular electron beam rotating subjected to an axial magnetic field B. If there is a local density perturbation, represented by the 3 particles, the electrostatic force felt by the leading particle from the center particle causes the leading particle to accelerate, increasing the particle velocity and causing it to move radially outward. The relativistic mass factor, $\gamma = \left(1 - v_\theta^2/c^2\right)^{-1/2}$, will be increased. This leads to a decrease of the rotational frequency, ω_0, given by

$$\omega_0 = \frac{\Omega_c}{\gamma}, \tag{3.1}$$

where $\Omega_c = |e|B_0/m_0$ is the non-relativistic electron cyclotron frequency. Thus, the leading particle falls back toward the center of the bunch. By the same argument the trailing particle slows down, moves radially inward, but speeds up azimuthally as if the effective mass is negative. This negative mass effect leads to azimuthal bunching (bottom panes of Figure 3-1). It is clear that this effect is unstable as the presence of an azimuthal electric perturbation will lead to particle rearrangement that reinforces the perturbation.

Recent simulations of a new microwave magnetron, the recirculating planar magnetron (RPM) [26], prompted the revisiting of the negative mass instability (see also chapter 2). The inverted RPM is shown in Figure 3-2. In the simulations, as soon as electrons move into the circular sections the electrons form bunches which are maintained, rather than dispersed, around the bends. After the circular portion of the device the electron bunches reenter the planar magnetron sections and move past the vanes in the slow wave structure and the excitation of a microwave signal begins. In the initial simulations this process occurs within a few ns of particle emission leading to fast startup of the RPM in the inverted configuration. The same general electron behavior has been previously seen in smoothbore inverted magnetron simulations. This is in contrast to conventional smoothbore magnetron simulations where a uniform hub of electrons is formed at the beginning and the final state is a uniform density electron cloud with no clearly identifiable features orbiting the central cathode.

There have been a number of previous PIC simulation based studies of the negative mass instability, however, these have focused on the case where an annular beam is supported by magnetic field alone, such as in a gyrotron configuration [38-41]. The present study seeks to extend this to arbitrary axial magnetic and radial electric fields supporting an equilibrium beam.

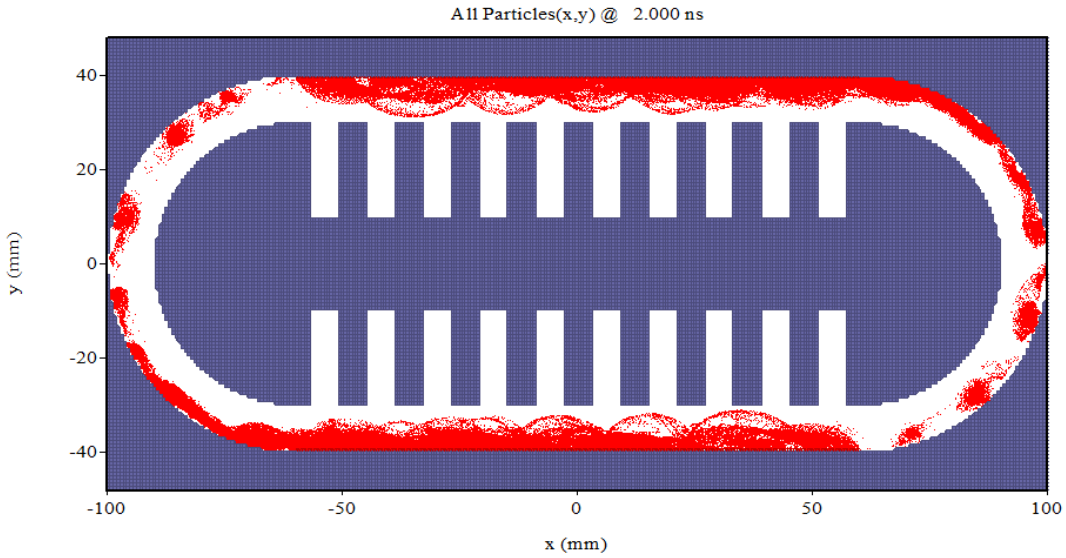

Figure 3-2. Recirculating planar magnetron (RPM) simulation showing immediate bunching and preservation of bunches around the bends, in the inverted configuration with the central anode and outer cathode.

3.2 Equilibrium Solution

The motion of a thin annular relativistic electron beam in equilibrium in a coaxial geometry will be derived from the force law for arbitrary radial electric and axial magnetic fields. Beginning from the Lorentz force equation for a charged particle in the presence of electric and magnetic fields

$$\vec{F} = q[\vec{E} + \vec{v} \times \vec{B}] \tag{3.2}$$

Setting the force equal to the centripetal acceleration of the electron beam with relativistic factor $\gamma = (1 - \beta_\perp^2)^{-1/2}$, $\beta_\perp = v_\theta / c$ orbiting at radius r in an axial magnetic field B_0 with a radial electric field E_r

$$\frac{m_0 \gamma v_\theta^2}{r} = e[E_r + v_\theta B_0]. \tag{3.3}$$

Dividing by the left side of (3.3),

$$1 = \frac{eE_r r}{m_0 \gamma v_\theta^2} + \frac{eB_0 r}{m_0 \gamma v_\theta}. \tag{3.4}$$

Defining the dimensionless parameter h

$$h = \frac{eE_r r}{m_0 \gamma^3 v_\theta^2}. \tag{3.5}$$

After substituting h into the first term on the RHS of (3.4) the second term can be solved for in terms of h and the force law (3.4) then becomes

$$1 = \gamma^2 h + (1 - \gamma^2 h), \tag{3.6}$$

So that $\gamma^2 h$ represents the fraction in the centripetal acceleration that is provided by the electric field, and the remaining $1 - \gamma^2 h$ is provided by the $v \times B$ force. This force law equation (3.6) allows for the limits of a coaxial system in equilibrium to be expressed in terms of a single dimensionless parameter h and the relativisitic factor γ [28]. Table 3-1 describes some common high power microwave devices with respect to the parameter h.

Table 3-1. Limits in h for different devices

h	Field Profiles	Device
$h = 0$	Magnetic field only	large orbit gyrotron
$h = 1/\gamma^2$	Electric field only, radially outward	orbitron
$h \gg 1/\gamma^2$	Magnetic field with electric field directed radially outward	inverted magnetron
$h \ll -1/\gamma^2$	Magnetic field with electric field directed radially inward	conventional magnetron

Many high power microwave sources are characterized by h [23],[28]. For example, $h = 0$ corresponds to the large orbit gyrotron [1],[15],[28] and peniotron [45], $h = 1/\gamma^2$ corresponds to the orbitron configuration [1],[45], whereas $h \gg 1/\gamma^2$ corresponds to the inverted magnetron, and $h \ll -1/\gamma^2$ corresponds to the conventional magnetron, all shown in Figure 3-3. These devices depend on the synchronism between the electron's azimuthal velocity with the electromagnetic mode's azimuthal phase velocity. It then follows that the startup critically depends on the responsiveness of the electrons to the mode's azimuthal electric field, at the location of an electron. It has been shown in [28] and is derived in appendix A that an electron rotating under a combination of axial magnetic field B_0 and a radial electric field E_0 has an effective mass, m_{eff}, in the azimuthal direction given by

$$m_{eff} = -m_0\gamma\left(\frac{1+\gamma^2h^2}{\beta_\perp^2+2h}\right), \tag{3.7}$$

where $\beta_\perp = v_\theta/c = (1-1/\gamma^2)^{1/2}$, and c is the speed of light. The ratio m_0/m_{eff} is plotted as a function of the parameter h in Figure 3-3. The location of infinite mass at $h = -\beta_\perp^2/2$ is the point that divides the positive mass (stable) region $h < -\beta_\perp^2/2$ and the negative mass

(unstable) region $h > -\beta_\perp^2/2$. The operating regions of common microwave tubes are indicated in the figure. The magnetron operates in the positive mass regime whereas most other microwave tubes operate in the negative mass regime. The gyrotron uses magnetic field alone to support the electron motion and therefore operates at $h = 0$. The orbitron configuration uses a radial electric field alone to support electron motion operates at $h = 1/\gamma^2$, or $\gamma^2 h = 1$, equation (3.6).

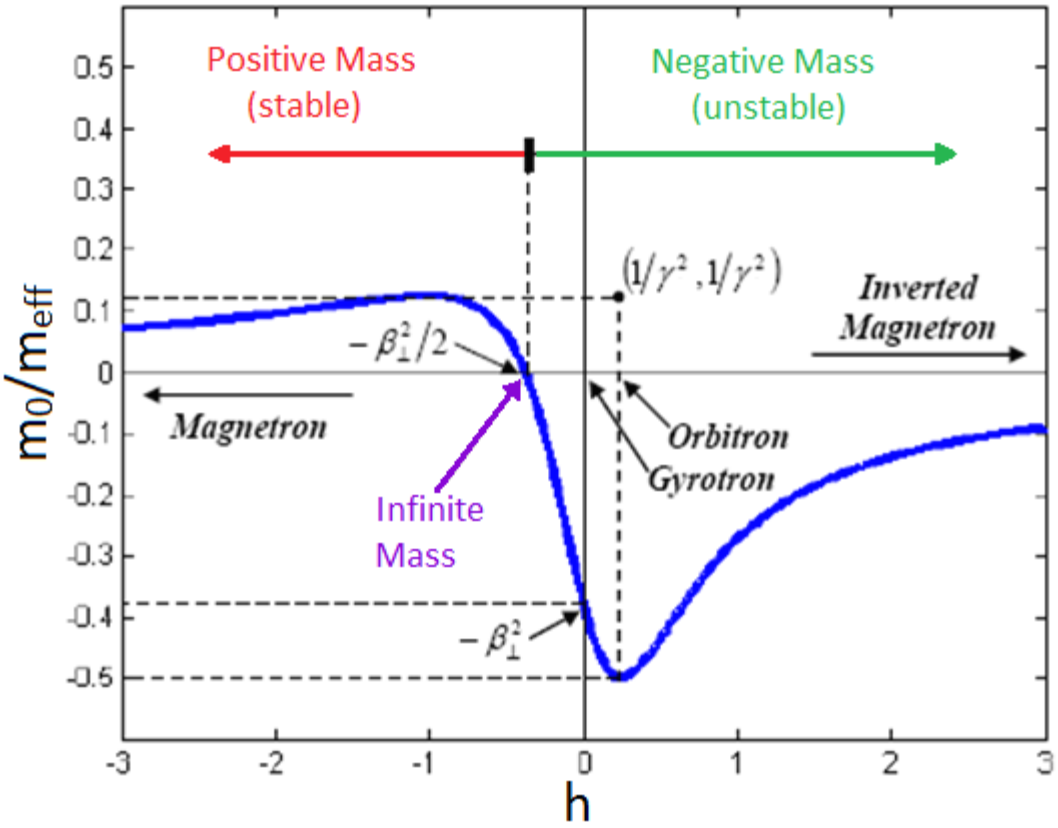

Figure 3-3. m_0/m_{eff} as a function of the parameter h for $\gamma = 2$. The regions of positive and negative mass (stable and unstable regions) are indicated. The operating point of various microwave tubes are indicated.

3.3 Simulations

Simulations of a thin annular beam are performed in the particle-in-cell code MAGIC [29].

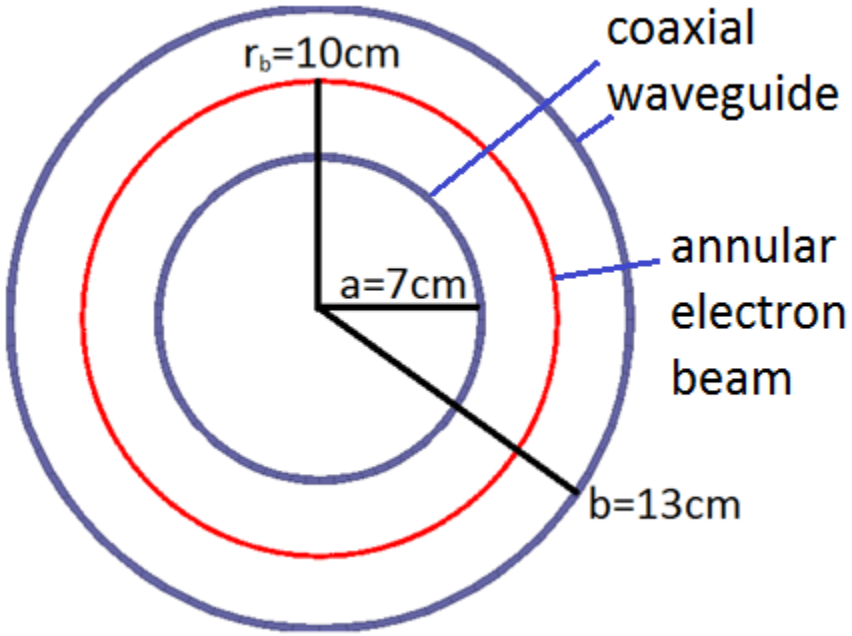

Figure 3-4. Simulation geometry used in MAGIC.

The simulation geometry is shown in Figure 3-4. The system is coaxial with inner radius a = 7 cm and outer radius b = 13 cm with a 2 mm thick beam at radius r_b = 10 cm. The electron beam is cold having zero temperature in the radial coordinate and no initial velocity spread in the azimuthal coordinate. To avoid coupling the beam to a vacuum cavity mode whose eigenfrequency, ω_{ln}, [given approximately by equation (3.8)] the beam rotational frequency, $\omega_0 = cl\beta_\perp/r_b$, is chosen to far be below the lowest order cavity modes.

$$\omega_{ln} \approx c\sqrt{\left(\frac{2l}{a+b}\right)^2 + \left(\frac{n\pi}{b-a}\right)^2}. \tag{3.8}$$

Here n is the radial mode number and l is the azimuthal mode number. For $r_b = (a+b)/2$ as is the case here, equation (3.8) reduces to $\omega_{l0} = cl/r_b$ for $n = 0$. This is higher than the beam rotation frequency ω_0 by a factor of $1/\beta_\perp$. Therefore for factors of $\beta_\perp \ll 1$ there will be no coupling of the beam to the primed cavity mode. The voltage and magnetic field required by the force law for a beam to be in equilibrium are

$$V = h\left[\left(\frac{m_0 c^2}{e}\right)\ln\left(\frac{b}{a}\right)\gamma(\gamma^2-1)\right], \tag{3.9}$$

$$B = (1-\gamma^2 h)\left[\left(\frac{m_0 c^2}{e}\right)\frac{(\gamma^2-1)}{r_b \gamma v_\theta}\right]. \tag{3.10}$$

The geometry, the beam energy of 51.1 kV ($\gamma = 1.1, \beta_\perp = 0.41$), and the choice of the h parameter sets the voltage and magnetic field from equations (3.9) and (3.10) for a beam of sufficiently low current that the self electric and magnetic fields are negligible. In the simulation, the beam is inserted at time $t = 0$ and the Poisson equation is solved with the beam present subject to the boundary value voltage from equation (3.9), this step is required for the problem to be solved self consistently. The electric field values determined from the Poisson solve are used to preset the initial dynamic electric fields in the code, if this step is not performed the code will insert an infinitely massive group of oppositely charged particles into the simulation at the location of the electron beam to neutralize the charge. This allows for the simulation to correctly solve for the presence of nonzero charge existing at time $t = 0$, of the form,

$$n(\theta) = n_0[1 + \alpha \sin(l\theta)]. \tag{3.11}$$

The beam is seeded with an initial density perturbation according to equation (3.11) where n_0 is the average charge density, α is the perturbation amount, and l is the azimuthal mode number.

Typical simulation parameters are $en_0 = 10^{-4}$ C/m^3, $\alpha = 0.1$, and $l = 6$. The initial density perturbation gives an azimuthal electric field which can lead to the growth of the instability for $m_{eff} < 0$, electrostatic wave oscillation for $m_{eff} > 0$, and preservation of the initial perturbation for $m_{eff} = \infty$. The density perturbation as a function of angle is shown in the top plot of Figure 3-5. For negative mass unstable configurations the density peak will grow with time as seen in the peaked density profile shown in the bottom plot of Figure 3-5 for the orbitron configuration, $h = 1/\gamma^2$.

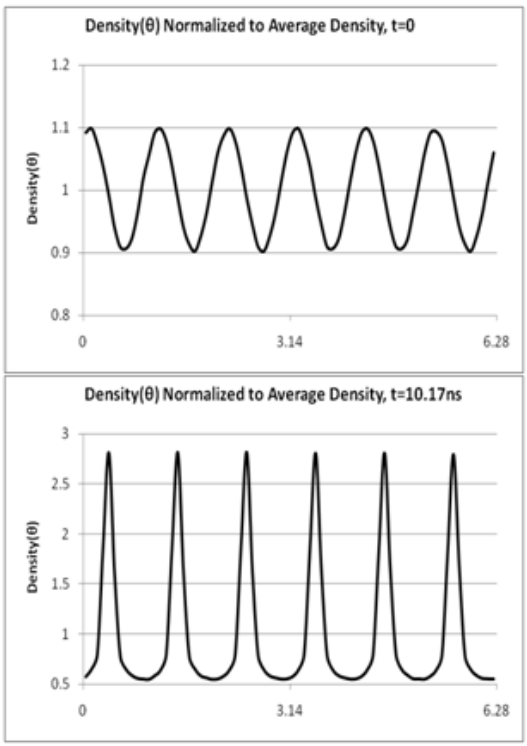

Figure 3-5. Azimuthal dependence of the normalized density with $\alpha = 0.1$ and $l = 6$ for the orbitron at time 0.56 ns (top) and 10.17 ns (bottom).

The particle plots shown in Figure 3-6 correspond to the azimuthal density plots in Figure 3-5. These clearly show the rearrangement of particles that occurs for negative effective mass particles in the presence of an azimuthal electric field perturbation that arises from the initial charge perturbation. Particles that were initially pushed ahead of the space charge region are increased in energy and move to a larger orbital radius and subsequently slow in the azimuthal direction such that the initial peak in space charge catches up with the particles in the higher orbit. Likewise, particles initially slowed by the space charge move to a lower orbit and catch up to the initial space charge peak leading to increased bunching, similar to Figure 3-1. If the cylindrical structure were loaded with a slow wave structure the bunched beam would readily interact with it due to the azimuthal electric field present as a result of the bunching.

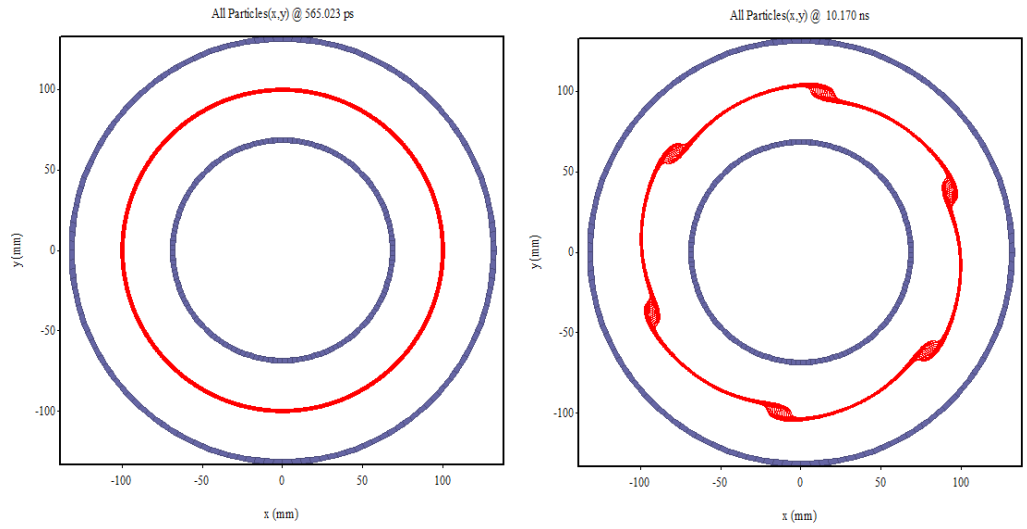

Figure 3-6.R-θ electron plots for $h = 1/\gamma^2$ from MAGIC showing the particles at 0.56 ns (left) and 10.17 ns (right) corresponding to the density(θ) plots in Figure 3-5. Azimuthal bunching due to the negative mass instability is present in the right pane of the figure, this bunching leads to an enhancement of the initial azimuthal electric field perturbation.

The bunching of the particles and therefore growth of the initial perturbations are quantified by monitoring the azimuthal electron current. The initial current for each case is 25 ± 2.5 A from the sinusoidal perturbation due to the density modulation from equation (3.11).

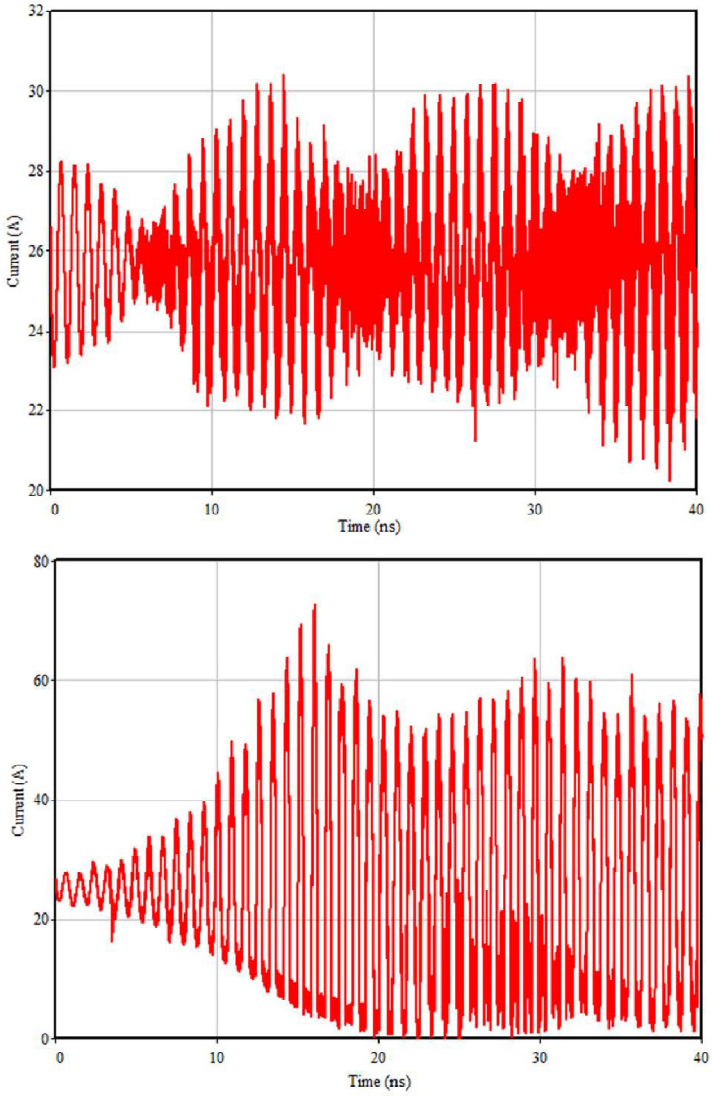

Figure 3-7. Azimuthal current for h = -0.5 (top) showing electrostatic oscillation beating at the reduced plasma frequency, and for h = 2 (bottom) showing growth due to the negative mass instability for the inverted magnetron configuration. The growth rate in the negative mass case is determined by the exponentiation time of the current prior to saturation. The current rise seen in the bottom pane of the figure shows exponential growth in the current perturbation to the point of saturation at ~70 Amps occurring at ~15 ns.

To avoid numerical artifacts from the finite difference method, sufficient grid resolution is necessary. A convergence study was performed in order to determine the necessary grid resolution and to solve the problem correctly. To represent a cold beam correctly in PIC simulations it is recommended to have at least 4 particles per cell. In this study 8 particles per cell were used and this value was held constant as the grid resolution was adjusted in order to avoid effects related to changing particle statistics. The simulations were run and the azimuthal electron density was monitored for different values of grid resolution. Figure 3-8 shows the current for three different values of R and θ resolution. The trace in the top of Figure 3-8 shows the current reaching 50 A in approximately 17 ns. As the grid resolution is doubled in both R and θ, center of Figure 3-8, the time to reach 50 A is increased to 20 ns. The time to reach 50 A does not change as the grid resolution is further increased by a factor of 2, bottom of Figure 3-8. Although the saturation characteristics are likely more reliable in the highest resolution runs, the quantification of growth rates only use data up to 36 A total azimuthal current, therefore the simulations were run with the parameters of the center of Figure 3-8. The 36 A value was chosen as it is far below the saturation current; however, still provides sufficient data to quantify the exponential current rise for unstable cases.

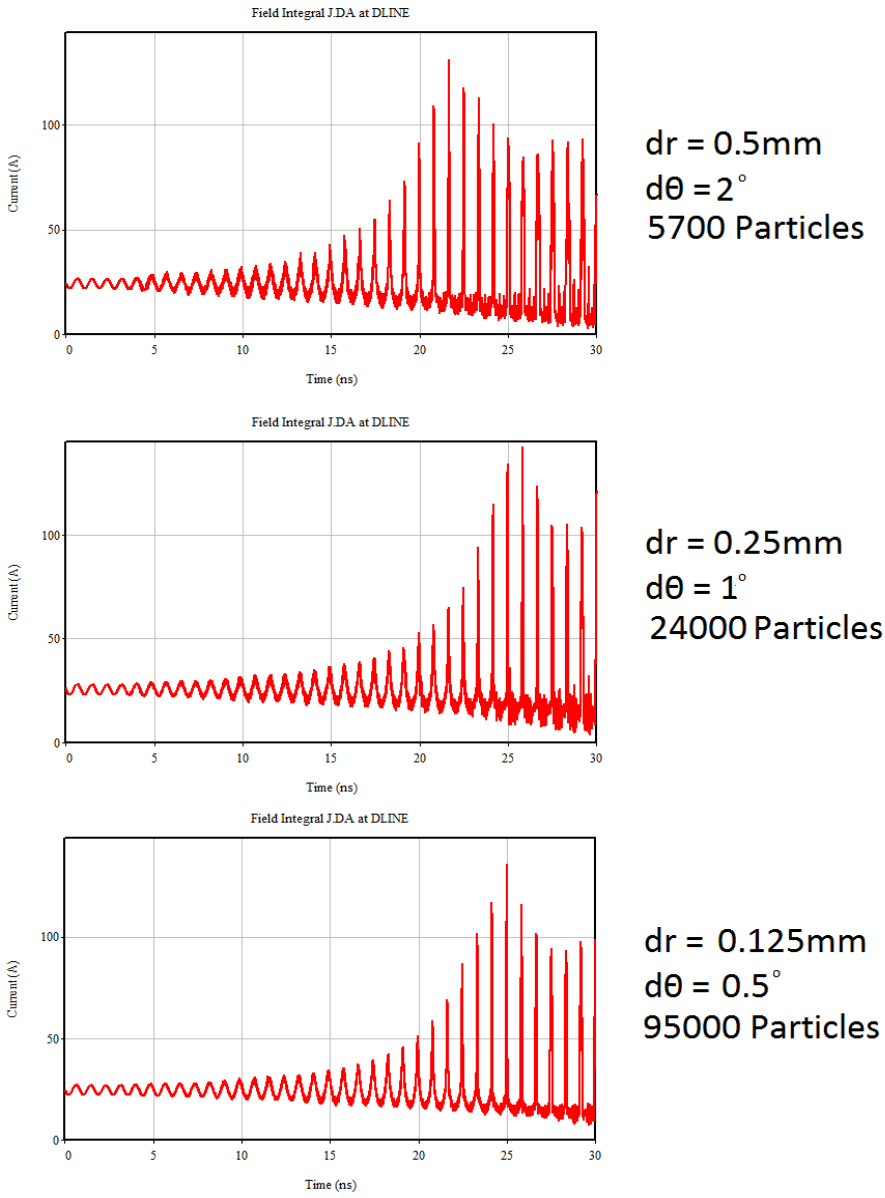

Figure 3-8. Azimuthal density plot of the gyrotron, h=0, used to determine if the simulation had converged.

3.4 Positive Mass Oscillation

The positive mass simulations, $h < -\beta_{\perp}^2/2$, show no growth of the initial perturbation, (cf. Figure 3-3). The beam maintains an annular shape until the end of the simulations and is subject to an electrostatic oscillation in the moving frame of the beam. The frequency of these oscillations, ω, can be determined by the lowest order dispersion relation (3.12) [23],[28].

$$(\omega - l\omega_0)^2 = \left(\frac{l\tau}{r_b}\right)\left(\frac{e^2 n_0}{\epsilon_0 m_{eff}}\right)\left(\frac{1}{b_+ + b_-}\right) \tag{3.12}$$

where ω_0 is the angular frequency of the beam, l is the mode number, τ is the beam thickness, $r_b$is the beam radius, n_0 is the unperturbed electron number density, m_{eff} is the effective mass given by equation (3.7), and b_+ and b_- are the normalized wave admittances looking radially outward and inward given by [28]

$$b_+ = -\frac{l}{x_2}\left(\frac{C_1^+ J_l(x_2) + C_2^+ Y_l(x_2)}{C_1^+ J'_l(x_2) + C_2^+ Y'_l(x_2)}\right), \tag{3.13}$$

$$b_- = \frac{l}{x_1}\left(\frac{C_1^- J_l(x_1) + C_2^- Y_l(x_1)}{C_1^- J'_l(x_1) + C_2^- Y'_l(x_1)}\right), \tag{3.14}$$

where $x_{1,2} = \omega r_{1,2}/c,\ \omega = l\omega_0,\ J_l\ and\ Y_l$ are Bessel functions of the 1st and 2nd kind respectively and for perfectly conducting walls at $r = r_w$: $(r_w = a \text{ or } b)$, $C_1/C_2 = -Y'_l(x_w)/J'_l(x_w)$. The numeric admittance values b_+ and b_- for beam energy of 51.1 keV are $b_+ = 1.295,\ b_- = 1.126$, and $(b_+ + b_-) = 2.421$, and for beam energy of 511 keV are $b_+ = -17996,\ b_- = 1.77616$, and $(b_+ + b_-) = -17994.2$. The parameters used in these simulations are $l = 6$, $\tau = 2$ mm, $r_b = 10$ cm, $n = 6.25 \times 10^8$ cm^{-3} . The top of Figure 3-7

shows the azimuthal electron current for the case of $h = -0.5$ which shows a clear beating of two frequencies. The frequencies can be solved using equation (3.15).

$$\omega_{\pm} = l\omega_0 \pm \sqrt{\left(\frac{l\tau}{r_b}\right)\left(\frac{e^2 n}{\epsilon_0 m_{eff}}\right)\left(\frac{1}{b_+ + b_-}\right)}. \tag{3.15}$$

For the positive mass cases shown in Figure 3-10, $h = -2, -1$, and -0.5, the observed oscillation frequency and the frequency predicted by equation (3.12) are given in Table 3-2. The positive and negative sign in Figure 3-10 and Table 3-2 refers to, respectively, the two frequencies obtained from equation (3.12) given by $\omega_{\pm}$ in equation (3.15). The MAGIC frequencies are extracted from the electron current by taking the fast Fourier transform (FFT) of the current trace, Figure 3-9, the error bars show the FFT frequency resolution. There is good agreement between the frequency observed in the simulations and that predicted by equation (3.15).

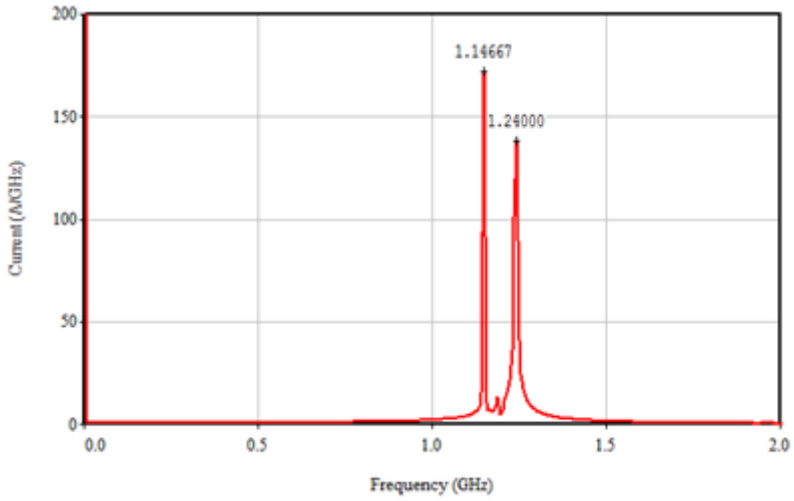

Figure 3-9. FFT of positive mass oscillation in MAGIC.

Table 3-2. Positive mass electrostatic oscillation frequency

h	m_{eff}/m_0	Theory +	Theory -	MAGIC +	MAGIC -	σ +	σ -
1.680	1.232	1.155	1.233	1.140	0.007	0.003	1.680
1.330	1.237	1.150	1.240	1.147	0.007	0.003	1.330
1.730	1.232	1.155	1.233	1.153	0.007	0.003	1.730

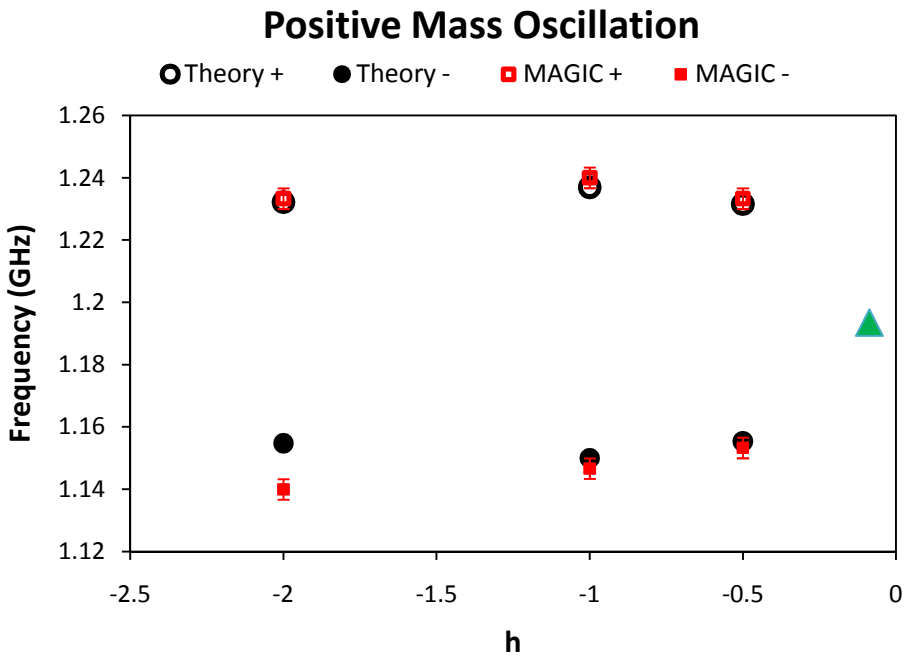

Figure 3-10. Frequency of oscillation for positive mass cases. The black circles are the frequencies from equation (3.15) and the red squares are the frequencies extracted from the FFTs in MAGIC. The location of infinite effective mass is shown by the green triangle

3.5 Negative Mass Growth

The negative mass simulations, $h > -\beta_{\perp}^2/2$, show growth of the initially seeded density perturbations (cf. Figure 3-3). The perturbations grow by particles moving to larger radius and falling back in θ, or moving to smaller radius and moving forward in θ into the same azimuthal phase as the regions of peak density, this particle rearrangement in r is what allows for bunching in θ (cf. Figure 3-1). Figure 3-11 shows the negative mass

instability in the inverted magnetron configuration with $h = 2$, this corresponds to the current trace in the bottom of Figure 3-7. In analyzing the dispersion relation given by equation (3.12) the growth rate of the instability can be determined. For $m_{eff} < 0$ the square root in equation (3.15) becomes imaginary

$$\omega = l\omega_0 \pm i\sqrt{\left(\frac{l\tau}{r_b}\right)\left(\frac{e^2 n}{\epsilon_0 |m_{eff}|}\right)\left(\frac{1}{b_+ + b_-}\right)}. \tag{3.16}$$

The negative imaginary component of this equation will lead to growth in the exponential description of the wave, $e^{i\omega t - il\theta}$. The growth rate ω_i is given by the imaginary component of equation (3.16).

$$\omega_i = \sqrt{\left(\frac{l\tau}{r_b}\right)\left(\frac{e^2 n}{\epsilon_0 |m_{eff}|}\right)\left(\frac{1}{b_+ + b_-}\right)} \tag{3.17}$$

The growth rates from the simulations are derived from the exponentiation time of the peaks in the azimuthal current, bottom of Figure 3-7. An exponential function was fit to the peaks in the azimuthal current density from time $t = 0$ and when the current exceeded 36 A. The 36 A point was chosen somewhat arbitrarily to be much lower than saturation current but large enough to give at least four points for the fitting of the exponential function. The electron plots for $h = 2$ is shown in Figure 3-11. The normalized growth rates extracted from the simulations are compared to the theoretical rates from equation (3.17) in Figure 3-12 for $h = -0.05,\ 0,\ 0.5,\ 0.826\ (= 1/\gamma^2),\ 2$, and 3. The error bars indicate the standard error for the normalized growth rates from the exponential fitting parameter. The

error bars in Figure 3-12 are derived from the uncertainty in the exponential fitting parameter [46]. The numerical values used in Figure 3-12 are listed in Table 3-3.

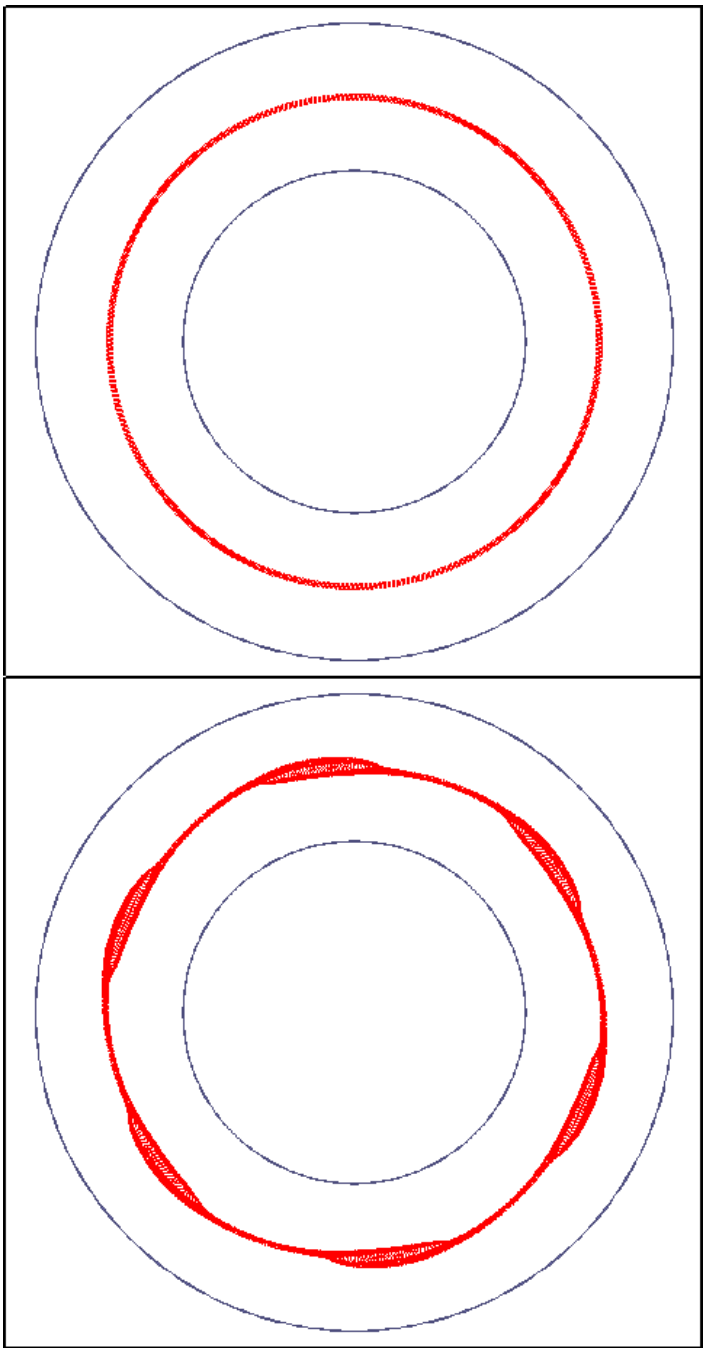

Figure 3-11. Electron beam at 0.2 ns [top] and 11.5 ns [bottom] for the inverted magnetron configuration ($h = 2$) showing negative mass behavior.

Table 3-3. Growth rate data from theory and MAGIC with the error in MAGIC

h	Theory (ω_i/ω_0)	MAGIC (ω_i/ω_0)	MAGIC σ (ω_i/ω_0)
-0.05	0.011	0.014	0.001
0	0.017	0.019	0.002
0.5	0.038	0.039	0.014
0.826 $(h = 1/\gamma_0^2)$	0.040	0.045	0.013
2	0.034	0.035	0.007
3	0.029	0.022	0.001

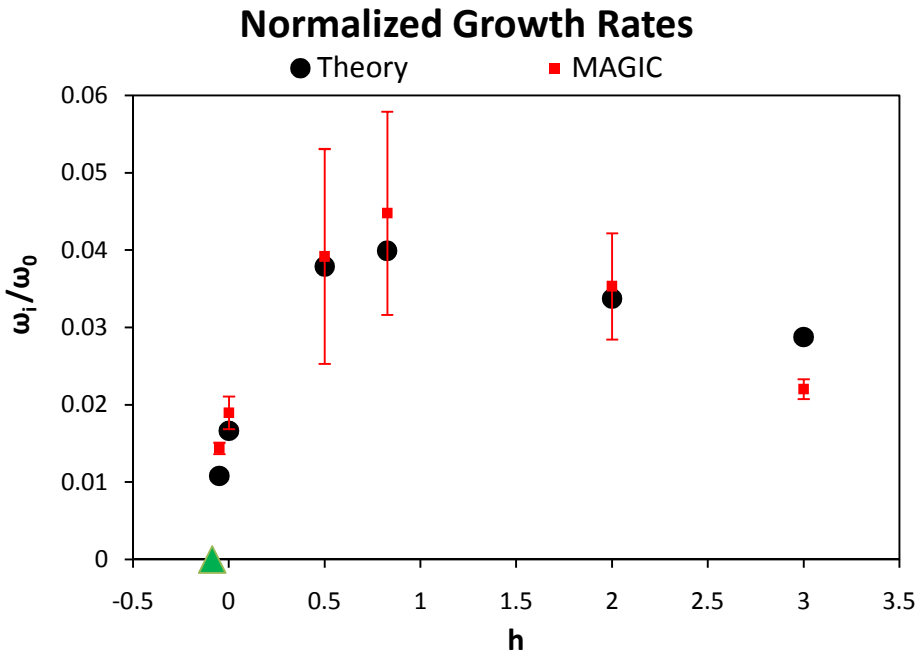

Figure 3-12. Normalized growth rates from theory (black) and derived from MAGIC (red). The location of infinite effective mass is shown by the green triangle

3.6 Infinite Mass

The infinite mass configuration occurs when $h = -\beta_\perp^2/2 = 0.0868$ for the parameters of this simulation, equation (3.7). The expected result of the infinite mass configuration is that initial density perturbations will not grow or oscillate, but rather persist indefinitely. Examining the dispersion relation given by equation (3.12), as the effective mass goes to infinity the right side goes to zero. The dispersion relation will then simply be $\omega = l\omega_0$, and the beam will simply maintain its orbit with azimuthal mode l.

For the 51.1 keV beam, the infinite mass configuration shows some mild growth; however, when the beam energy is increased to 511 keV, the beam shows no growth or oscillation for the entirety of the simulation, Figure 3-13. The current for the 511 keV beam is approximately twice as large as the 51.1 keV beam and the velocity is roughly twice as high. In comparing the m_0/m_{eff} plots for the two cases, Figure 3-14, it is clear that the 51.1 keV case is very close to $h = 0$. Recalling that $h \propto E$, the very small applied field (1 kV/cm) for the case of 51.1 keV indicates that self-fields will play an important role in the effective mass of the beam. Alternatively, the diocotron effect, which enters as a higher order correction to the dispersion relation (3.12), becomes important [23],[28], and this may be considered as the residual instability for the infinite mass case. For the 511 keV case, the applied electric field of 115 kV/cm is substantially greater than self-fields within the beam, therefore the beam displays the expected infinite mass behavior, and this residual instability is negligible. To verify that the growth was the result of self-fields, a 51.1 keV simulation was run with a nominal beam current 1/100th that of the previous runs and no growth was observed.

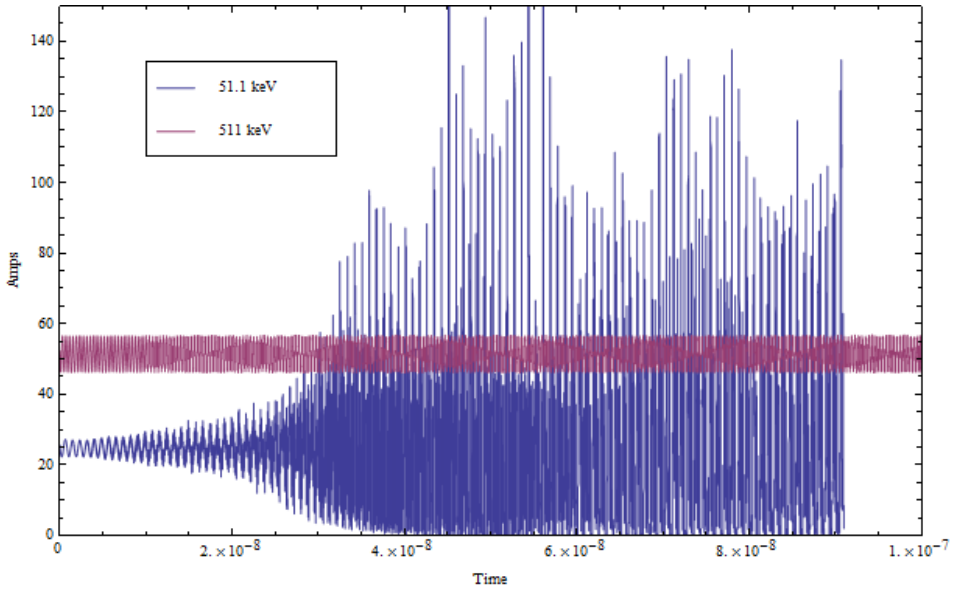

Figure 3-13. Azimuthal current measured for $h = -\beta_{\perp}^2/2$ $(m_{eff} = \infty)$ for beam energy of 51.1 keV, growing mode, and 511 keV, stable mode.

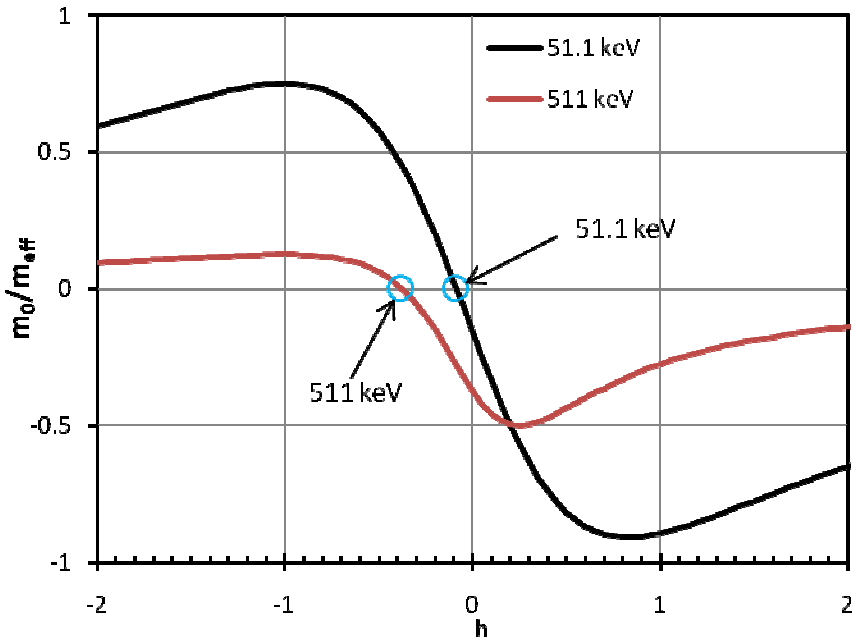

Figure 3-14. m_0/m_{eff} comparison for 511 keV and 51.1 keV

3.7 Conclusion

Particle-in-cell simulations were performed in MAGIC to analyze the stability of a rotating annular electron beam in a coaxial waveguide for general radial electric and axial magnetic fields. For the cases where the effective electron mass is positive, a beam seeded with an initial density perturbation will undergo electrostatic oscillations in the beam frame but maintain its annular shape. For negative effective mass, particle rearrangement will lead to azimuthal bunching of the beam about the regions of peak density reinforcing the initial azimuthal electric field perturbation. Electrons display infinite mass behavior when $h = -\beta_{\perp}^2/2$, where an initial density perturbation will persist. A condition for the infinite mass case is that the electric field contribution from space charge within the beam is negligible compared to the applied electric field. In this last case, even the resistive wall instability [47] is absent [23],[28], despite the appearance of complex impedances b_+ and b_- in equation (3.12) because of the finite wall resistivity.

CHAPTER 4

NONLINEAR TRANSMISSION LINES

4.1 Introduction

Nonlinear transmission lines (NLTLs) operated at high power levels have been a focus of intense research for a number of years [48]. Uses for such devices range from pulse risetime sharpening [20] to soliton generation [49]. In particular, generation of RF directly from square pulses remains of great interest for high power operation [17],[50],[18], as well as providing experimental evidence for such phenomenon as the inverse Doppler shift [51]. While NLTLs have a wide range of applications, their potential to build a high power microwave (HPM) source is attractive. Most existing HPM sources derive from vacuum electronic devices [1-3]. These sources require vacuum, magnetic field, and a high current electron source, as well as other ancillary devices, to produce microwaves. NLTL-based sources have an advantage over current HPM sources such as gyrotrons, magnetrons, and klystrons since the requisite extra hardware remains relatively small.

The two types of nonlinearities used in NLTLs are nonlinear capacitance, based on nonlinear dielectric materials or nonlinear semiconductor phenomena, and nonlinear inductance based on magnetic materials such as ferrite. In this chapter, three different nonlinear transmission line systems are explored: 1) a varactor-based, low voltage NLTL

driven by a benchtop pulser, 2) a ferrite based low impedance NLTL driven by a nominally 100 MW compact pulsed power driver, and 3) a nonlinear dielectric based NLTL driven by a 500 MW Blumlein line pulser. The three different lines all operated in different regimes of power, nonlinearity, and impedance, but are of the same basic design and operate under the same principles.

4.2 Varactor Based Nonlinear Transmission Line

This section details a series of experiments on low voltage, nonlinear transmission lines constructed from discrete L-C elements, with nonlinear capacitance being provided by varactors. While these types of lines have been extensively investigated in the past, the result of a time-frequency analysis for the evolution of the oscillating pulse along the transmission line is presented. It is demonstrated that the waveforms generated on the line have an oscillatory nature with frequency given by characteristic L and C on each unit and that these waveforms can be extracted into a load. The experimental results are confirmed with circuit simulations. Additionally, two general criteria for the frequency of oscillation and the risetime necessary to generate these oscillations are found. This work comprises the initial steps in understanding how complex waveforms generated in such nonlinear transmission lines can be coupled effectively to a load, whether a simple resistive load or an antenna structure.

Briefly, the nonlinear transmission line (NLTL) considered in this section operates as follows and appears schematically in Figure 4-1. A large amplitude square pulse is injected into the input terminals of the NLTL. “Large” in this case implies of sufficient amplitude to

push either the inductive or, in the case considered here, the capacitive elements, into their nonlinear regime. One clear result of this scenario consists of pulse sharpening of the input waveform due to the nonlinearity [20]. However, under the proper conditions, an oscillating waveform can also be generated.

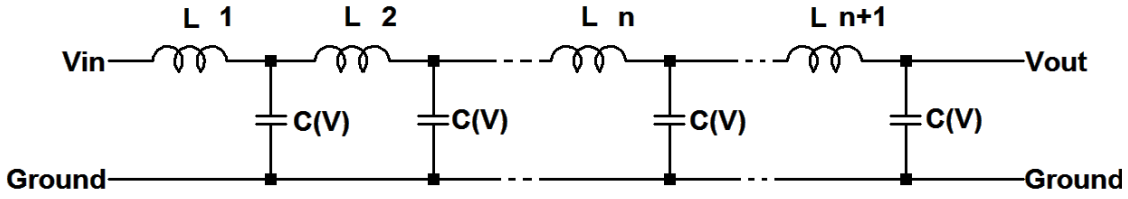

Figure 4-1. Schematic representation of a nonlinear transmission line (NLTL) with nonlinear capacitive elements. Since the capacitance depends on the voltage a signal in the NLTL will not be preserved as it moves down the line.

This section begins with a description of the experimental configuration, followed by an analysis and discussion of the results, particularly the time-frequency analysis. The time-frequency analysis presented here represents the first attempt to understand the temporal evolution of the harmonic content of such a system. In particular, the structure of the waveform indicates a harmonically oscillating waveform.

4.2.1 Experimental Configuration and Results

The experiments discussed here are performed on a discrete element transmission line that is built on a solderless prototyping board. The nonlinear transmission line circuit here can be considered a Type B pulse forming network which employs a nonlinear capacitive element [52]. The discrete element line consists of either 20 or 30 stages with a 1 μH inductor and a nonlinear capacitor (varactor) MV209. Figure 4-2 shows the voltage dependence of these capacitors. The varactor is a semiconductor device where the depletion

layer thickness provides the capacitance. Since this thickness depends upon the applied voltage the capacitance is a function of voltage and these can be used as a nonlinear capacitive element in the NLTLs.

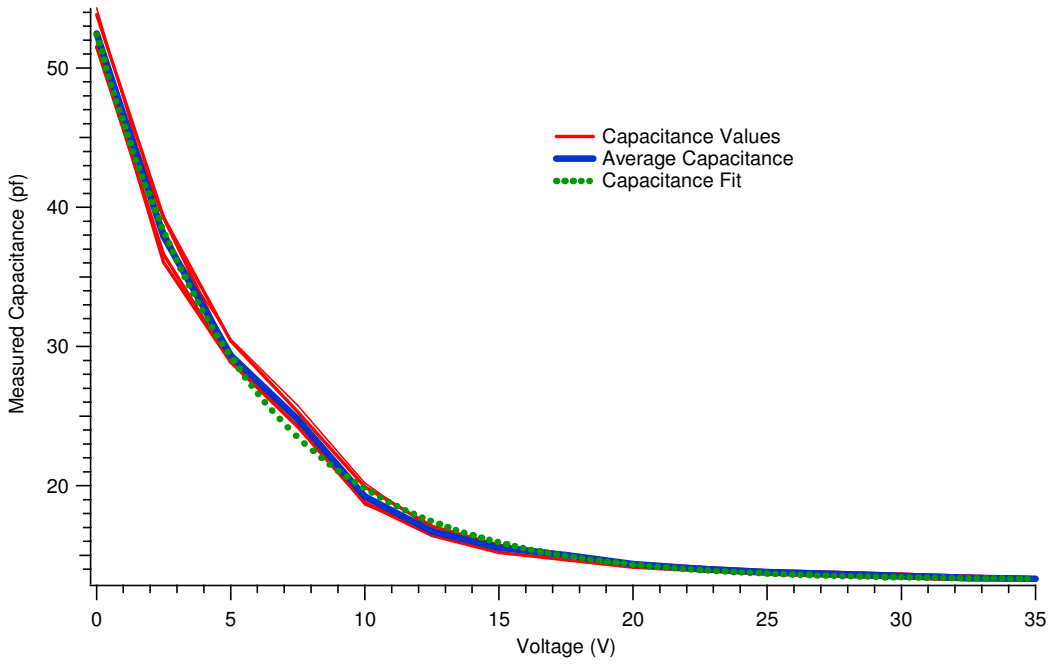

Figure 4-2: Voltage dependence of the capacitors. The red traces show the capacitance of ten individual capacitors, with the average capacitance shown in blue and a least squares fit to the data shown in green [53].

The red traces show the capacitance of ten individual capacitors sampled at random from the lot of 30. The average capacitance appears in blue and a least squares fit to the data in green. Note that the capacitance clearly decreases with increasing voltage, following an approximately exponential decrease as demonstrated using the least squares curve fit. A Berkeley Nucleonics Model 565 Digital Delay Generator was used to drive the NLTL, with the line connected to the generator using a 50 Ω cable. The output of the line is terminated at 50 Ω into a Tektronix TDS3052 oscilloscope. To show that the RF signal generated could

be extracted into a load, a transit-time isolated measurement into the 50 Ω termination of the oscilloscope was made through 300 ns of RG58 cable, shown in Figure 4-3.

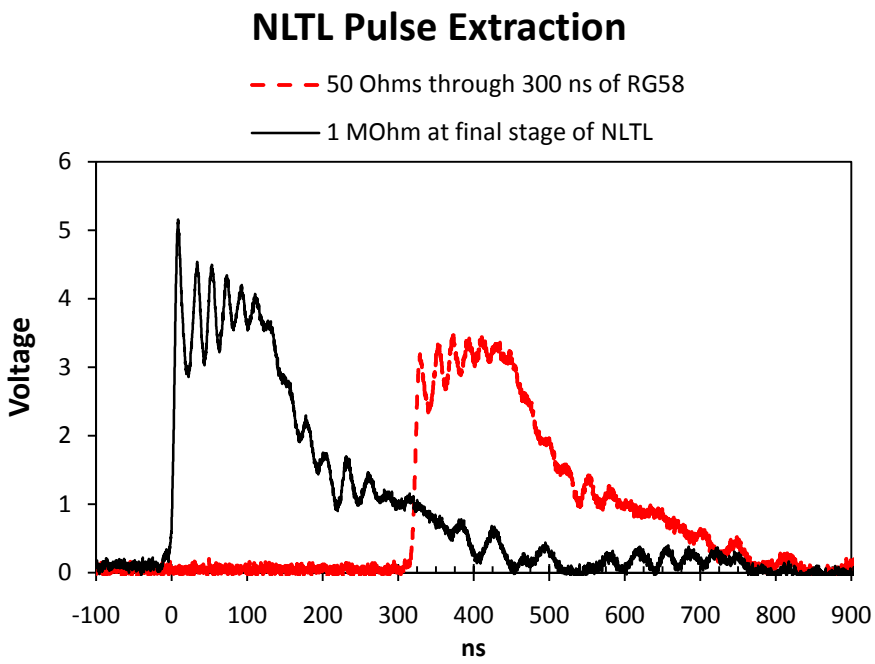

Figure 4-3: The dotted trace shows the extracted signal through 300 ns of RG58 cable. The waveform generated here is less than the Bragg frequency, π phase shift per stage, and is therefore the passband of the NLTL. Signals generated at the Bragg frequency have zero group velocity and therefore cannot be extracted.

Experiments were performed on two separate lines of 20 and 30 sections each. Each line had the same inductors and nonlinear capacitors. Using the 20 section line in order to verify the pulse sharpening effect of the nonlinear line, we increased the risetime of the pulse from the 10 nanoseconds available from the source to 100 nanoseconds through the addition of series inductance. As shown in Figure 4-4, the leading edge of the long risetime pulses sharpens from 100 ns to approximately 10 ns after passing through 20 stages. Since the velocity on the transmission line is dependent upon the voltage, the peak of the pulse catches up to the beginning of the pulse while outrunning the tail of the pulse. This generates a shock front at the beginning of the pulse and a long tail at the end of the pulse,

as shown in Figure 4-4 and Figure 4-6. We note also that oscillations begin to develop along the output pulse as it terminates in the load region. However, as demonstrated below, when pulses are injected directly from the generator with 10 ns risetime, deeper modulation of the top of the pulse occurs as the pulse travels down the line.

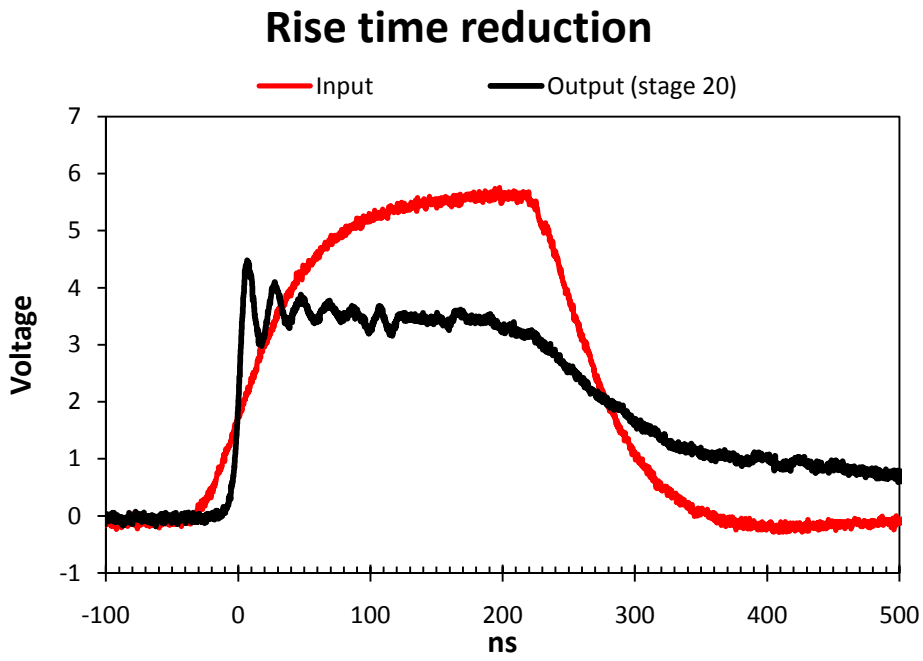

Figure 4-4: Pulse sharpening of a 100 ns risetime pulse to 10 ns risetime after a 20 stage NLTL (the output trace has been shifted in time). Note also the beginning of oscillations along the pulse at the output.

In addition to the pulse sharpening seen for the 20 section line, a 30 section line was also constructed. Figure 4-5 depicts the output measurements from this NLTL as stages are added to the system. We note here that at least 20 stages are required to achieve "clean" modulation of the fixed duration input pulse, corresponding to the transit time of the pulse through the NLTL. To better understand the frequency content of the waveform, we performed a time-frequency analysis (TFA) of this data, a common technique for waveform analysis in the HPM field [54]. Figure 4-7 shows the results of this analysis as well as a

standard fast Fourier transform (FFT) of the signal. The primary frequency of oscillation ranges from 45-50 MHz. Notably, this value is approximately equal to the characteristic frequency of the transmission line assuming a saturated capacitance, whose theoretical value is $1/2\pi(LC_{sat})^{1/2}$, or about 44 MHz.

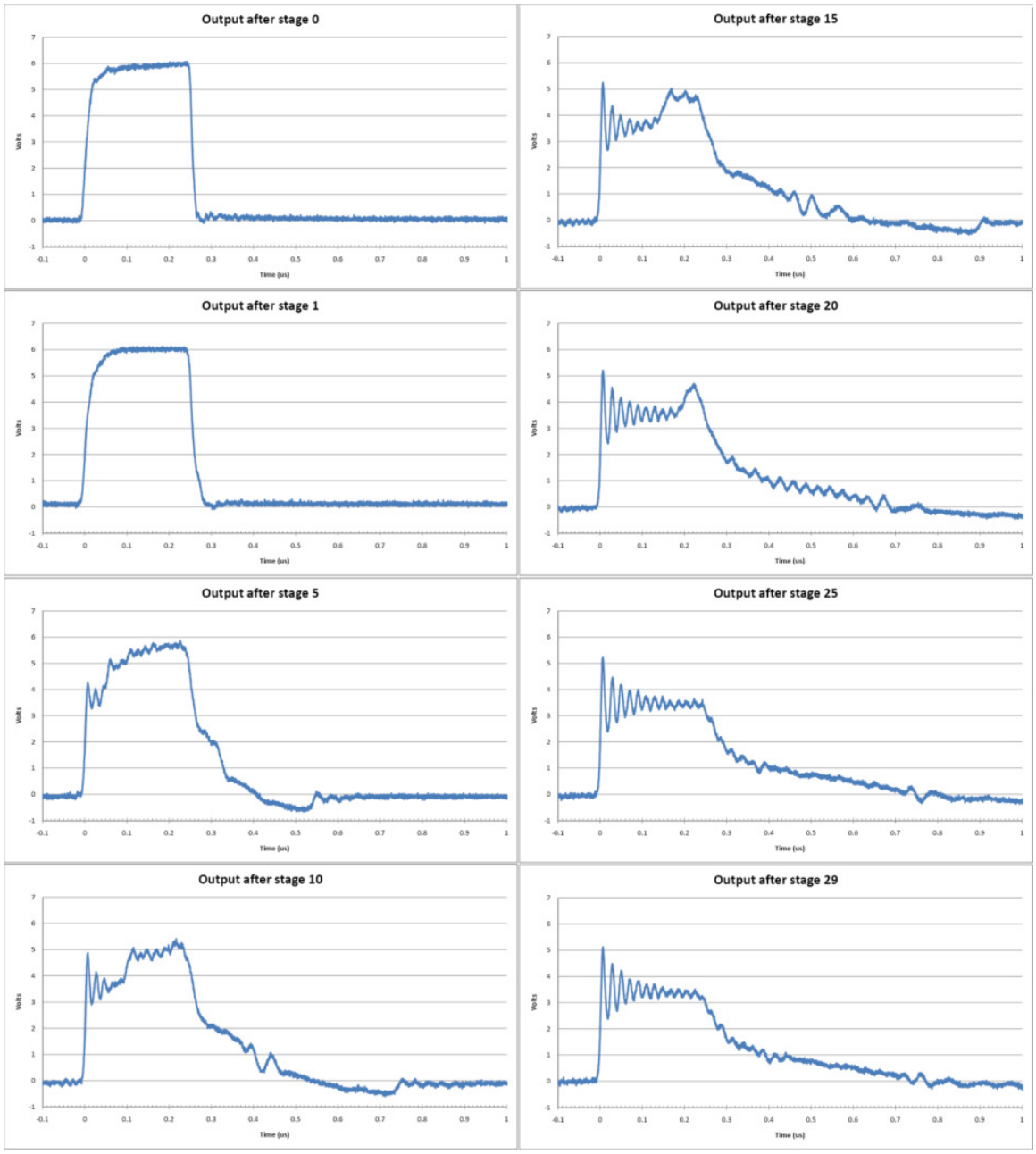

Figure 4-5: Output of NLTLs comprised of different numbers of LC stages for a fixed duration input pulse. The input pulse (top left) is 6 Volts in amplitude and 250 ns in duration. Note the changes in the characteristics of the voltage as one adds more stages to the line.

4.2.2 Simulation Results

In order to make comparisons of basic circuit models to the experiment, circuit simulations were run using LTspice [55]. As shown in Figure 4-6, circuit simulations clearly show both the sharpening of long risetime pulses and RF modulation on the tops of pulses.

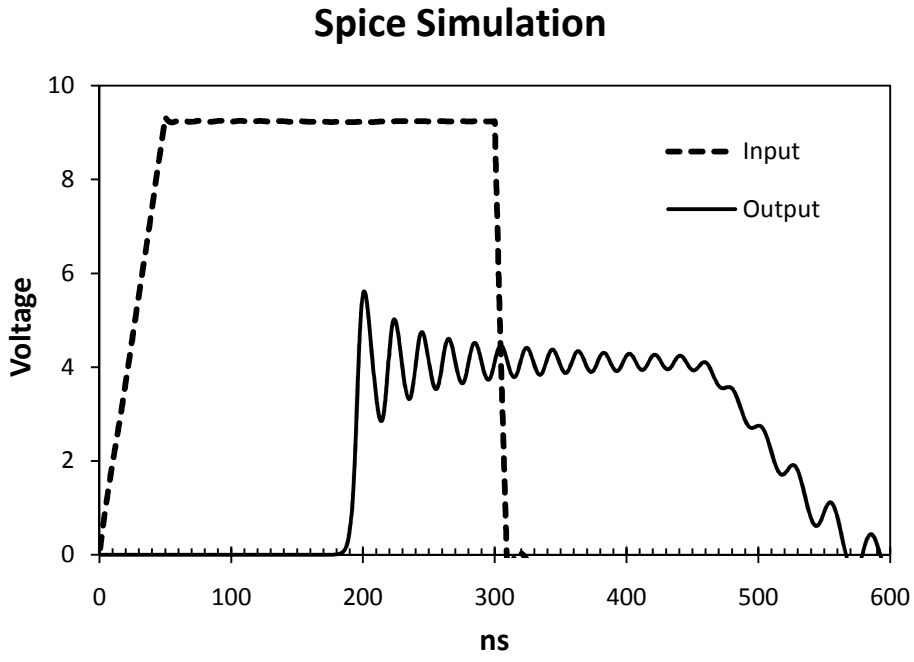

Figure 4-6: LTspice [55] simulation showing the input (dashed line) and output (solid line) of a 30 stage NLTL having the same inductance and nonlinear capacitance as the experiment (no loss is included in this simulation).

The risetime of the injected pulse clearly influences whether RF generation occurs. Simulation results show that if the injected pulse risetime is less than about half of the unsaturated RF period, the voltage waveform shows little to no modulation. Figure 4-4, Figure 4-5, and Figure 4-7 demonstrate this result experimentally. Several oscillations can be seen in the pulse sharpening experiment in Figure 4-4; however, these do not appear to be as pure in frequency and are not as strong as the oscillations seen in the longer lines of Figure 4-5 and Figure 4-7. The risetime threshold for RF generation is important to note as

the injected pulse risetime will need to be faster than this for effective oscillations to develop. This condition may require very fast drivers for generation at high frequencies, placing constraints on the driver technology.

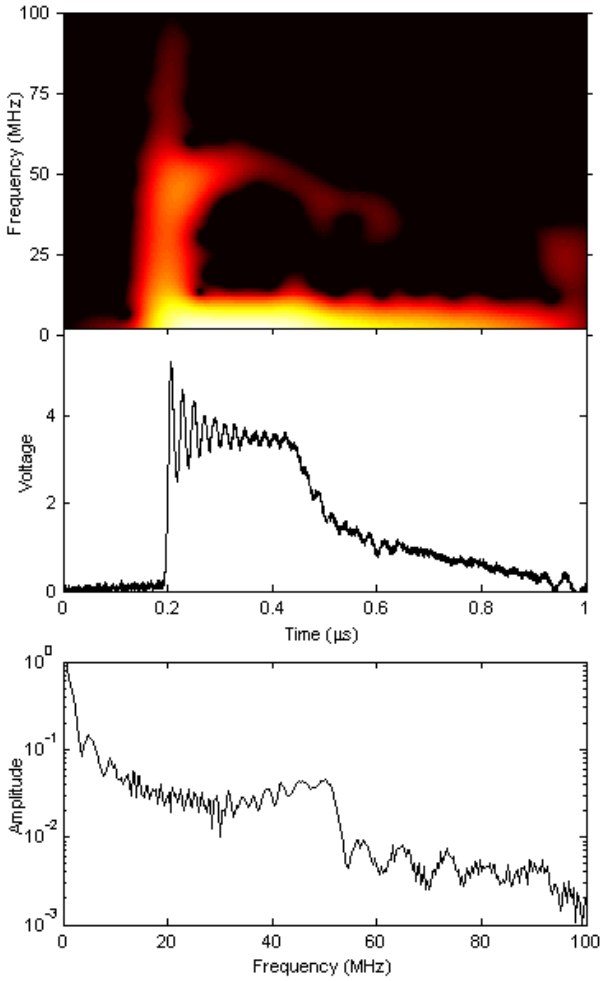

Figure 4-7: Upper plot shows time frequency analysis (TFA) of the NLTL output trace, shown in center plot. The lower plot shows an FFT of the NLTL output trace. The TFA plots show a large amount of spectral content at the shockfront followed by a relatively pure signal at ~50MHz from 200 to 400ns.

Additionally, a series of parameter scans were performed to develop intuition for the behavior of the RF signal and the risetime necessary to initiate generation of periodic modulation. In particular, it was discovered that the RF energy was generated at a frequency consistent with a unit cell of the capacitance/inductor for our transmission line

where the capacitance is the saturated value due to the nonlinearity. As an example with the experimental values, C(saturated) = 13 pF and L = 1 uH, the resulting RF oscillation should be at 44 MHz, which agrees with both the experimental results and the simulation data. Additionally, the risetime of the DC driving pulse was systematically varied to find the threshold for RF generation. RF generation occurs when the risetime is faster than the period of fully linear (zero voltage) capacitance of the unit cell capacitor/inductor. Again, using the experimental values as an example, the zero voltage capactance of C(cold) = 53 pF and L = 1 uH suggests an RF period of the unit cell equal to 45 ns, which is in excellent agreement with the threshold rise time of 50ns. In short, our study leads to these general criteria: (a) the RF generated by a NLTL is at the resonant frequency associated with the saturated capacitance, and (b) the critical risetime to generate RF occurs when the risetime is faster than the RF period of the fully linear ("cold" or "zero voltage") capacitance.

4.2.3 Discussion and Conclusions

An oscillating waveform generated on the NLTL was extracted into a transit-time isolated 50 Ω load. It was demonstrated that the oscillations correspond roughly to the frequency dictated by the capacitance of the saturated line. A condition for generating oscillations consists of having a sufficiently rapid risetime. Importantly, these two facts lead to two general criteria that one can employ for NLTL design of a nonlinear capacitor-based system. First, a critical risetime exists for the generation of RF. The risetime must be less than that of the RF period associated with the fully linear (“cold” or “zero voltage”) capacitance of a single section of the NLTL. Second, the RF generated by this pulse occurs at

the frequency associated with the saturated capacitance of a single section of the NLTL. These two general criteria provide the initial tools necessary for NLTL design and place constraints on the output available from the nonlinear capacitor-based lines in this study.

4.3 Ferrite Based Nonlinear Transmission Lines

In this section, we report the ferrite NLTL experiments at UM on a discrete element nonlinear transmission line using nonlinear inductance with input powers of 100 MW. Pulse sharpening of multi-kA input pulses has been observed in addition to the generation of oscillations at the characteristic L-C frequency.

4.3.1 Basic Analytic Scaling

From the study of section 4.2, it is natural to expect that the frequency of NLTL output is the characteristic frequency of the L-C system assuming saturated nonlinearity, inductance or capacitance, $f = 1/2\pi(\mathrm{L_{sat}C_{sat}})^{1/2}$. Setting this frequency equal to the desired frequency one can solve for the saturated capacitance and saturated inductance as a function of impedance, $L = Z/2\pi f, C = (1/Z)(1/2\pi f)$, where $Z = (L/C)^{-1/2}$ is the characteristic impedance of the L-C circuit. The scaling shown in Figure 4-8 for a frequency of 1 GHz indicates that for an impedance of 1 Ω, the per-stage inductance and capacitance must be 160 pH and 160 pF respectively. While this capacitance is easily achievable, the inductance may not be achievable experimentally. The requirement for large anode-cathode spacing in order to be capable of holding off high voltage and the small anode-cathode spacing necessary for low inductance make this scaling unfavorable. The most successful

ferrite based NLTLs constructed thus far are 25 Ω and use a slightly different circuit that includes capacitive crosslinks between every other stage [18].

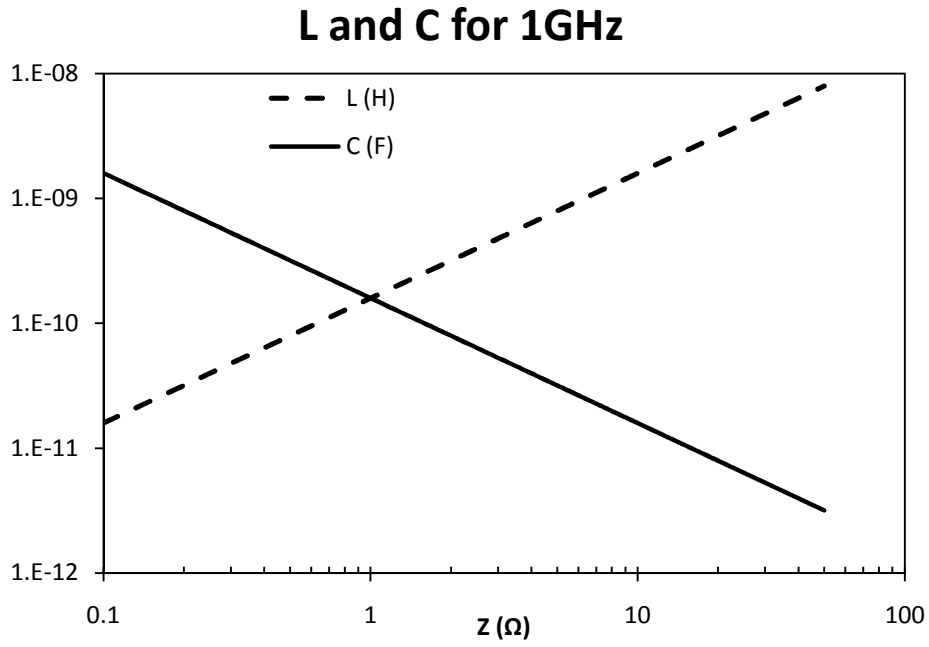

Figure 4-8. Scaling of L and C with impedance for a fixed frequency of 1 GHz.

4.3.2 Experiments

Several ferrite nonlinear transmission line circuits have been constructed at UM for the purpose of finding general scaling laws for RF generation at high power levels. In particular we examine the feasibility of a low impedance NLTL. For a given power, a low impedance circuit operates at a lower voltage than a high impedance circuit, which may be advantageous at high power levels. The circuits are built as discrete element L-C transmission lines where the inductance is nonlinear due to the presence of ferrite beads over an inductive interconnect. The driver used for the circuits is a nominally 100 MW, 1 Ω, 10 kV, 10 kA spark-gap switched circuit with a rise time of 175 ns into a matched load. The

driver circuit contains an internal 1 Ω resistance as the output is typically used to drive a short circuit load for the calibration of current diagnostics. A current trace with the output shorted is shown in Figure 4-9.

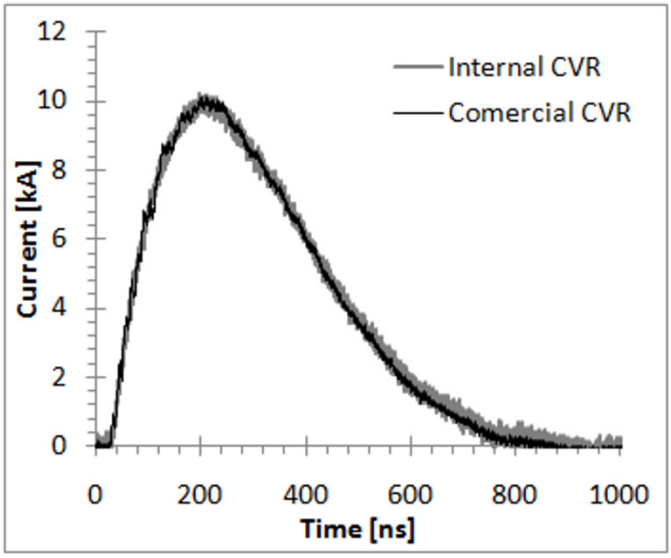

Figure 4-9. Output into a short (driver contains an internal matched resistive load).

The first UM ferrite NLTL was built as a proof of concept to determine if pulse sharpening and RF generation was achievable with a low impedance circuit with the slow risetime of the available driver. The circuit was built using doorknob style high voltage capacitors and NiZn ferrite beads. The 9 stage circuit uses 3 nF capacitors for the first 3 stages, 1.5 nF capacitors for the next 2 stages, and 0.5 nF capacitors for the last 4 stages, Figure 4-10. The tapering of the impedance and characteristic frequency was done out of convenience as these capacitors were on hand. The per stage inductance of this circuit at zero current and when saturated was approximately 2 μH versus 40 nH respectively. The ground plane of the circuit was a 100 × 0.75 mm strip of copper. The ground sides of the capacitors were screwed into the copper sheet and the high voltage side was attached to a

11.1 mm brass rod around which the ferrite beads were located. The circuit was terminated into a nominally 1.6 Ω load consisting of two 3.2 Ω carbon resistors. The voltage across the load was measured with a high voltage probe and the current was measured with a commercial current viewing resistor. A photograph of the circuit is shown in Figure 4-10. The voltage and current were measured for cases with versus without a pre-shot reset current. If the ferrite cores in the line are driven into reverse saturation and left at the bottom remnant point in the hysteresis curve, the sharpening of the incoming current rise to 2 kA occurs in less than 20 ns and generation of oscillations is very apparent (top of Figure 4-11). The bottom graph in Figure 4-11 shows the same NLTL with no reset current; thus the cores are left at the top remnant point of the hysteresis curve. In this case, fewer oscillations are seen and the current rise is much slower, not reaching 2 kA until approximately 50 ns.

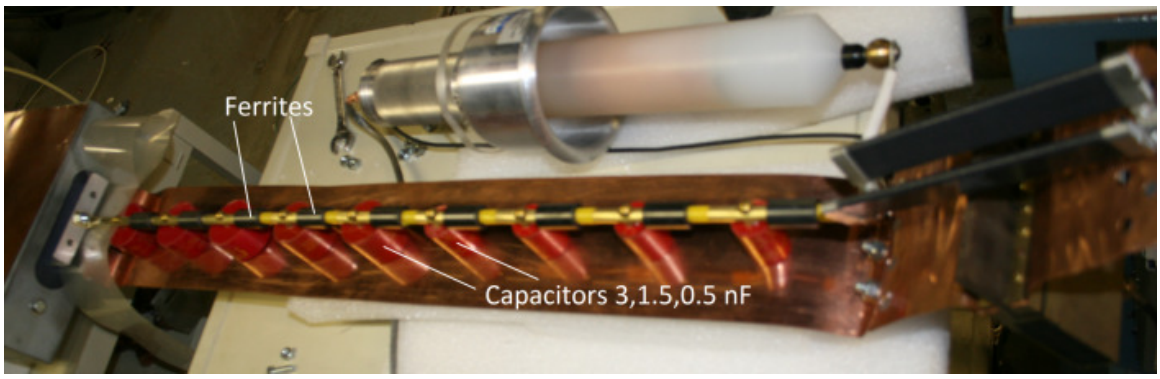

Figure 4-10. Low impedance proof of concept line.

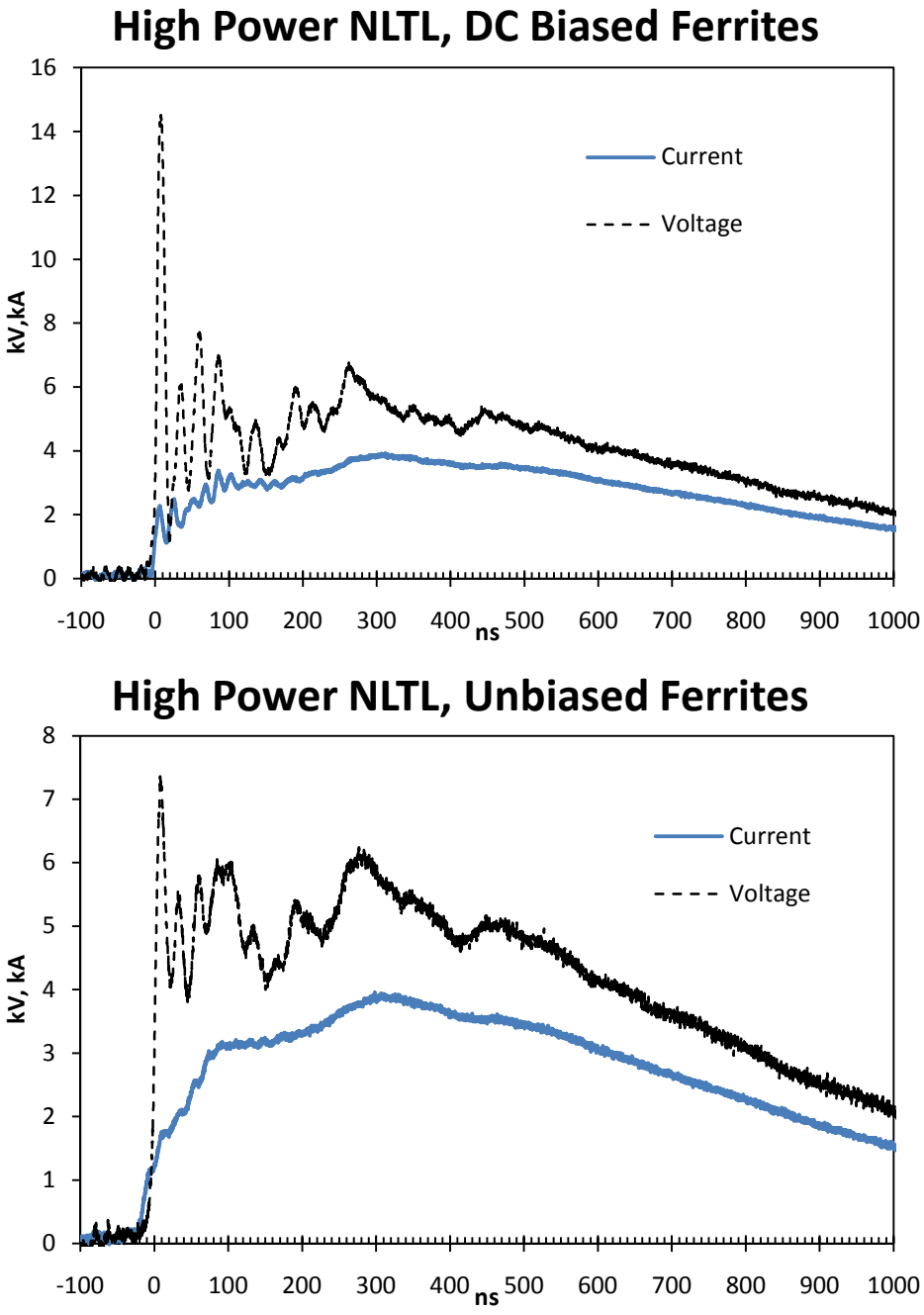

Figure 4-11.Voltage and current traces from proof of concept line with cores reset (top) versus not reset (bottom).

The second UM ferrite NLTL that was built had 24 L-C stages in order to increase the number of oscillations, as well as the depth of the oscillations, shown in the waveforms in Figure 4-12. This circuit was similar to the one shown in Figure 4-10 but used 1 nF

capacitors and a slightly different geometry that resulted in a saturated inductance of 21 nH. The ferrites used for this line were MnZn and gave a zero current inductance of approximately 6 μH per stage. The spatially uniform impedance and characteristic frequency of this NLTL resulted in approximately 10 oscillations at a frequency of 36 MHz. This closely agrees with the predicted frequency of 34.7 MHz using the simple relation $f = 1/2\pi(L_{sat}C)^{1/2}$ with the measured L_{sat} and C. The average power of the RF oscillations in the signal was 1.4 MW.

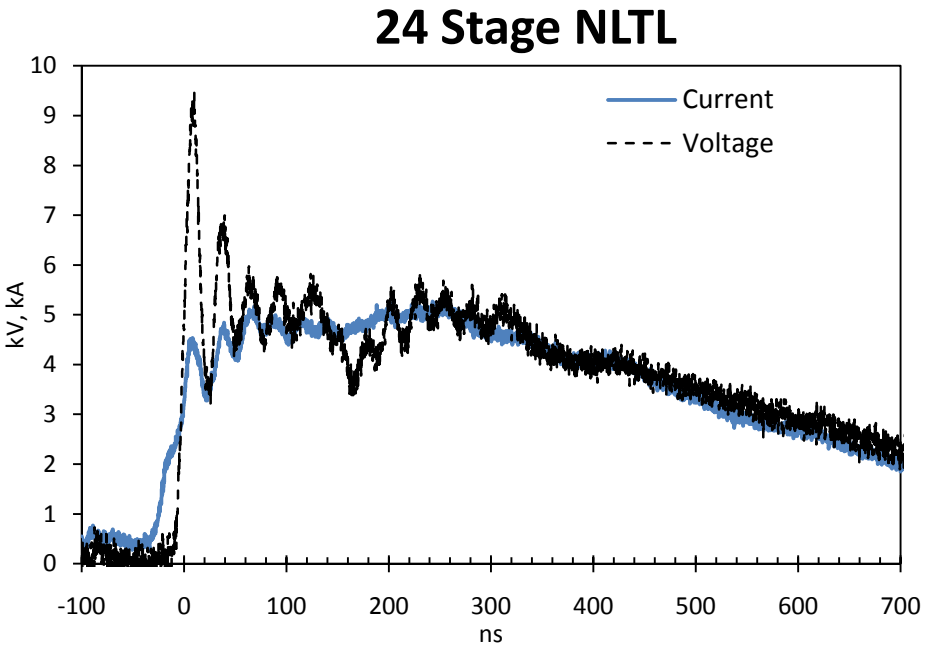

Figure 4-12. Output voltage and current of 24 stage ferrite NLTL.

4.3.3 Conclusions

NLTL circuits using ferrite inductors have successfully been built and tested at MW power levels. The circuits described here were limited to low frequency due to the slow available driver and the low impedance, requiring high capacitance values. The relatively

simple scaling using characteristic L-C frequency (assuming saturated impedance) also describes the output frequency of the NLTLs considered here. The unfavorable scaling of frequency with impedance appears to make low impedance, high power, GHz frequency NLTLs that use ferrite nonlinearity somewhat impractical.

In both the capacitive and inductive NLTLs the RF signal has approximately a damped sine shape. The efficiency measurements are made from the shockfront to the 1/e point in the RF signal. Both the simulated and experimental nonlinear capacitive line have RF efficiencies of ~5%. The RF efficiency of the 24 stage ferrite NLTL is ~1%. These efficiencies are based on the ratio of the power in the RF part of the signal to that in the DC offset. The efficiencies of these lines are significantly lower than what is available from existing sources. Relativistic magnetron efficiency is typically on the order of 30% and conventional magnetron efficiency can reach 90% [2]. For these sources to compete with the existing sources the advantages such as no requirement for a vacuum or magnetic field, lighter weight, or simplicity to implement, would have to outweigh the significantly lower efficiency.

4.4 Nonlinear Dielectric NLTL (AFRL)

A nonlinear transmission line was constructed in a parallel-plate design, using nonlinear dielectric slabs as the nonlinear medium. The NLTL had 50 parallel-plate L-C sections spaced evenly along the length of the transmission line. Each L-C section was comprised of a parallel-plate region loaded with a nonlinear dielectric slab followed by an unloaded section which was filled with transformer oil in the experiment, Figure 4-13. The

dielectric slabs provide a nonlinear capacitance, and the gaps between provide linear inductive interconnects. This is essentially the same design used by Ikezi [49],[56]. In the basic circuit model used for this configuration the L and C values for a given stage are determined by calculating the L and C values of the capacitor region and inductor region and summing the two. The nonlinear dielectric material used for the capacitor regions was a lead-manganese-niobate ceramic made by the TRS company, designated PMN38 [57]. Originally designed for sonar transducer applications, PMN38 is known to have piezoelectric properties. The zero voltage capacitance of the PMN38 capacitors used for this NLTL is nominally 170 pF. The per-stage estimate of inductance (L) and capacitance (C) in transformer oil ($\varepsilon = 2.2$), based on geometric calculations, is summarized in Table 4-1. Table 4-1 also includes the characteristic frequency, $f = 1/2\pi(LC)^{1/2}$, and impedance, $Z = (L/C)^{1/2}$.

Table 4-1. Circuit parameters for NLTL with PMN38 capacitors. The zero voltage capacitance is measured and the saturated capacitance is an estimate based on data provided by the manufacturer. The inductance value is a geometric calculation.

Zero Voltage		Saturated	
L (nH)	13.22	**L (nH)**	13.22
C (pF)	169.48	**C (pF)**	51.00
f (MHz)	106.32	**f (MHz)**	193.82
Z (Ω)	8.83	**Z (Ω)**	16.10

4.4.1 Transmission Line Construction

The transmission line was built using two brass plates that have channels milled to index the capacitor location and to provide a good surface to epoxy the capacitors. A diagram of the transmission line is shown in Figure 4-13. The slab dimensions are 1.5x15x20 mm with the 1.5x15 mm faces metalized so that they can be epoxied to the brass. The

capacitors and brass plates were cleaned with alcohol before the dielectric slabs were bonded to the plates with conductive epoxy. Because the resistivity of the epoxy depends upon the temperature at which it is cured, after application of the epoxy and in order to achieve a low resistivity bond the assembled line was clamped together with metal clamps and baked at 105° C at a pressure of less than 100 μTorr for 24 hours. When the epoxy was cured, the vacuum baking system was then cooled to room temperature before being brought up to atmosphere and the line was quickly transferred to a plastic clamping assembly and placed under oil.

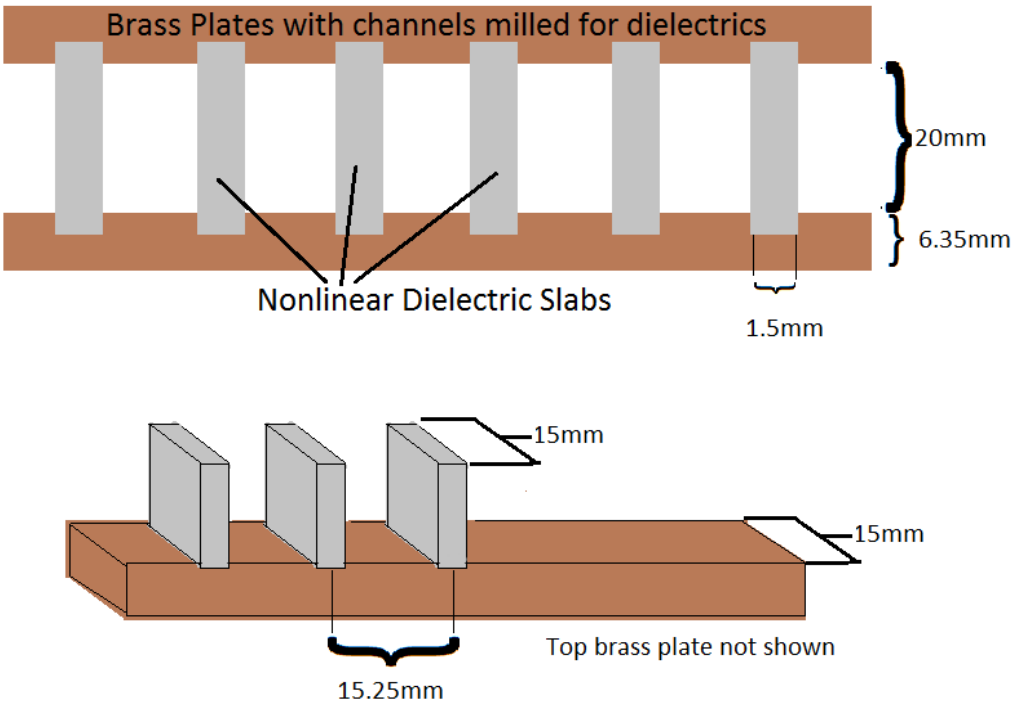

Figure 4-13. Parallel plate transmission line using the Ikezi geometry.

By minimizing the time the assembled and clean NLTL spent in ambient air, any absorption of moisture into the capacitors was minimized. This is an important consideration as any

surface contamination on the capacitors may lead to increased likelihood of surface tracking when high voltage is applied to the transmission line.

4.4.2 Transmission Line Driver

The transmission line was driven by a 6.25 Ω Blumlein pulse forming line that generates ~ 50 ns square pulses with ~ 6 ns rise and fall times at up to 50 kV. A diagram of the pulser with output into a 6 Ω load used for testing is shown in Figure 4-14. The pulser is operated in self break mode with a switch that uses high pressure dry air, the self-break curve for the air-gap switch is shown in Figure 4-15. The output of the pulser is connected to eight 50 Ω cables that attach to the input of the NLTL. A sample trace of the pulser output into a nominally matched resistive load is shown in Figure 4-16. The pulser is housed in an aluminum oil tank and the eight output cables connect to the NLTL experiment in an adjacent metal oil tank, shown in Figure 4-17 .

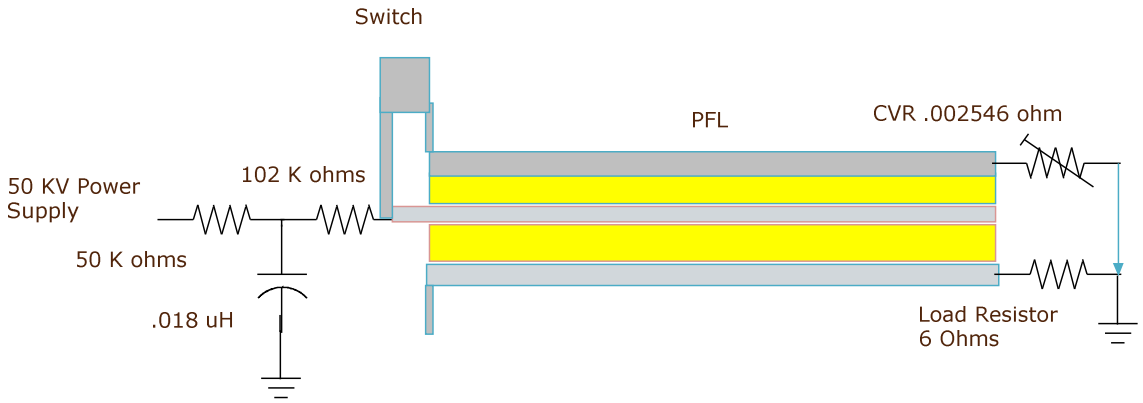

Figure 4-14. NLTL driver

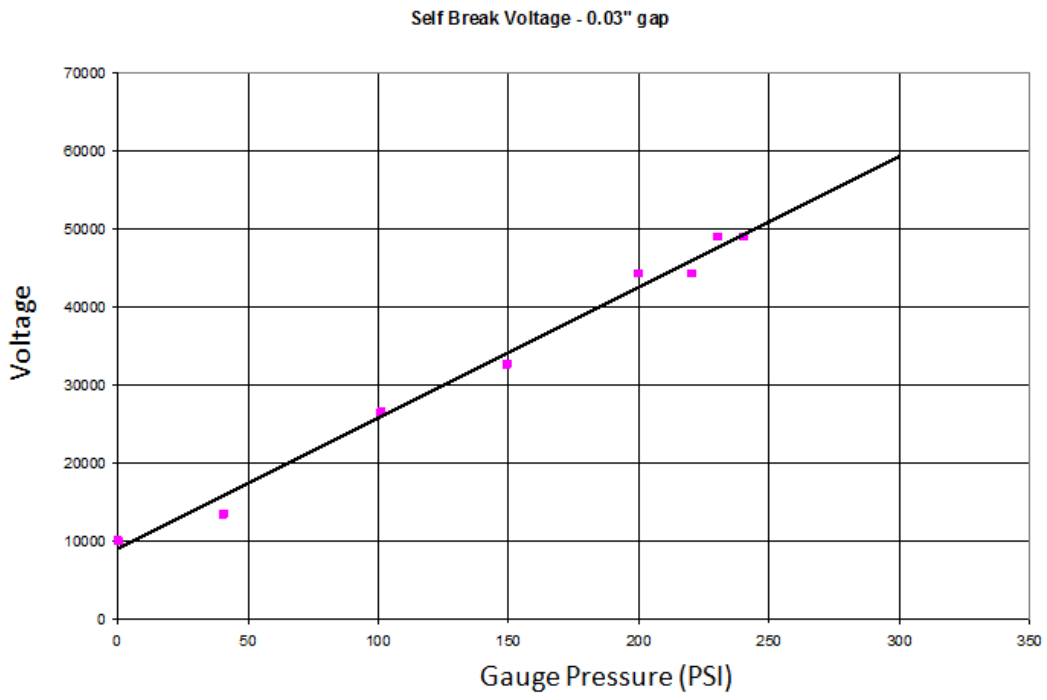

Figure 4-15. Driver switch self break voltage curve.

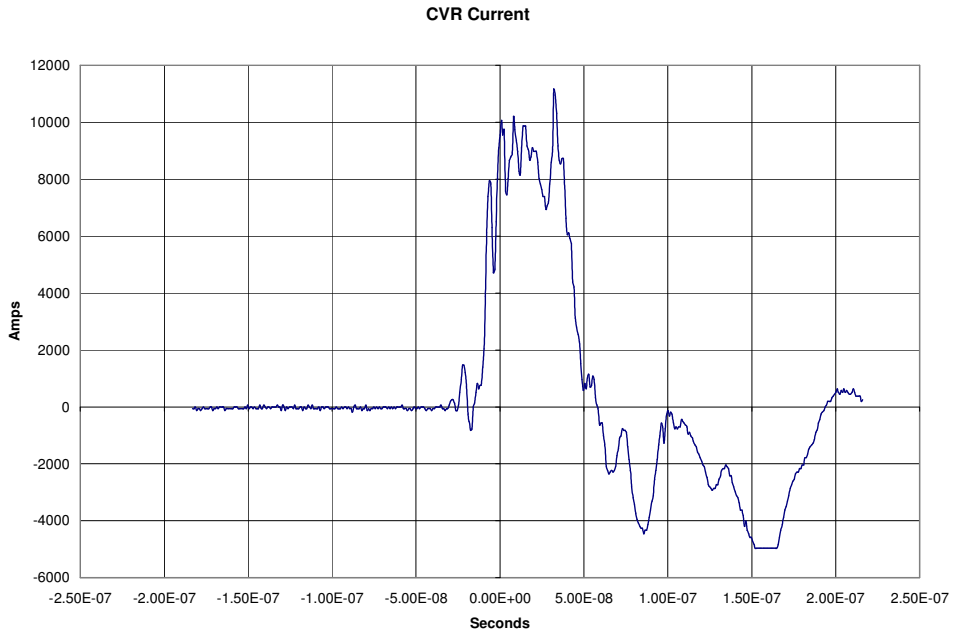

Figure 4-16. Pulser output current into a matched load.

Figure 4-17. Driver oil tank at top connected with eight 50 Ω cables to NLTL in adjacent oil tank at bottom.

4.4.3 Capacitor Modeling

The capacitance-voltage characteristic is determined by finding a functional form of the normalized dielectric constant and multiplying by a scaling constant determined by the measured capacitance at zero voltage. The functional form is a Lorentzian that was fit to the measured data using a slightly modified least squared minimization that more heavily weighted the points at higher voltages, as this is the region where RF generation would occur. Figure 4-18 shows the measured data and the functional fit.

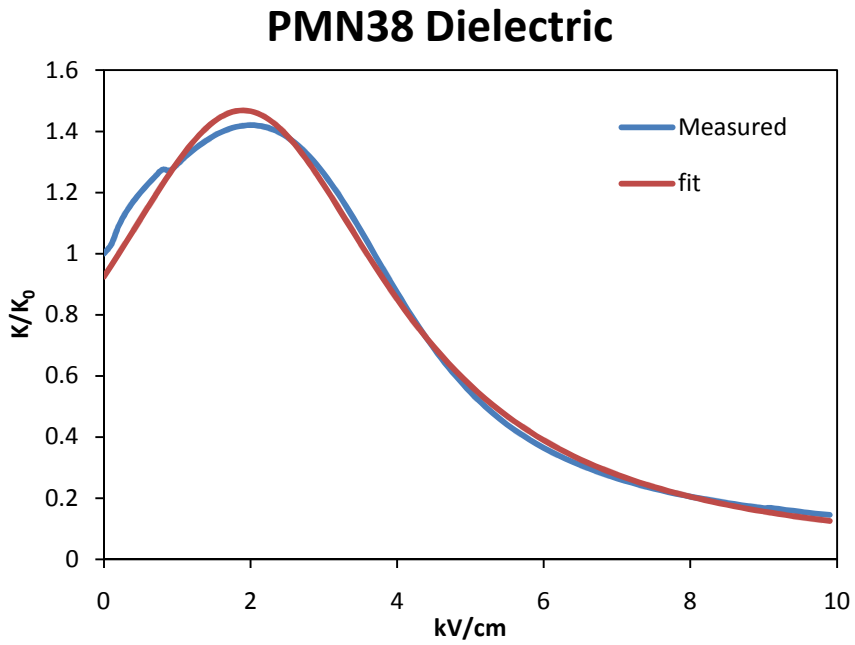

Figure 4-18. Fit to the PMN38 dielectric constant.

It is necessary to have function that can be analytically integrated so that the model can be put into LTspice [55]. LTspice has a nonlinear capacitance model that uses the functional form of the charge to determine the current and voltage on circuit elements. Equations (4.1) and (4.2) are the functions that are used in the LTspice model, the constants

are listed in Table 4-2. The absolute values for the voltage and the ratio V/|V| in the capacitance and charge models, equations (4.1) and (4.2), are used to correctly account for the sign of the charge in the LTspice model. C(V) and q(V) are plotted in Figure 4-19 and Figure 4-20, the functions are plotted up to 20 kV as this was the highest voltage for which measured data were available.

$$\mathrm{C(V)} = C_0 \left(\frac{\mathrm{c_1}}{\mathrm{c_2} + \left(\frac{\mathrm{c_3} - |\mathrm{V}|}{\mathrm{c_4}} \right)^2} \right) \tag{4.1}$$

$$\mathrm{q(V)} = \frac{V}{|V|} C_0 \left(\frac{(c_1 c_4)\mathrm{ArcTan}\left[\frac{c_3 - |\mathrm{V}|}{c_4 \sqrt{c_2}} \right]}{\sqrt{c_2}} - \frac{(c_1 c_4)\mathrm{ArcTan}\left[\frac{c_3}{c_4 \sqrt{c_2}} \right]}{\sqrt{c_2}} \right) \tag{4.2}$$

Table 4-2. Constant values used in C(V) and q(V).

Constant	Value
C_0	184.69 pF
c_1	80.53
c_2	54.79
c_3	3.8 kV
c_4	0.66 kV

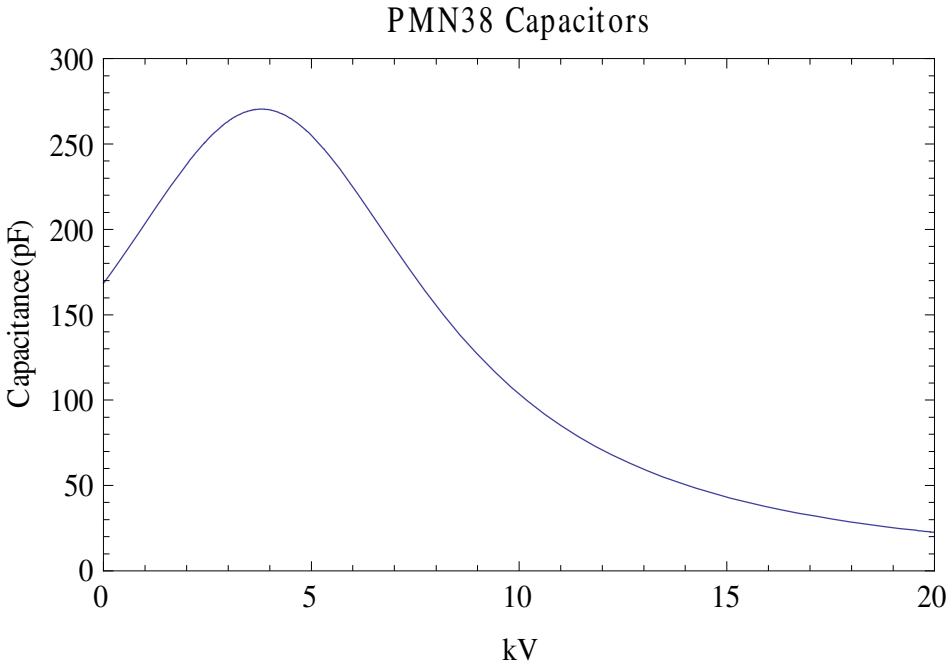

Figure 4-19. Capacitance function that is used in the LTspice circuit models.

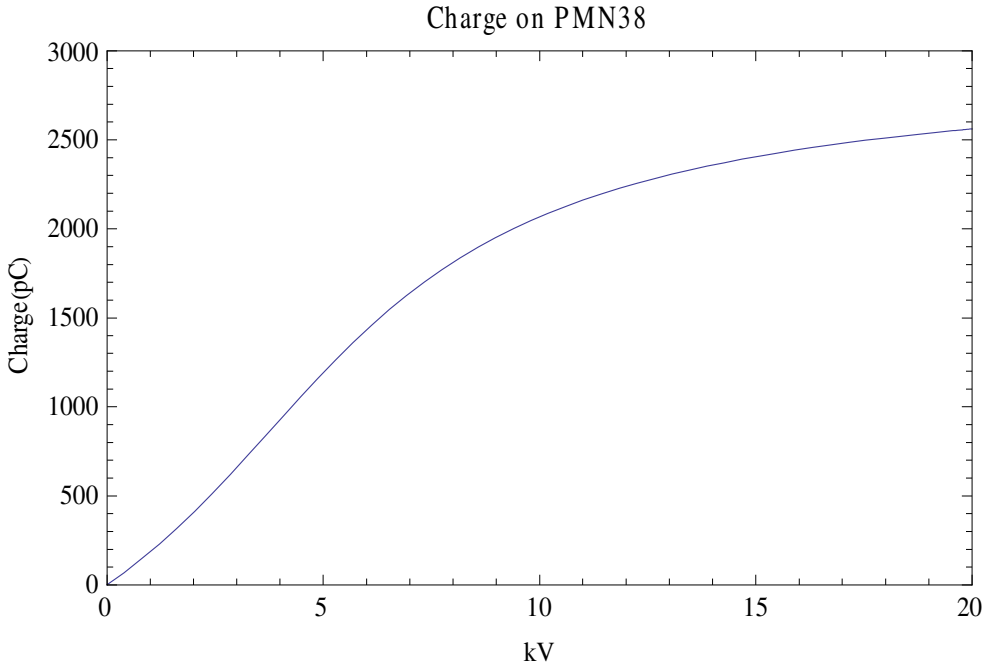

Figure 4-20. Charge on the nonlinear capacitors.

In order to verify that the LTspice simulation is using the correct model of the capacitance, a simple numerical test can be performed on a single capacitor as a pulse moves down the transmission line, as illustrated in Figure 4-21. The relationship between charge, capacitance, and voltage on a nonlinear capacitor is $C(V) = dq(V)/dV$. By finding $dq(V)$ and dV the capacitance that is occuring in LTspice can be extracted from the waveform. The current through the capacitor is $I = dq/dt$, for the finite difference LTspice code this current is $I_n = \Delta q_n/\Delta t_n$. The change in charge Δq_n at time t_n can be calculated by taking the current I_n and multiplying by the timestep $\Delta t_n = t_n - t_{n-1}$. The change in charge Δq_n can be divided by the change in voltage, $\Delta V = V_n - V_{n-1}$, to get the capacitance-voltage relationship $C(V_n) = \Delta q_n/\Delta V_n$. This relationship is plotted in Figure 4-22 for the voltage and current trace from Figure 4-21. This check of the capacitance model in LTspice assures that the LTspice model is correctly simulating the experiment.

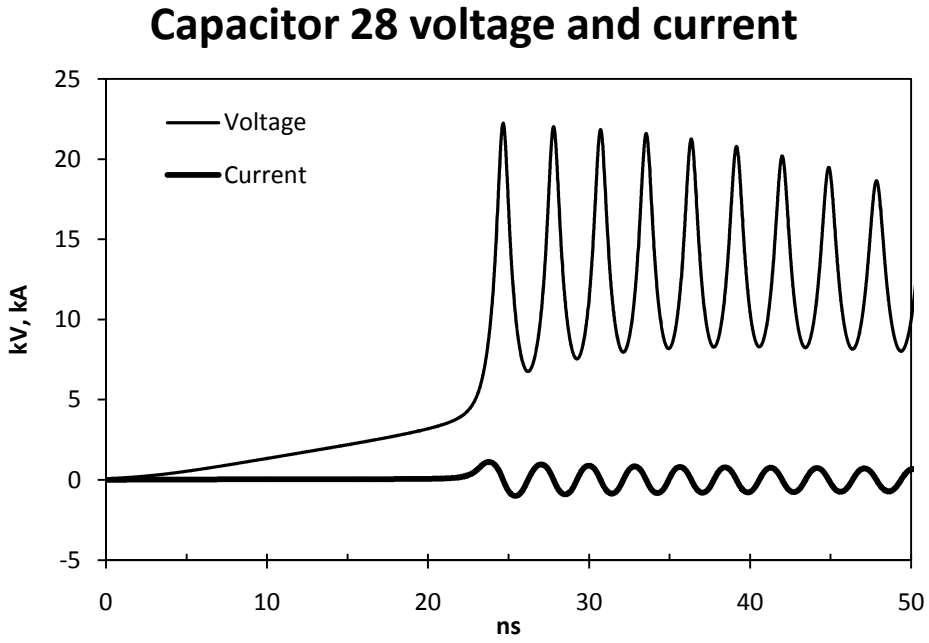

Figure 4-21. Voltage and current traces from LTspice on capacitor 28 as a pulse propagates down the line.

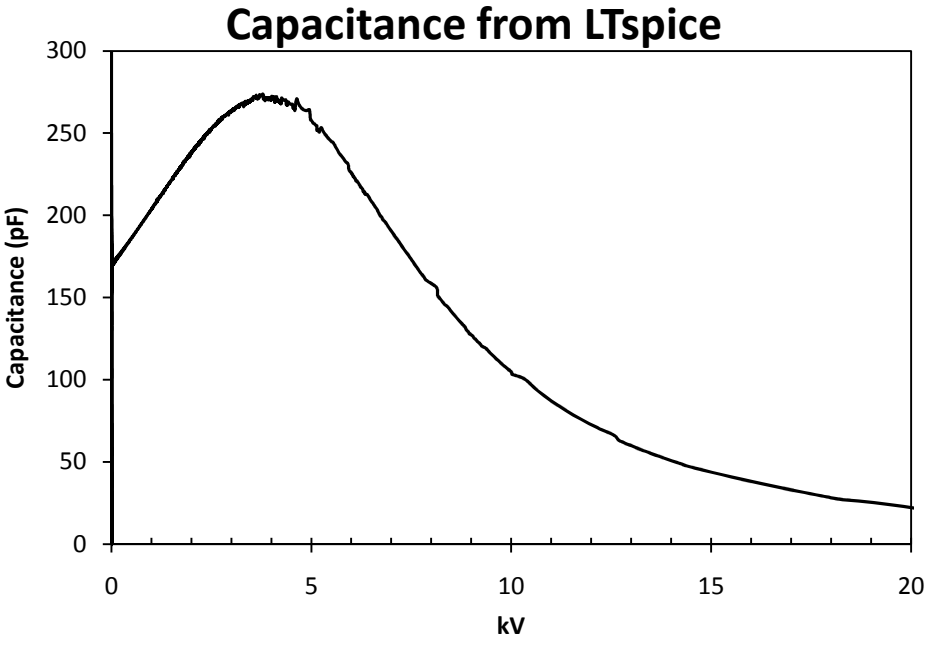

Figure 4-22. Capacitance as a function of voltage extracted from LTspice.

4.4.4 Circuit Simulations

Using the functional form of the capacitance from equation (4.1) and the analytically determined per stage inductance, the 50 stage NLTL circuit is modeled in LTspice [55]. The pulser is modeled as a 6.25 Ω source that puts out a 50 ns wide pulse with 6 ns rise and fall times. The NLTL is terminated in a 13 Ω resistance in order to match the load to the saturated line impedance. Figure 4-23 shows the simulated behavior of a lossless 50 stage NLTL circuit for different voltage of the input pulses. At input voltages below peak capacitance (~4kV), the risetime of the pulse is increased because the lower voltage portion of the pulse travels faster than the peak, effectively stretching the pulse in time and increasing the time to peak. This same process results in an electromagnetic shockwave being formed at the fall of the pulse. Following the electromagnetic shock at the end of the pulse, oscillations about zero voltage are observed. When the peak voltage of the input pulse is above the 4kV threshold, dC/dV becomes negative (cf. Figure 4-19) therefore a shock will be formed at the rise of the pulse once the voltage exceeds 4kV. The bottom pane of Figure 4-23 shows a 9kV input pulse and the resulting output pulse which shows oscillations after the rise of the pulse. The simulation results are shown for a lossless transmission line. In the actual line used in the experiment, dielectric loss will dissipate energy from the RF wave. In order to more accurately model the experiment, loss must be included in the calculations.

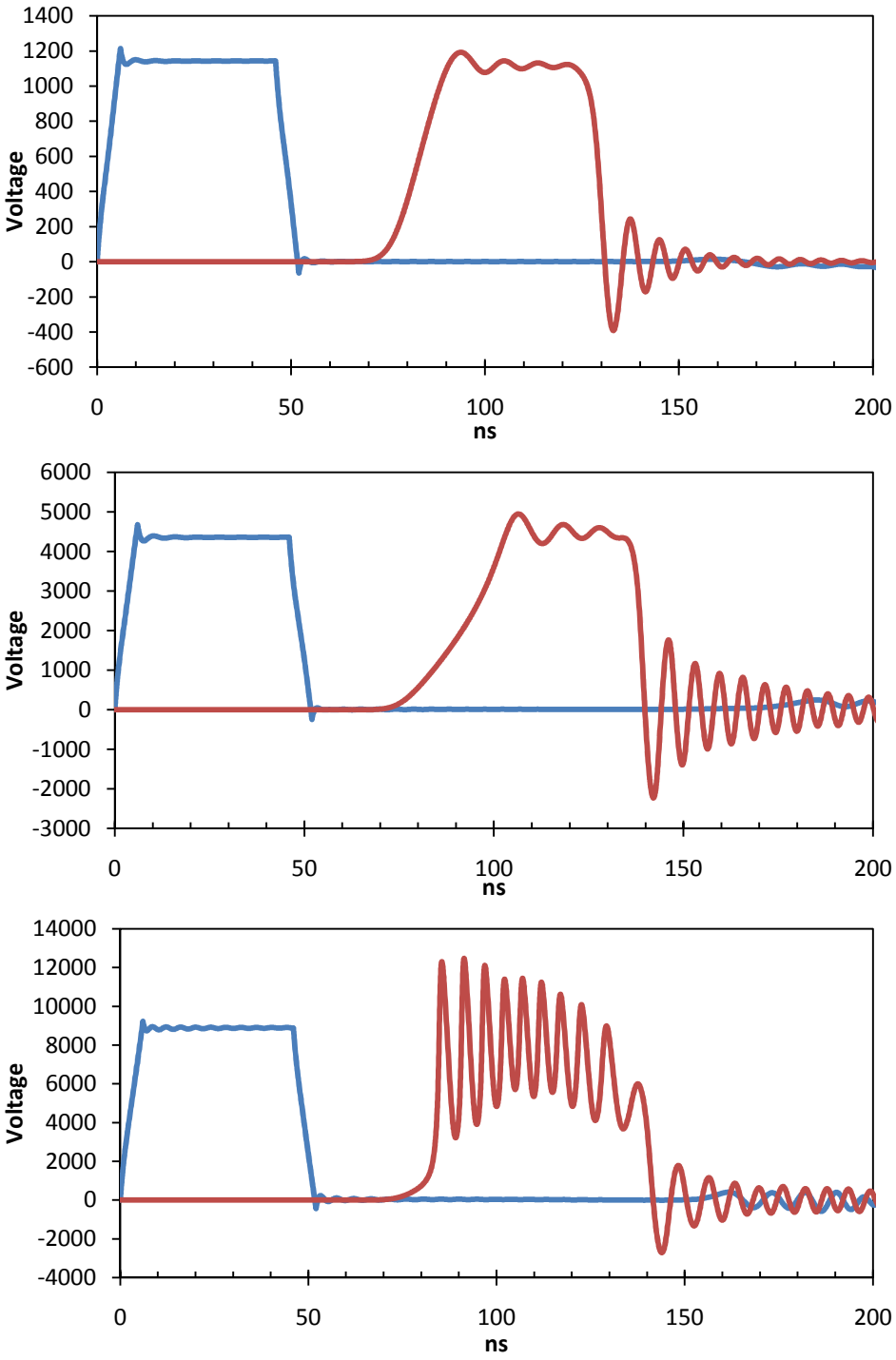

Figure 4-23. Input (blue) and output (red) traces showing the behavior of the lossless 50 stage NLTL using the PMN38 capacitance characteristic used in the experiment.

4.4.5 Loss Considerations

The loss of a capacitor is typically given as the loss tangent, tanδ. The circuit of a real capacitor is an ideal capacitor of capacitance C and an equivalent series resistance (ESR), Figure 4-24.

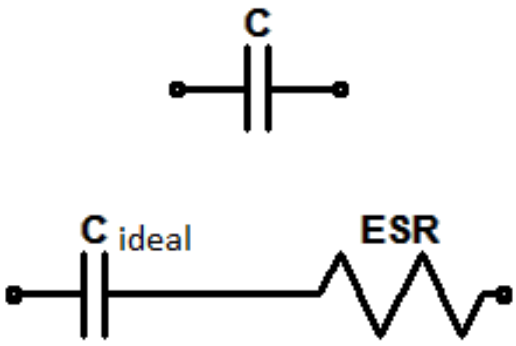

Figure 4-24. An actual capacitor can be modeled as an ideal capacitor (zero resistance) in series with a resistor.

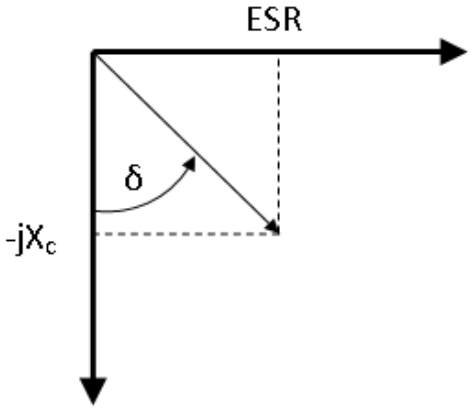

Figure 4-25. Diagram showing the real and imaginary components of the impedance and δ, the angle between them.

The impedance of a device is given by $Z(\omega) = R + jX(\omega)$, where the complex impedance is due to capacitive or inductive components. For circuits, the loss tangent is

expressed as $\tan\delta = \omega C \cdot ESR = ESR/|X_c|$, where X_c is the complex impedance of the capacitance, the ESR is the equivalent series resistance of the capacitor, and δ is the angle between the complex and real pars of the impedance. The PMN38 material loss tangent data taken at zero voltage are shown in Figure 4-26. Using the loss tangent data, the equivalent series resistance for a given frequency can be determined. This equivalent series resistance can be put into the LTspice model to take into account the loss that will be present for a specific frequency. In order to include dielectric loss effects in the circuit simulations, the ESR for a single frequency is put into the model in series with the lossless capacitors. To determine the specific ESR value to be used, a simulation is first run without resistive losses in order to determine the center frequency of oscillation. The ESR for this center frequency is then added to subsequent simulations. Although there are a very broad range of frequencies present in the NLTL waveform, this method will provide the correct damping at the dominant frequency of oscillation. Including the dielectric losses of the PNM38 in the model allows estimation of the severity of the damping experienced by the RF oscillations. In cases of excessive damping, no RF will be observable at the output of the transmission line.

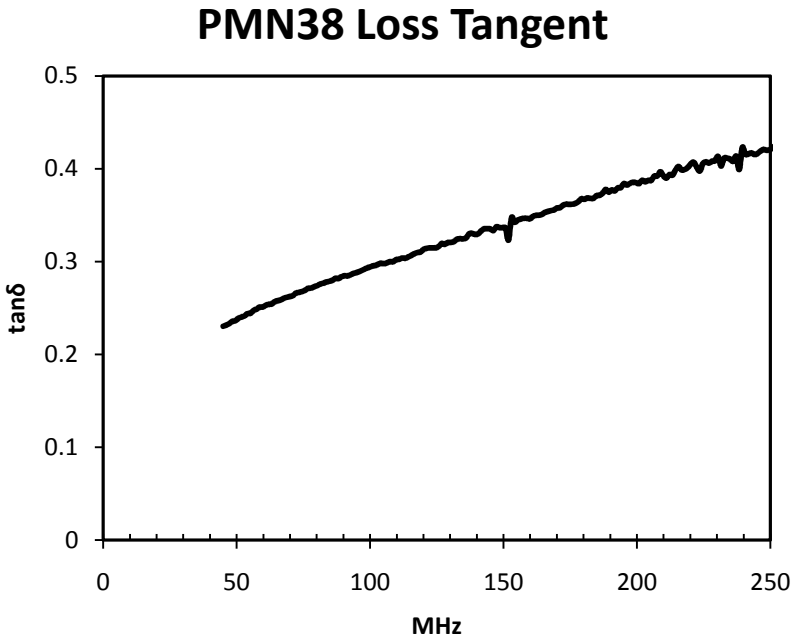

Figure 4-26. PMN38 loss tangent as a function of frequency, measured at zero voltage.

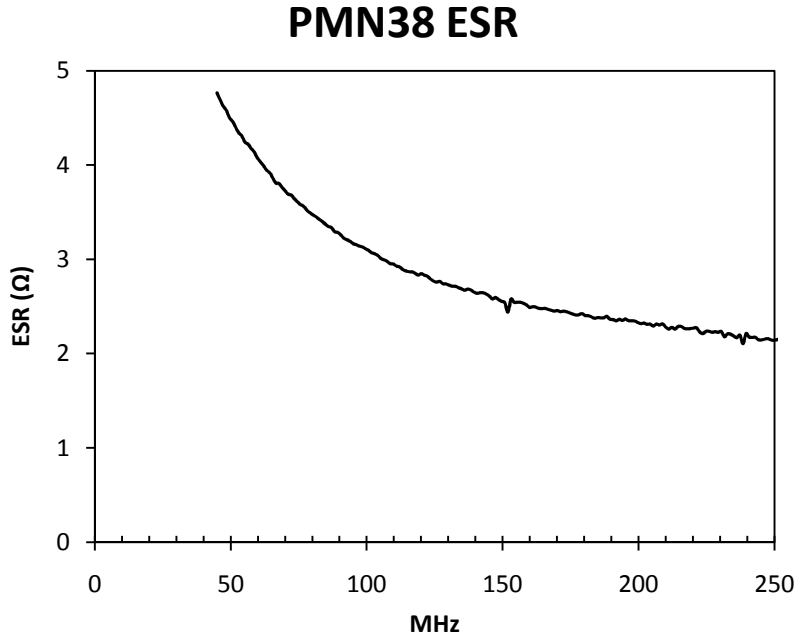

Figure 4-27. PMN38 capacitor equivalent series resistance.

The frequency dependant losses in capacitors utilizing materials like PNM38 can be detrimental to NLTL operation as higher frequency components will be damped. This will reduce both the depth and number of oscillations at the output of the NLTL, an example of this is shown in Figure 4-28.

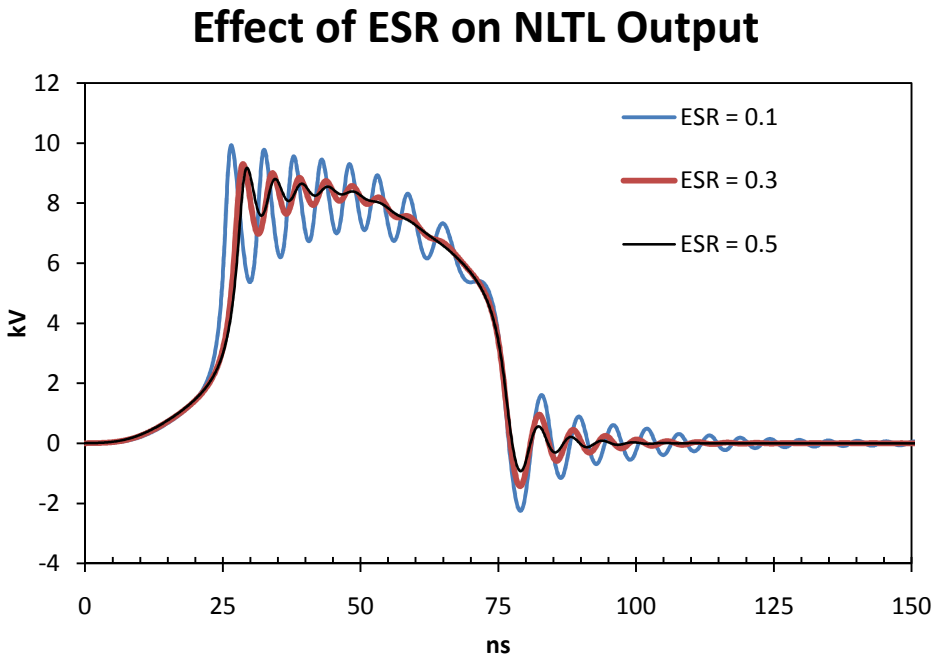

Figure 4-28. Output of 50 stage simulated NLTL with ESR of 0.1, 0.3, and 0.5 ohms.

An equivalent series resistance was added to the capacitors in the 50 stage NLTL simulations. As the ESR is increased from 0.1 Ω to 0.5 Ω the risetime is increased and the depth of oscillations is reduced. From Figure 4-27 it is clear that the ESR is at least 2 Ω for all frequencies for the PMN38 material. A circuit simulation showing the lossless and 2 Ω ESR is shown in Figure 4-29. The simulated 2 Ω NLTL waveform is approximately what is to be expected from the experimental line as the model includes the correct form of the capacitance, inductance, and a simple loss model.

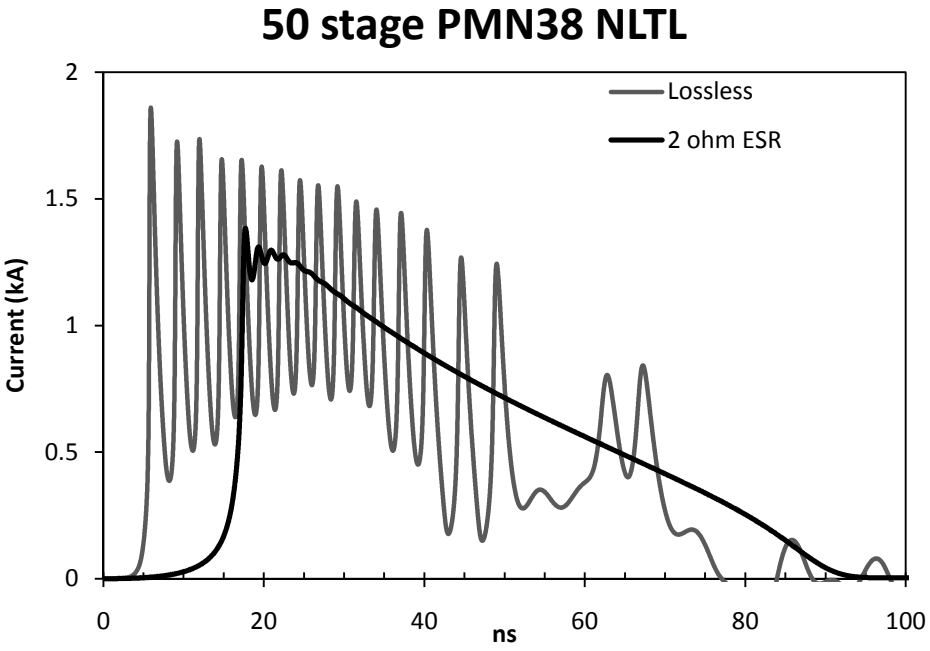

Figure 4-29. Output of 50 stage NLTL showing lossless case and 2Ω ESR case.

4.4.6 Experimental Diagnostics

The diagnostics used on the experimental system are Bdot sensors along the line and a commercial 1.2 GHz bandwidth current viewing resistor (CVR) at the load. The CVR is a low resistance (15 mΩ) resistor with negligible inductance that allows the measurement of the current flowing through the output of the NLTL by monitoring the output voltage, $I = V/R$. The CVR was placed at the end of the line in series with a low inductance, ≈ 30 nH, 17 Ω coaxial load. The CVR was used as a reference in order to calibrate the Bdot probes in the transmission line prior to installing the capacitors as well as providing the exit current at the termination of the NLTL. Four sets of Bdot probes were spaced along the NLTL. Each Bdot set was comprised of 4 probes inserted in adjacent stages for a total of 16 Bdots. The first Bdot group was at stages 0-3, the second group was in stages 10-13, the third group was in stages 25-28, and the forth group was in stages 40-43. The entrance current was measured

with Bdot zero and the exit current is measured with the CVR. The final set of Bdots were put at stages 40-43 instead of at the end of the line, stage 47-50, to avoid the complicated waveforms that would result from reflections at the end of the line. The large number of adjacent Bdot probes allows determination of the phase shift per stage, in the case of an RF waveform, and to measure the velocity of the pulse as it propagates down the transmission line. The diagnostics are visible in Figure 4-30 and Figure 4-31.

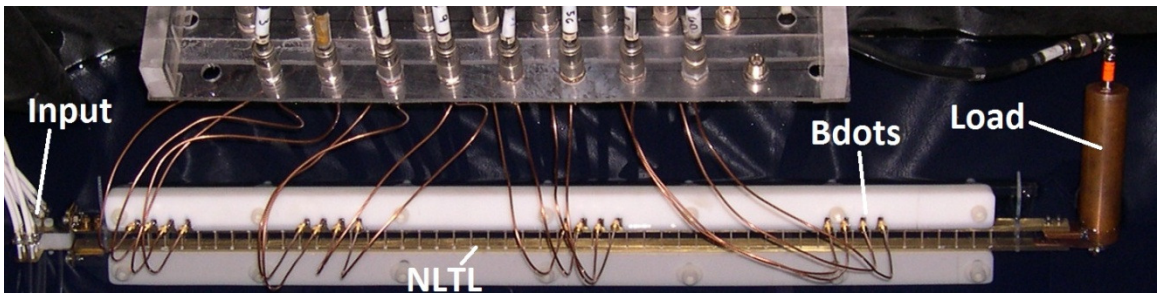

Figure 4-30. NLTL with diagnostics and load indicated.

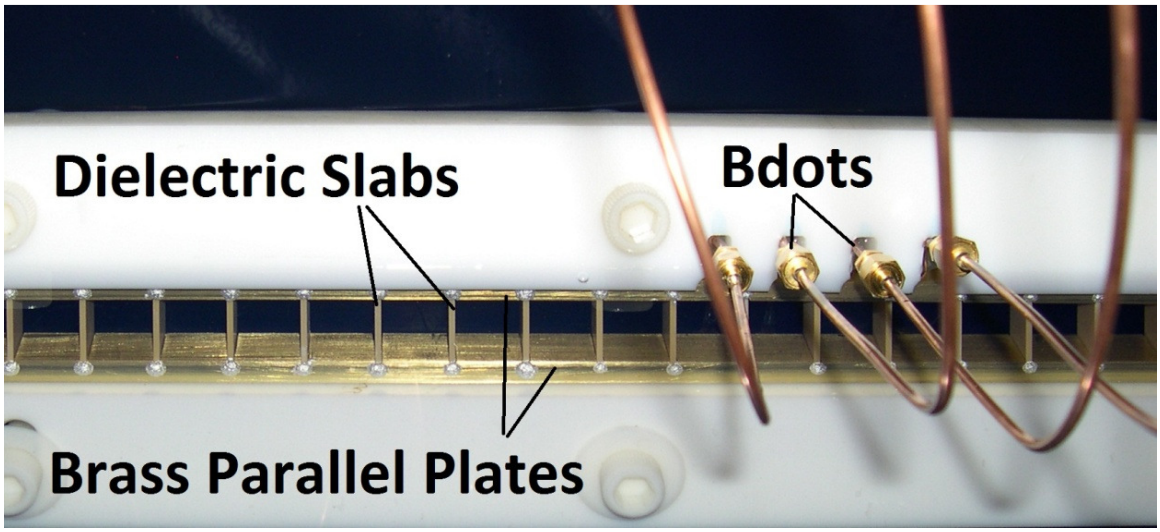

Figure 4-31. Closeup of experimental NLTL

The calibration of the Bdot probes was performed by pulsing at low voltage, < 10 kV. The Bdot probe traces are then integrated and calibrated with the reference current from the commercial CVR. The calibrations were performed with 10 dB attenuators and external 50 Ω terminators on the Bdots. The measured sensitivities (with the attenuators installed) are listed in Table 4-3. Bdot #4 and Bdot #6 were found to have no output so these probes were not used. An attempt to repair the two malfunctioning probes was not attempted because the repair effort might have damaged the other working probes. The overlay of the Bdots with the CVR traces are shown in Figure 4-32. The integrated Bdot signals match the CVR very well on the current rise to peak and then deviate somewhat. Since the signal of interest is close to the rise of the pulse these deviations can be ignored as the late in time data is not used. Some of the mismatch between traces in the calibration plots (Figure 4-32) is due to imperfect time delays which were corrected for the actual experiment. The determination of the exact delays for each diagnostic was performed with a time domain reflectometry (TDR) measurement and these delays were put into an analysis program to correctly offset each trace in time.

Table 4-3. Bdot calibrations

Bdot	A/(V*s)	Bdot	A/(V*s)
B1	4.814E+10	B9	5.320E+10
B2	4.389E+10	B10	5.534E+10
B3	4.566E+10	B11	4.868E+10
B4		B12	2.322E+10
B5	6.663E+10	B13	6.230E+10
B6		B14	7.625E+10
B7	4.644E+10	B15	5.607E+10
B8	5.053E+10	B16	3.790E+10

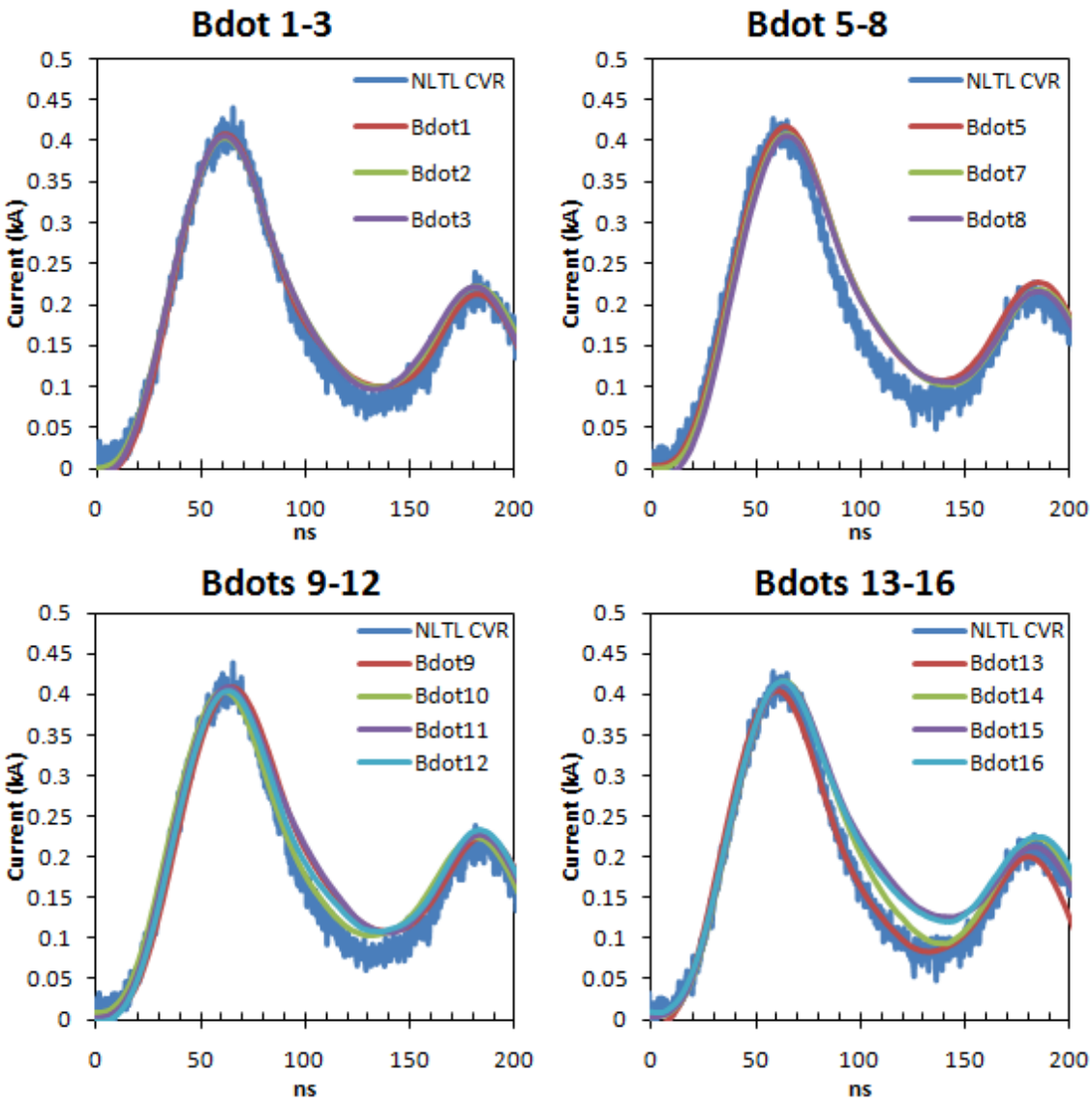

Figure 4-32. Integrated Bdot calibration traces.

4.4.7 Experimental Data

The experiment was run with pulser output voltages ranging from 4-43 kV. At voltages below 4 kV, the line should not sharpen the waveform since dC/dV is positive, Figure 4-19. Figure 4-33 shows the 4 kV pulse at the beginning and end of the line showing

virtually no change in pulse shape, but rather the current has decreased from ~230 A to ~125 A at the last set of Bdots.

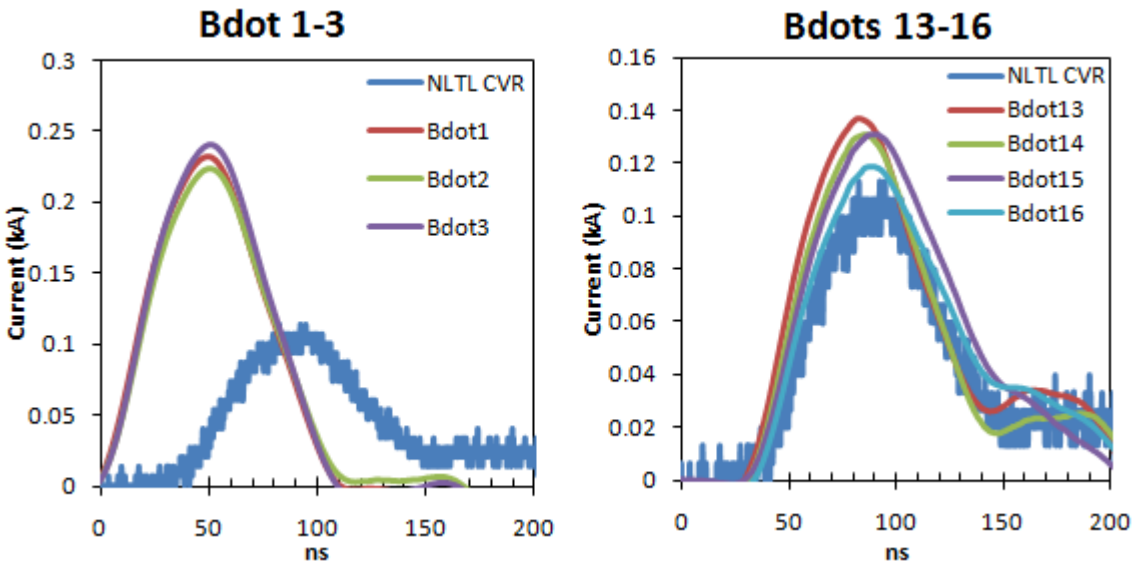

Figure 4-33. Integrated Bdots 1-3 and 13-16 with NLTL CVR showing the output current with 4 kV input.

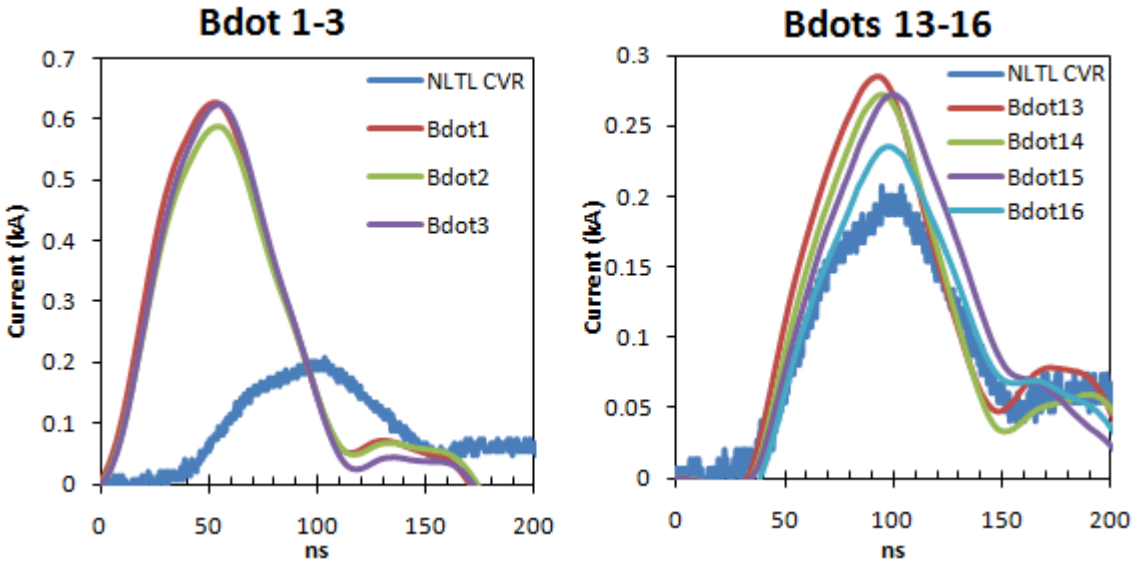

Figure 4-34. Integrated Bdots 1-3 and 13-16 with NLTL CVR showing the output current with 10 kV input.

When the voltage is increased to 10 kV, Figure 4-34, there is no significant change in the pulse at it moves down the line. The current decreases from ~600 A to ~260 A from the first to the last set of Bdots.

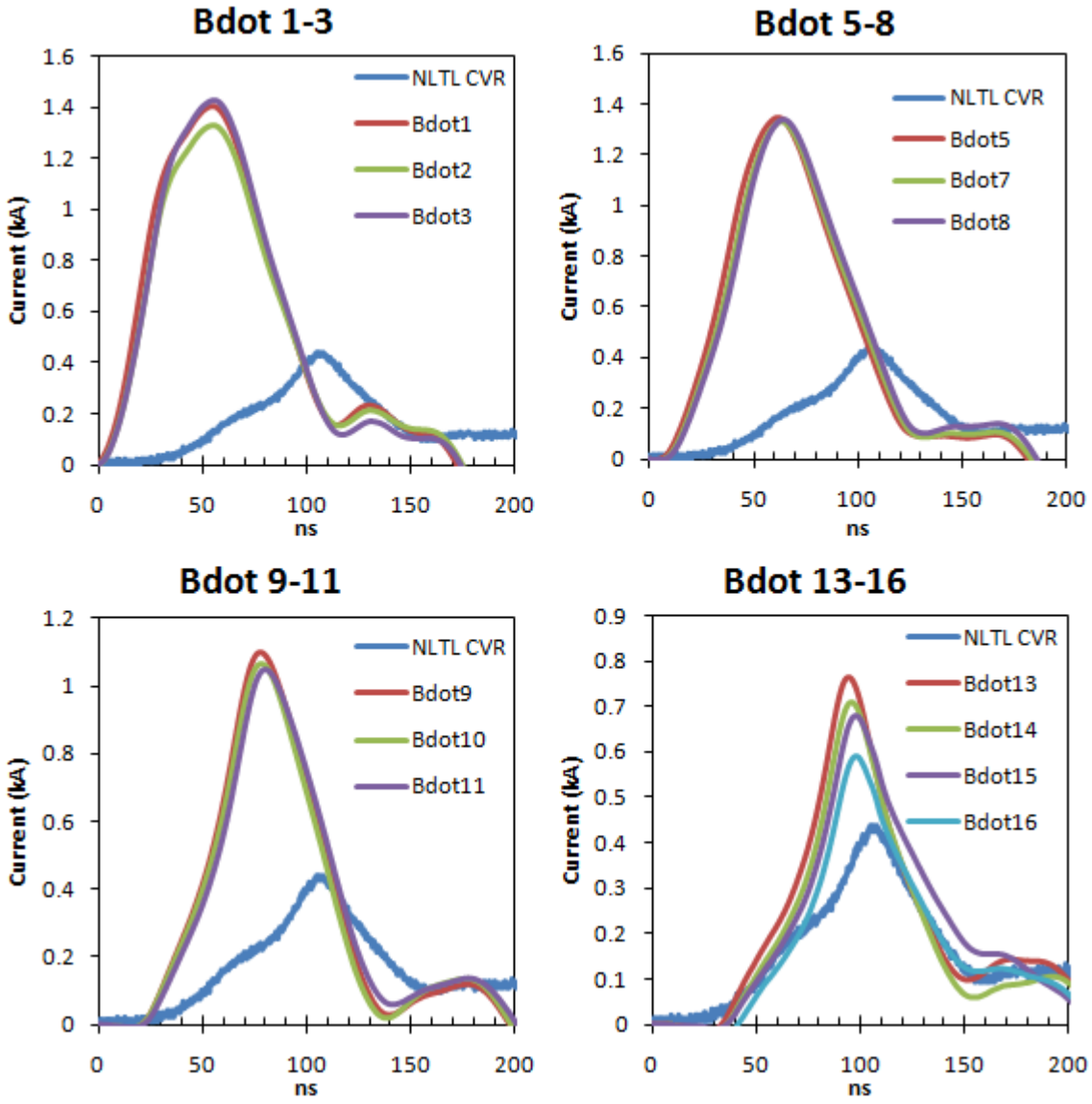

Figure 4-35. Integrated Bdots showing the evolution of a 25 kV input pulse.

As the voltage is further increased to 25 kV the nonlinear nature of the line becomes more evident as the pulse shape changes down the line, Figure 4-35. The current decreases

from ~1400 A to ~750 A from the first to the last set of Bdots. The highest output voltage that was achievable with the available charging system and switch pressure regulator was 43 kV, a 41 kV shot is shown in Figure 4-36.

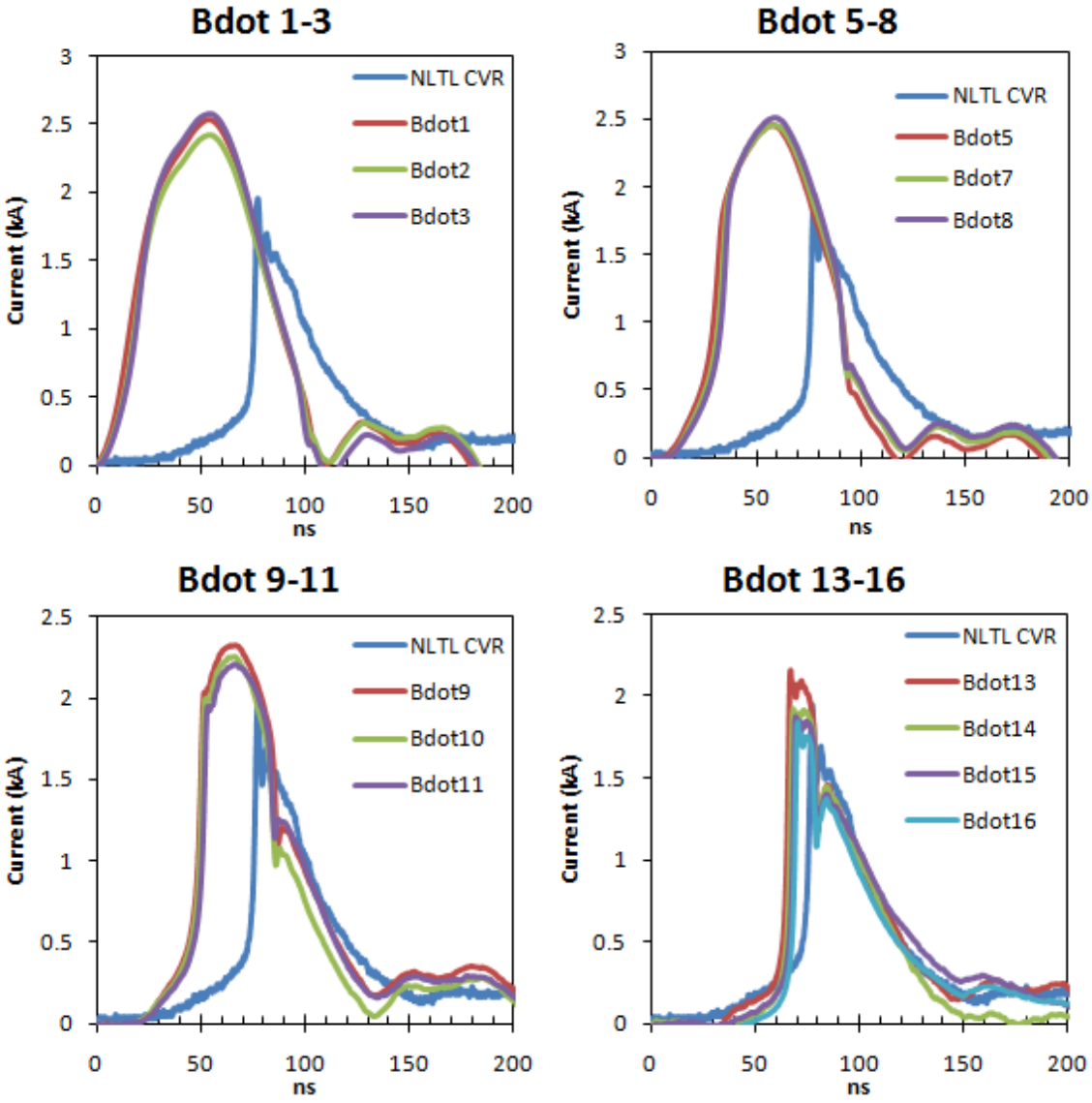

Figure 4-36. Integrated Bdot traces showing the evolution of a 41 kV input pulse

It is very clear that above ~ 0.5 kA a strong electromagnetic shock is formed with a risetime of approximately 3ns. Due to the high loss present in the PMN38 dielectric material strong oscillations were never formed as the shockwave propagated down the NLTL. There

is some evidence of oscillations after the peak on the traces from Bdots 13-16, however the depth of these oscillations was very small. This behavior was expected based on the simulation shown in Figure 4-29 where the shockwave forms, however, with a 2 Ω ESR the oscillation do not develop. The experimental results have the same general trend as the traces from Figure 4-28 where the risetime is slow until the voltage reaches ~ 4 kV. After this point dC/dV is negative and an electromagnetic shockwave is generated. Figure 4-37 shows the evolution of the 41 kV pulse as it travels down the line.

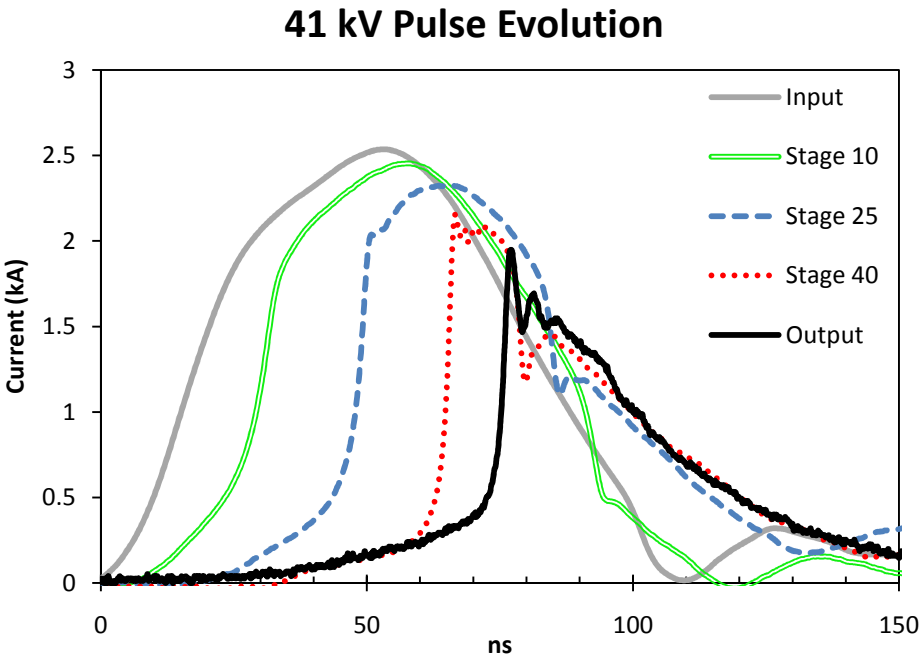

Figure 4-37. Traces showing the evolution of a 41 kV input pulse.

The velocity of the pulse traveling down the transmission line can be easily measured using the traces in Figure 4-36. By measuring the time between adjacent sets of Bdots reaching a current of 1.5 kA, 16.5 ± 0.5 ns, which are separated by 25.15 cm, the velocity is calculated to be 0.051 ± 0.002 c. Since the velocity of a signal on the transmission line is given by $v = (\mathrm{LC})^{-1/2}$, where the L and C are per unit length, it is possible to

determine the capacitance at a specified current. For the 1.5kA current with the velocity determined above and the 13 nH/1.676 cm inductance of the NLTL this analysis gives a capacitance per stage of 92 ± 7 pF. Comparing this to the 4 kV case shown in Figure 4-33, which for the 0.1kA velocity is 0.035 ± 0.002 c has a capacitance of 196 ± 22 pF. This low voltage capacitance value is what is expected based on the functional form of the capacitance shown in Figure 4-19, however, it is expected that the capacitance for the 41 kV input pulse would be ~ 20 pF based on Figure 4-19. This discrepancy is likely due to the high loss and poor high frequency response of the dielectric material. The capacitance values can be used to determine the impedance at low and high voltages, $Z = (L/C)^{1/2}$. The impedances are 8.1 Ω and 11.9 Ω for the 4 kV and 41 kV input pulses respectively. This analysis technique may be useful as a voltage diagnostic in certain cases where the frequency and voltage dependence of a nonlinear dielectric is well known, or, as a method to characterize the frequency and voltage dependence of a material.

4.4.8 Conclusions

A nonlinear dielectric-based nonlinear transmission line was constructed and tested. The NLTL was modeled in a circuit simulation code using the experimentally measured form of the nonlinear capacitance. Dielectric loss was modeled by finding the equivalent series resistance of the dielectric from the measured loss tangent at the expected dominant frequency of oscillation. The inclusion of loss in the model damps the RF oscillations at the peak of the wave after the electromagnetic shockfront. The experimental line was tested at voltages from 4-43 kV and showed the expected nonlinear behavior as waveforms showed

shockwave generation as they travel down the transmission line. The waveforms from the experimental line compare qualitatively with the circuit model. An analysis of the velocity of the waveform on the transmission line can be used to probe the transmission line impedance and the nonlinear dependence of the dielectric material.

CHAPTER 5

CONDUCTIVE VERSUS CAPACITIVE COUPLING FOR CELL ELECTROPORATION WITH NANOSECOND PULSES

This chapter summarizes the authors earlier work on bioelectromagnetism; specifically, on the application of a high voltage nanosecond pulse to biological cells [58].

5.1 Introduction

Electroporation is the formation of pores in cell walls due to the application of an electric field [59]. The process is reversible and the pores will close after some time, typically 100s of seconds [60]. In typical a cell electroporation experiment and electrical pulse is applied across a sample of cells. The pulses used have electric field amplitude sufficient to produce a voltage drop on the order of 1 V across a cell and are of μs to ms in duration. Electroporation has been used as a research tool for the last 30 years as a technique for transfection, where nucleic acids are introduced into cells [61]. For the last 20 years there has been work on live animals or humans in clinical applications where it has been used as a means to increase the uptake of drugs into cells to increase the efficacy of chemotherapy [62]. Research into the use of electroporation as a method of gene delivery into cells, which is usually accomplished by a viral gene delivery, is ongoing and could provide an alternative method for gene therapy, dubbed electrogene therapy [63].

Cell electroporation with fields coupled capacitively or radiatively would be a powerful technique for both transfection research or for electrochemotheraputic clinical treatment. In this section the results of experiments and simulations performed to determine the effects of using capacitive coupling for the electroporation of cells are presented. The focus of this experiment is on reversible cell electroporation although apoptosis, programmed cell death, is seen in treated cells.

The experiment is performed with a fast risetime pulser and antenna (tapered plate transmission line) to expose samples of cells to electric fields. A diagram of the experimental system is shown in Figure 5-1. The pulser is connected to a peaking/tailcut switch, which shortens and decreases the risetime of the pulses. To avoid breakdown, the antenna is housed in an SF_6 filled plastic box. The pulser system is capable of delivering pulses of 33 kV with subnanosecond risetimes to the antenna. The pulse parameters used in these experiments are a peak voltage of 24 kV, 0.6 ns risetime, and 1.6 ns FWHM; a typical pulse in shown in Figure 5-2. Pulses are measured using a calibrated probe in the antenna shown in Figure 5-3.

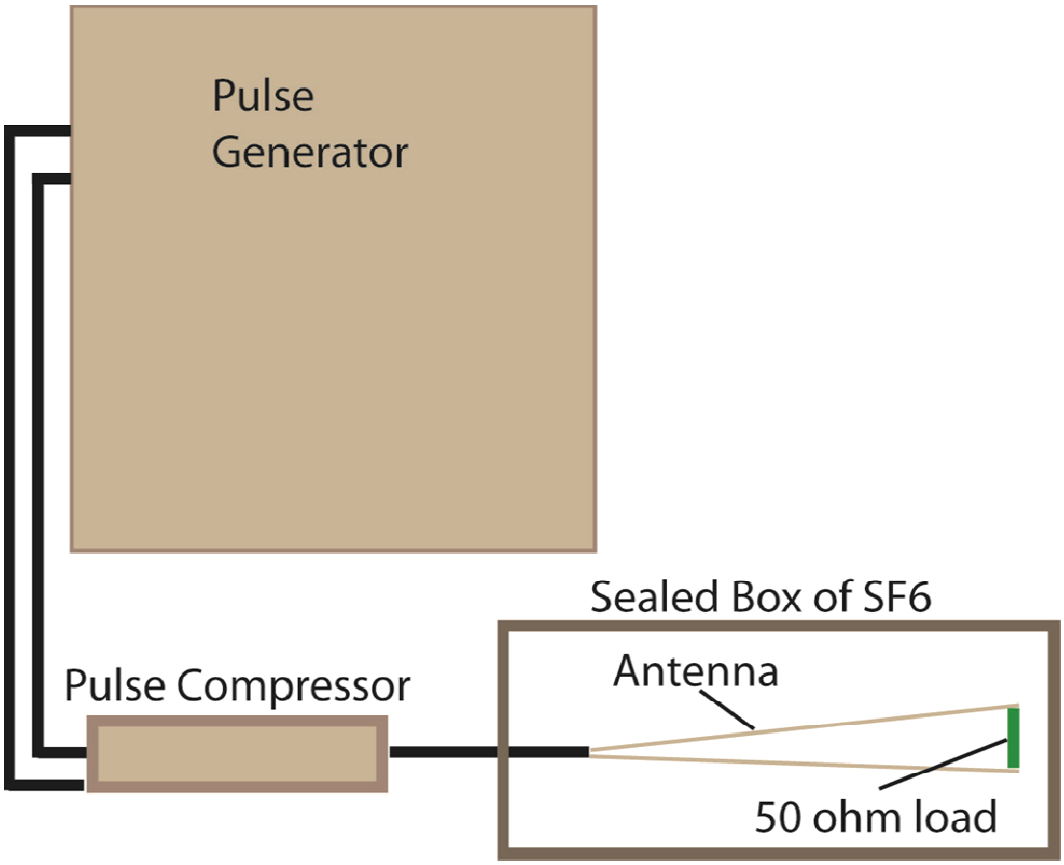

Figure 5-1: Experiments are performed on the antenna in a sealed box filled with SF_6 to prevent arcing.

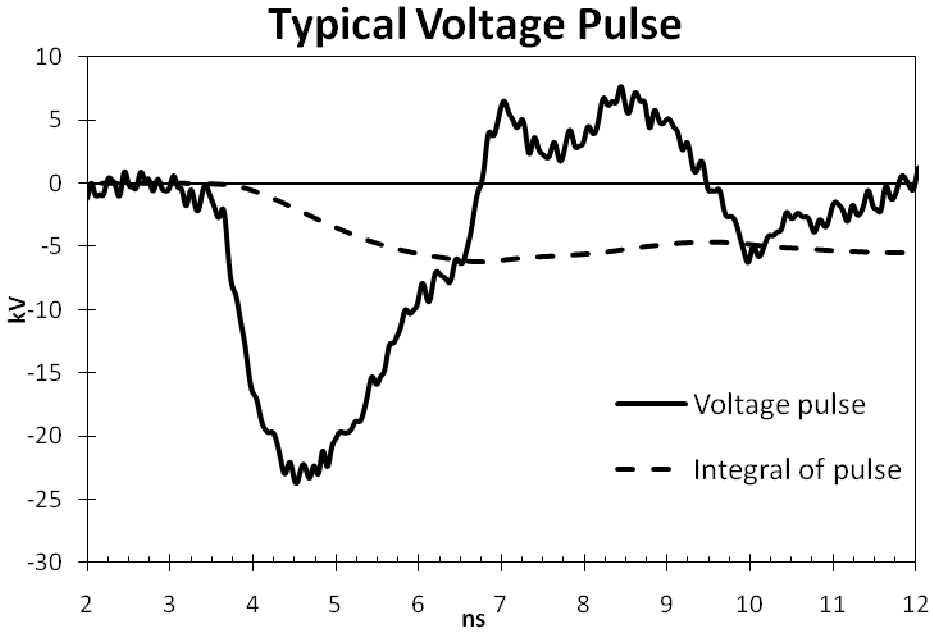

Figure 5-2. Output from pulse compressor to antenna.

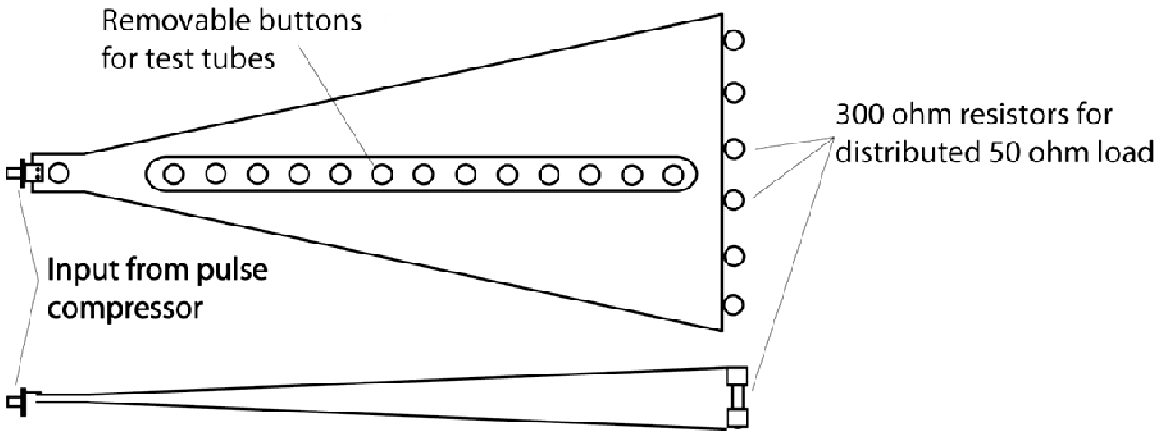

Figure 5-3. Antenna where the cells are placed as either part of the load with wire electrodes (conductive connection), or through the holes in the plates (capacitive coupling).

The cells were exposed to the fields by either a conducting connection (wire electrodes) or by means of capacitive coupling (tube inserted through holes in transmission line), the two configurations are shown in Figure 5-4.

Figure 5-4. Diagram showing the two possible test tube locations for electroporation. Note that only a single tube, either conductive (right test tube) or capacitve connection (left test tube), would be present during a given shot.

The regime being explored here has not been previously published on prior to our study [58], although others have looked at different bioeffects with pulses of similar duration and electric field [64]. There have been many studies of the effects of 10s of ns

duration pulses with few ns risetimes [65-73] and of subnanosecond pulses at very high electric fields of up to 1MV/m [73].

5.2 Circuit Model

A simple circuit model of the experiment is used to describe the capacitive coupling of the pulse to the cell suspension. The cell suspension in the test tube has contributions from resistive and capacitive impedance. The resistance and capacitance of the cell suspension are in parallel and the coupling capacitance from the upper and lower plates of the transmission line to the test tubes are in series with the cell suspension. The circuit diagram of this system is shown in Figure 5-5, where the top and bottom capacitance represents the test tube wall between the conductive transmission line and the conductive cell suspension.

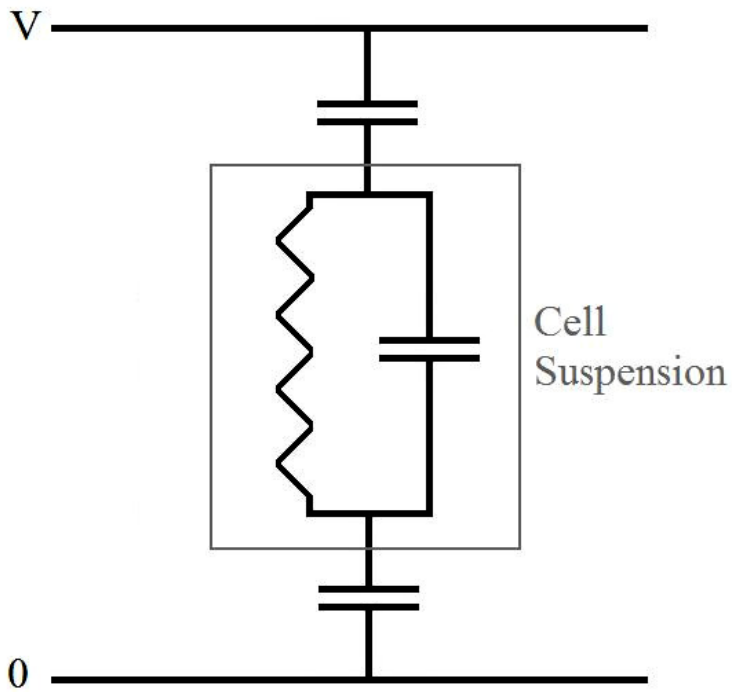

Figure 5-5. Circuit of cell suspension test tube inserted into transmission line in a capacitively coupled configuration, the top and bottom capacitance represent the test tube wall.

5.3 Simulations

Simulations were performed in MAGIC 3D. The simulation geometry is a parallel plate transmission line with the test tube containing the cell suspension with either conductive connection to the plates, or inserted through a hole in the transmission line plates for capacitive coupling; the latter is shown in Figure 5-6. In the case of conductive connection, the voltage across the cell suspension is approximately that of the applied pulse, with a small component that is proportional to the derivative of the voltage pulse due to the small capacitance across the cell suspension. The voltage across the cell suspension in the capacitively coupled case is very different. The current that is driven through the cell suspension (Figure 5-5) must be coupled by displacement current through the test tube

wall. The voltage across the cell suspension will therefore be proportional to the derivative of the transmission line voltage. This leads to a different pulse shape in the case of capacitive coupling.

The output of the MAGIC simulations for the case of capacitive coupling is shown in Figure 5-7. The voltage across the tube, measured across the anode-cathode gap within the suspension, is approximately 8 kV for a transmission line voltage of 24 kV. Therefore 8 kV is dropped across the cell suspension and the remaining 16 kV is dropped across the capacitive connections from transmission line to cell suspension seen in Figure 5-5. The electric field of 16 kV/cm was used to set the electrode spacing in the conductive connection case in order to match the electric field amplitudes in each case.

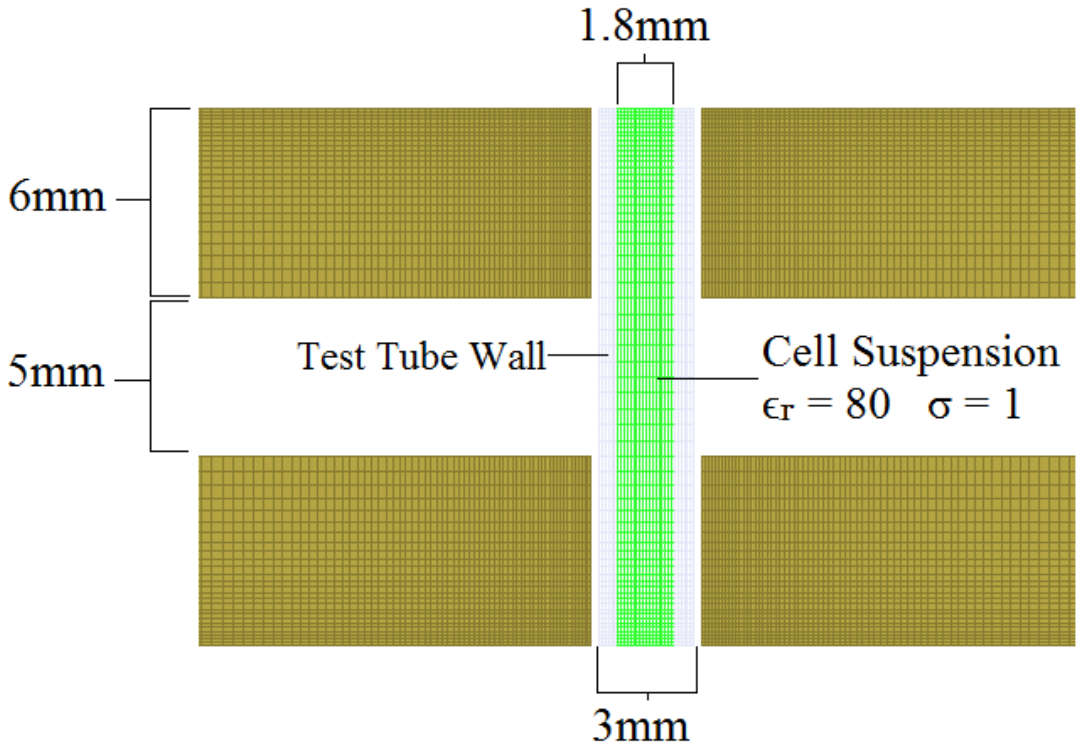

Figure 5-6. MAGIC model for capacitive coupling.

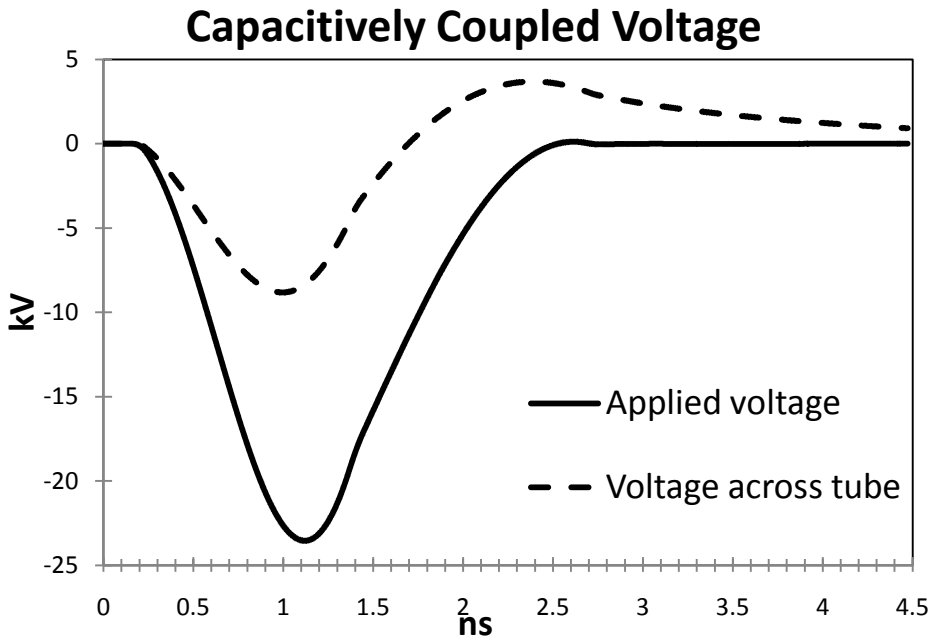

Figure 5-7. MAGIC simulation results of capacitively coupled tube. The dashed line represents the voltage measured across the 5mm gap, within the cell suspension, between the plates seen in Figure 5-6. Since the voltage measured across the tube is driven by the displacement current and therefore the derivative of the applied voltage, the minimum in the voltage across the tube occurs during the rise of the applied pulse.

5.4 Cell Culture and Imaging

Human Jurkat T cells, which are an immortalized line of T lymphocyte cells commonly used in research, were grown in RPMI 1640 media (InVitrogen) supplemented with penicillin, streptomycin, and 10% fetal calf serum. For treatment, cells in culture media were mixed in the absence or presence of Bleomycin, a cancer chemotherapeutic drug which has been used previously in experiments to determine electrochemotherapeutic effects on Jurkat cells [74], (5 ng/ml) and agarose (1/10 volume of 4% agarose in phosphate-buffered saline). The agarose solution was added to the glass tubes and allowed to gel at room temperature for 10 minutes (see next paragraph). Following treatment, the gel cylinders containing the cells were extruded using positive air pressure and incubated in

culture media containing 5 ng/ml DAPI (4',6-diamidino-2-phenylindole), a fluorescent stain. Cells were imaged 2 hours after treatment to determine immediate killing and 24 hours after treatment to determine death due to the Bleomycin.

5.5 Experimental Results

To minimize the movement of the cells within the glass tubes the Jurkat cells were embedded in an agarose solution which was allowed to gel at room temperature. The immobilization of the cells allows the cell killing to be spatially resolved. The cells remained viable by both trypan blue staining assays, used to selectively stain dead cells blue, and growth assays when cultured within the gel matrix. The cells within the glass tubes were subjected to pulses with either conductive connection or with capacitive coupling in either the presence or absence of Bleomycin. Following treatment, cells were stained by culturing in growth medium containing DAPI. DAPI does not stain cells with an intact cellular membrane, but if membrane integrity is compromised cell nuclei will be stained. Each of the agarose tube gels containing Jurkat cells was stained and counted (Figure 5-8) for dead (DAPI positive) and live (DAPI negative) cells.

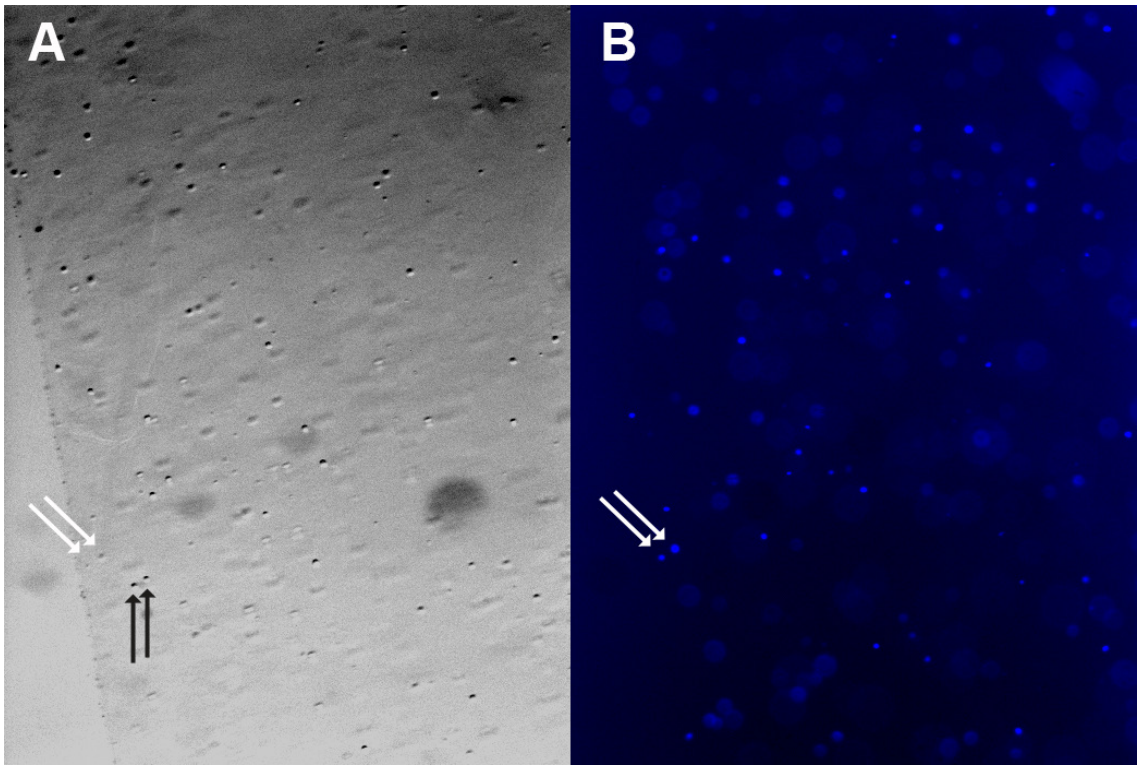

Figure 5-8. DAPI Staining of Jurkat Cells Immobilized in Agarose. Panel (A) shows a bright field image of an agarose gel containing immobilized Jurkat cells. The edge of the gel is evident along the lower left image of the gel. Two dead cells that are stained with DAPI are indicated with white arrows and two live cells that are not stained with DAPI are indicated with black arrows. Panel (B) shows the corresponding fluorescence image, the fluorescent cells have been killed, the two dead cells indicated in panel A are also indicated with white arrows in panel B.

Cells received 0, 1, 4 or 8 pulses under each of these conditions and then cell survival was quantitated as described in Figure 5-8 for cell survival. Three replicate tube gels were quantitated for each experimental point for statistics. At two hours following treatment (Figure 5-9) a significant difference in cell survival was seen for those cells that were pulsed with conductive connection. After 8 pulses, the cells pulsed with conductive connection were reduced to less than 40 % of their starting population. Cells in the capacitively coupled case were not significantly reduced in number when assayed 2 hours after treatment.

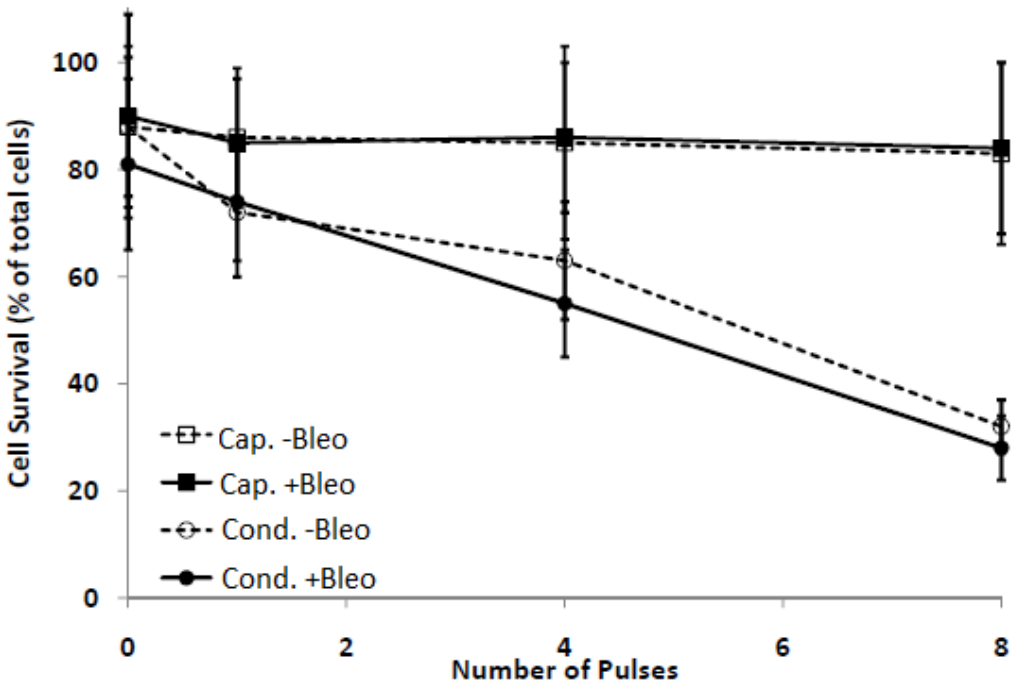

Figure 5-9. Cell survival at 2 hours following electroporation. Jurkat cells were pulsed in the absence (-Bleo) or presence (+Bleo) of Bleomycin with either capacitive coupling (Cap.) or conductive coupling (Cond.) for the indicated number of pulses. Two hours after treatment, cells were incubated in the presence of DAPI and cell survival determined.

To measure the electrochemotherapeutic effect of treatments, cells were incubated in the agarose tubes for 24 hours and then imaged for DAPI staining. We have shown previously that Bleomycin entering the cells following electroporation killed a majority of the Jurkat cells within 24 hrs. As shown in Figure 5-10, the cells pulsed with conductive connection showed significantly lower survival after 24 hours compared to that seen at 2 hours (Figure 5-9). In the presence of Bleomycin and conductive coupling, cell survival is reduced to 10% after 4 pulses. In the absence of Bleomycin, cell survival was 32%. The difference between these two survival rates is consistent with electroporation leading to enhanced Bleomycin uptake and increased cell death over the 24 hour period. Similar

results have been reported previously for Jurkat cells maintained in solution [74]. No electrochemotherapeutic effect was observed for the cells that experienced capacitive coupling.

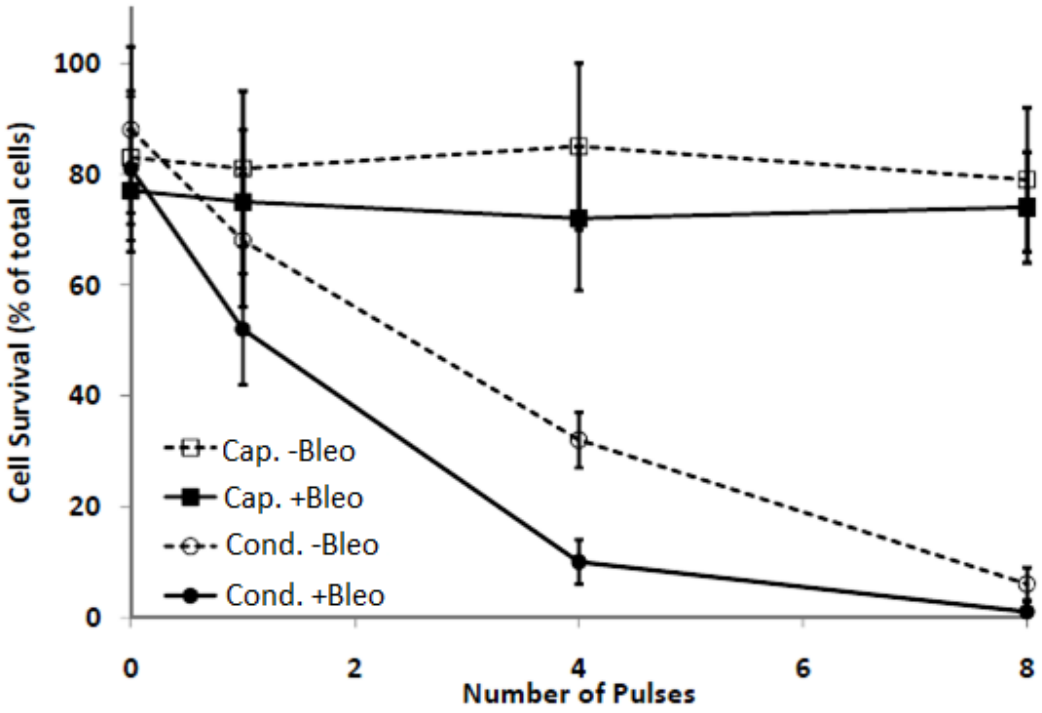

Figure 5-10. Cell survival at 24 hours following electroporation.

5.6 Discussion

The difference between these two cases is immediately obvious. The magnitude of the electric field was 16 kV/cm in both cases, however, in the case of conductive connection a cell in the center of the tube will see an electric field in one direction only, whereas a cell in the center of the tube in the capacitive coupling case will see an electric field that reverses direction. The bipolar pulse that a cell is subject to in the capacitive coupled case provides no net charging of the cell membrane and hence no perforation of the cell membrane, which

is necessary for Bleomycin to enter. Bipolar pulses occurring faster than the timescale of pore formation that result from capacitive coupling to the cell suspension therefore inhibit electroporation. The cell in the conductively connected case is different in that it is left with a net polarization after the pulse is applied; see the integral of the voltage pulse shown in Figure 5-2. The importance of this result is that experiments done using a conductive connection to determine dose, field strength, pulse duration, or other parameters cannot necessarily be assumed to behave the same way when using a field that is coupled capacitively or broadcast with an antenna. The pulse shape is important when working with pulses that have durations on or faster than the timescale of bioeffects. These results suggest that electroporation using capacitive connection may require a step function pulse shape, which will be differentiated into a monopolar pulse when coupled to the sample, as opposed to the impulse which is differentiated into a bipolar pulse. Step function pulse shapes are accessible in transmission line experiments such as those performed here, but may not be as accessible for pulses radiated from an antenna.

CHAPTER 6

CONCLUSIONS AND FUTURE WORK

The research presented here details some novel configurations for the generation of high power microwaves. Included is the new RPM magnetron configuration, simulation based studies of beam dynamics for general crossed-field systems, solid state sources based on nonlinear transmission lines, and work on bioelectromagetism during the early phase of this thesis research.

A new type of magnetron device, the recirculating planar magnetron (RPM), has been developed. RPM simulations have been performed to determine the feasibility of the device in both conventional and inverted configurations with MELBA type parameters. The 2D proof-of-concept simulations of the RPMs show startup and operation, and in the inverted magnetron design, show rapid startup due to the negative mass instability. 3D geometries of the inverted RPMs with the University of Michigan MELBA machine parameters show that axial extraction is possible. Radial B-field simulations were done by Dr. Brad Hoff of the Air Force Research Laboratory showing the feasibility of this configuration. Future work on the RPM project should begin by experimentally testing the conventional configuration on MELBA. Experimental confirmation of the recirculation of electrons and microwaves will give confidence that simulation can be used further as a

design tool for the RPM. Axial extraction from the inverted design will be a challenge; however, several different possible configurations for axial extraction were presented here. Comparison of the conventional and inverted designs on the same driver will be interesting as this could give confirmation and quantitative data on the faster startup of the inverted geometry.

An electron rotating under a general combination of an axial magnetic field and a radial electric field may exhibit negative, positive, and infinite effective mass behavior [1],[28]. Particle-in-cell simulations to analyze the stability of a rotating annular electron beam in a coaxial waveguide for general radial electric and axial magnetic fields were performed. For the cases where the effective electron mass is positive, a beam seeded with an initial density perturbation will undergo electrostatic oscillations in the beam frame. For negative effective mass, azimuthal bunching of the beam about the regions of peak density will reinforce the initial azimuthal electric field perturbation. Electrons display infinite mass behavior at some specific combination of radial electric field and axial magnetic field where an initial density perturbation will persist. A condition for the infinite mass case is that the electric field contribution from space charge within the beam is negligible compared to the applied electric field. In this last case, even the resistive wall instability [1] is absent [47]. Future work should seek to extend the analysis to an equilibrium Brillouin flow. The presence of space charge will require the consideration of the entire mode structure in addition to treatment of the position dependent effective mass within the beam. This analysis may be compared to data taken on the conventional and inverted RPM experiments run on MELBA.

Solid-state HPM sources would represent significant departure from electron beam driven sources. Three different nonlinear transmission line (NLTL) sources have been explored. The three different lines all operated in different regimes of power, nonlinearity, and impedance, but are of the same basic design and operate under the same principles.

In the varactor based low voltage NLTL some general criteria for NLTL operation were discovered. First, the risetime of the pulse must be less than that of the RF period associated with the fully linear ("cold" or "zero voltage") capacitance of a single section of the NLTL for RF to be generated. Second, the RF generated by this pulse occurs at the frequency associated with the characteristic L-C frequency of a single section of the NLTL assuming saturated nonlinearity. In the low voltage line a transit time isolated measurement of the waveform exiting the line confirmed that an RF waveform could be extracted.

Low impedance ferrite inductor based NLTL circuits were constructed and tested at high power levels. These circuits followed the relatively simple scaling using characteristic L-C frequency assuming saturated nonlinearity. These circuits showed an unfavorable scaling of frequency with impedance and therefore seem to be unacceptable as a GHz frequency HPM source. Successful operation of ferrite based NLTLs by other groups using higher impedance circuits may make them useful in parallel architectures [18].

A nonlinear dielectric-based nonlinear transmission line with parallel plate geometry was constructed. The NLTL was modeled in a circuit simulation code with the inclusion of dielectric loss. The inclusion of loss in the model damps the RF oscillations that would otherwise occur after the electromagnetic shockfront. The experimental line showed the

expected nonlinear behavior as waveforms showed shockwave generation as they travel down the transmission line. The waveforms from the experimental line compare qualitatively with the circuit model with loss. Future work on this type of line should focus on using a low-loss dielectric to assure that an RF waveform is developed. The diagnostic system used in this experiment shows promise as it would allow for an experimental determination of where on the dispersion relation the device is operating. The relatively few oscillations generated using the simple L-C circuit in the NLTLs presented here could be increased by using a circuit with tunable dispersion characteristics with capacitive cross links such as in [17],[18],[50],[75].

Cell electroporation experiments comparing capacitive to conductive connection were performed [58]. The difference between these two cases involves the pulse shape seen by the cells. Although the magnitude of the electric field was 16 kV/cm in both cases, the conductively connected cells experience an electric field in one direction only, whereas, the capacitive coupled cells see an electric field that reverses direction. Bipolar pulses occurring faster than the timescale of pore formation that result from capacitive coupling to the cell suspension therefore inhibit electroporation. The cell in the conductively connected case is left with a net polarization after the pulse. The pulse shape is important when working with pulses that have durations on or faster than the timescale of bioeffects. These results suggest that electroporation using capacitive connection may require a step function pulse shape, which will be differentiated into a monopolar pulse when coupled to the sample, as opposed to the impulse which is differentiated into a bipolar pulse. Future work on this could leverage NLTL technology which can be used to generate an extremely fast risetime at

the leading edge of a long pulse. Pulses with risetimes of less than 100 ps have been generated at voltages of 90 kV using ferrite-filled coaxial lines [76]. An experiment to examine this effect could use the existing pulse generator and adjust the pulse shape by using either the existing pulse compressor, or a ferrite filled coaxial shockline. The output of the pulse shaping device could be fed into the existing tapered plate transmission line for application to cell samples. This experiment would allow for the isolation of the cause for the lack of electroporation with capacitive coupling. It would provide a direct comparison of pulse shapes, both with capacitive coupling, such that it could be determined if the effect is in fact due to the pulse shape or if it is inherent when capacitive coupling is used. The use of such capacitive coupling could allow for the electroporation of cells without the need for electrodes. For research applications this would allow for a cell sample to be electroporated without needing to transfer the sample into and out of an electrode containing cuvette. For clinical applications, capacitive coupling could allow for electrochemotheraputic treatments without the need for electrodes to be attached to the skin.

APPENDIX

DERIVATION OF EFFECTIVE MASS

Beginning with the force law for a charged particle, with $v_0 = v_\theta$ in equation (3.3).

$$\gamma v_0^2 = \frac{e}{m} Er + \frac{e}{m} B v_0 r, \tag{A.1}$$

we divide by the left hand side of (A.1) and define the parameter

$$h = \frac{eEr}{m\gamma^3 v_0^2}. \tag{A.2}$$

The force law becomes

$$1 = \gamma^2 h + (1 - \gamma^2 h). \tag{A.3}$$

Note that $\gamma^2 h$ is the fraction in the centripetal acceleration that is provided by the electric field, and the remaining fraction $(1 - \gamma^2 h)$ is provided by the $v \times B$ force. The effective particle mass is derived by considering the energy transfer equation

$$\frac{d\varepsilon}{dt} = \frac{d}{dt}(\gamma m_0 c^2) = \vec{F} \cdot \vec{v} = eE_{\theta 1} v_\theta, \tag{A.4}$$

where the energy transfer occurs through the azimuthal electric field perturbation on an electron whose motion is in the $\hat{\theta}$ direction. Equation (A.4) can be rewritten in terms of $\dot{\theta}$

$$\frac{d\varepsilon}{dt} = \frac{d\dot{\theta}/dt}{d\dot{\theta}/d\varepsilon}, \tag{A.5}$$

so that (A.4) and (A.5) combine to give

$$\frac{d\dot{\theta}}{dt} = \frac{d^2\theta}{dt^2} = \left(\frac{d\dot{\theta}}{d\varepsilon}\right) eE_{\theta 1} v_\theta. \tag{A.6}$$

In a linear theory, in the RHS of (A.6), we keep only the zeroth order azimuthal velocity, v_0, since $E_{\theta 1}$is first order. Since $\theta = \theta_0 + \theta_1 = \omega_0 t + \theta_1$, $d^2\theta/dt^2 = d^2\theta_1/dt^2$, and $d\dot{\theta}/d\varepsilon = \partial\omega_0/\partial\varepsilon$ where $\omega_0 = v_0/r$ is the equilibrium angular frequency. In terms of the azimuthal displacement from an equilibrium orbit, $\eta = r_0\theta_1$ and $d\eta = r_0 d\theta_1$, equation (A.6) can be written as

$$\frac{d^2\eta}{dt^2} = (eE_{\theta 1})\left(r_0 v_0 \frac{\partial\omega_0}{\partial\varepsilon}\right). \tag{A.7}$$

Defining an effective mass in the azimuthal direction

$$m_{eff} = \left(r_0 v_0 \frac{\partial\omega_0}{\partial\varepsilon}\right)^{-1}, \tag{A.8}$$

equation (A.7) becomes the azimuthal force law:

$$\frac{d^2\eta}{dt^2} = \frac{(eE_{\theta 1})}{m_{eff}}. \tag{A.9}$$

We rewrite $\partial\omega_0/\partial\varepsilon$

$$\frac{\partial\omega_0}{\partial\varepsilon} = \frac{\partial\omega_0/\partial r}{\partial\varepsilon/\partial r} = \frac{\partial(v_0/r)/\partial r}{\partial\varepsilon/\partial r}. \tag{A.10}$$

To get $\partial v_0/\partial r$ we take the partial derivative of the force law in equation (A.1)

$$\frac{\partial}{\partial r}\left[\gamma v_0^2 = \frac{e}{m}Er + \frac{e}{m}Bv_0 r\right]. \tag{A.11}$$

Since $E = V/r\ln(b/a)$, the term containing the electric field E goes to zero when the partial derivative is taken,

$$\frac{\partial}{\partial r}(\gamma v_0^2) = \left(\frac{e}{m}B\right)\frac{\partial}{\partial r}(v_0 r). \tag{A.12}$$

This relation, written as,

$$\gamma\frac{\partial}{\partial r}v_0^2 + v_0^2\frac{\partial}{\partial r}\gamma = \left(\frac{e}{m}B\right)\left[v_0 + r\frac{\partial}{\partial r}v_0\right], \tag{A.13}$$

allows us to find $\partial v_0/\partial r$ since $\gamma = (1 - v_0^2/c^2)^{-1/2}$, yields $\partial\gamma/\partial r = (v_0\gamma^3/c^2)\partial v_0/\partial r$ which is also in terms of $\partial v_0/\partial r$. Combining terms containing $\partial v_0/\partial r$ and rearranging gives

$$\frac{\partial v_0}{\partial r}\left(2 - \frac{eBr}{m\gamma v_0} + \frac{v_0^2}{c^2}\gamma^2\right)\gamma v_0 = \frac{eBv_0}{m}. \tag{A.14}$$

Using the relations: $eBr/m\gamma v_0 = 1 - \gamma^2 h$, $\beta_\perp = v_0/c$, and $\omega_0 = v_0/r$ the above can be rewritten

$$\frac{\partial v_0}{\partial r}(2 - (1 - \gamma^2 h) + \beta_\perp^2\gamma^2) = \omega_0(1 - \gamma^2 h). \tag{A.15}$$

Upon using the relation

$$\beta_\perp^2 = 1 - \frac{1}{\gamma^2}, \tag{A.16}$$

equation (A.15) reads

$$\frac{\partial v_0}{\partial r} = \frac{\omega_0(1 - \gamma^2 h)}{\gamma^2(1 + h)}. \tag{A.17}$$

We next obtain $\partial\omega_0/\partial r$

$$\frac{\partial \omega_0}{\partial r} = \frac{\partial}{\partial r}\left(\frac{v_0}{r}\right) = v_0 \frac{\partial}{\partial r}\left(\frac{1}{r}\right) + \frac{1}{r}\frac{\partial v_0}{\partial r}. \tag{A.18}$$

Substitution of (A.17) into (A.18), we obtain

$$\frac{\partial \omega_0}{\partial r} = -\frac{\omega_0}{r}\frac{(\beta_\perp^2 + 2h)}{(1+h)}. \tag{A.19}$$

where we have used equation (A.16). To solve for the quantity $\partial\varepsilon/\partial r$ one must remember that the total energy $\varepsilon = \varepsilon_k + \varepsilon_p$, where

$$\varepsilon_p(r) = |e| \int_a^r E_0 dr, \tag{A.20}$$

$$\varepsilon_k(r) = (\gamma_0 - 1) m_0 c^2. \tag{A.21}$$

$\partial\varepsilon/\partial r$ becomes

$$\frac{\partial \varepsilon}{\partial r} = \frac{\partial}{\partial r}[(\gamma - 1) m_0 c^2] + \frac{\partial}{\partial r}\left[|e| \int_a^r E_0 dr\right], \tag{A.22}$$

$$\frac{\partial \varepsilon}{\partial r} = m_0 c^2 \frac{\partial \gamma}{\partial r} + eE_0. \tag{A.23}$$

Using the earlier solution for $\partial\gamma/\partial r$, (cf. line after equation (A.13)) and remembering that $eE_0 r/m_0 \gamma v_0^2 = \gamma^2 h$, and $\omega_0 = v_0/r$

$$\begin{gathered} \frac{\partial \varepsilon}{\partial r} = m_0 c^2 \left(\frac{v_0 \gamma^3}{c^2}\right)\frac{\partial v_0}{\partial r} + \left(\frac{eE_0 r}{m\gamma v_0^2}\right)\left(\frac{\gamma m_0 v_0^2}{r}\right), \\ \frac{\partial \varepsilon}{\partial r} = m_0 v_0 \gamma^3 \frac{\partial v_0}{\partial r} + \omega_0 m_0 v_0 \gamma(\gamma^2 h). \end{gathered} \tag{A.24}$$

Substituting the earlier solution for $\partial v_0/\partial r$, (A.17),

$$\frac{\partial \varepsilon}{\partial r} = m_0 v_0 \gamma^3 \left(\frac{\omega_0(1 - \gamma^2 h)}{\gamma^2(1+h)}\right) + \omega_0 m_0 v_0 \gamma(\gamma^2 h), \tag{A.25}$$

$$\frac{\partial \varepsilon}{\partial r} = \omega_0 m_0 v_0 \gamma \left(\frac{1 - \gamma^2 h}{1 + h} + \gamma^2 h \right).$$

Solving for $\partial \varepsilon / \partial r$,

$$\frac{\partial \varepsilon}{\partial r} = \omega_0 m_0 v_0 \gamma \left(\frac{1 + \gamma^2 h^2}{1 + h} \right). \tag{A.26}$$

Using equations (A.19) and (A.26) for $\partial \omega_0 / \partial \varepsilon$, we have

$$\frac{\partial \omega_0}{\partial \varepsilon} = \frac{\partial \omega_0 / \partial r}{\partial \varepsilon / \partial r} = \frac{-\frac{\omega_0}{r} \frac{(\beta_\perp^2 + 2h)}{(1 + h)}}{\omega m_0 v_0 \gamma \left(\frac{1 + \gamma^2 h^2}{1 + h} \right)} = \frac{-1}{r v_0 m_0 \gamma} \left(\frac{\beta_\perp^2 + 2h}{1 + \gamma^2 h^2} \right). \tag{A.27}$$

Substituting $\partial \omega_0 / \partial \varepsilon$ into the relation for effective mass, (A.8), we have

$$m_{eff} = -m_0 \gamma \left(\frac{1 + \gamma^2 h^2}{\beta_\perp^2 + 2h} \right). \tag{A.28}$$

BIBLIOGRAPHY

[1] V.L. Granatstein and I. Alexeff, *High-power microwave sources*, Artech House, 1987.

[2] J. Benford, J.A. Swegle, and E. Schamiloglu, *High power microwaves*, CRC Press, 2007.

[3] G.S. Nusinovich, *Modern Microwave and Millimeter-Wave Power Electronics*, Wiley-IEEE Press, 2005.

[4] M.C. Wicks, "RF Tomography with Application to Ground Penetrating Radar," *2007 Conference Record of the Forty-First Asilomar Conference on Signals, Systems and Computers*, Pacific Grove, CA, USA: 2007, pp. 2017-2022.

[5] W. Brown, "The History of Power Transmission by Radio Waves," *IEEE Transactions On Microwave Theory And Techniques*, vol. 32, 1984, pp. 1230-1242.

[6] FPL, http://www.fpl.com/environment/solar/desoto.shtml.

[7] A. Kasugai, R. Minami, K. Takahashi, N. Kobayashi, and K. Sakamoto, "Long pulse operation of 170GHz ITER gyrotron by beam current control," *Fusion Engineering and Design*, vol. 81, 2006, pp. 2791-2796.

[8] S. Bhattacharya, "The standard model Higgs search at the large hadron collider," *Pramana*, vol. 69, 2008, pp. 749-752.

[9] R. Tatchyn, J. Arthur, M. Baltay, K. Bane, R. Boyce, M. Cornacchia, T. Cremer, A. Fisher, S. Hahn, M. Hernandez, G. Loew, R. Miller, W. Nelson, H. Nuhn, D. Palmer, J. Paterson, T. Raubenheimer, J. Weaver, H. Wiedemann, H. Winick, C. Pellegrini, G. Travish, E. Scharlemann, S. Caspi, W. Fawley, K. Halbach, K. Kim, R. Schlueter, M. Xie, D. Meyerhofer, R. Bonifacio, and L. DeSalvo, "Research and development toward a 4.5-1.5 angstrom linac coherent light source (LCLS) at SLAC," *Nuclear Instruments & Methods In Physics Research Section*, vol. 375, Jun. 1996, pp. 274-283.

[10] LHC_Homepage, http://lhc.web.cern.ch/lhc/.

[11] D. Sullivan, "High-Power Microwave Generation From A Virtual Cathode Oscillator (Vircator)," *IEEE Transactions On Nuclear Science*, vol. 30, 1983, pp. 3426-3428.

[12] C.D. Child, "Discharge From Hot CaO," *Physical Review (Series I)*, vol. 32, May. 1911, p. 492.

[13] I. Langmuir, "The Effect of Space Charge and Initial Velocities on the Potential Distribution and Thermionic Current between Parallel Plane Electrodes," *Physical Review*, vol. 21, Apr. 1923, p. 419.

[14] R.H. Varian and S.F. Varian, "A High Frequency Oscillator and Amplifier," *Journal of Applied Physics*, vol. 10, 1939, p. 321.

[15] V. Flyagin, A. Gaponov, M. Petelin, And V. Yulpatov, "Gyrotron," *IEEE Transactions on Microwave Theory and Techniques*, vol. 25, 1977, pp. 514-521.

[16] J.C. Slater, "Microwave Electronics," *Reviews of Modern Physics*, vol. 18, Oct. 1946, p. 441.

[17] A. Belyantsev and A. Kozyrev, "RF oscillation generated by an electromagnetic shock wave in coupled transmission lines with anomalous and normal dispersion," *Technical Physics*, vol. 46, Jul. 2001, pp. 864-867.

[18] N. Seddon, C. Spikings, and J. Dolan, "RF pulse formation in nonlinear transmission lines," *2007 IEEE Pulsed Power Conference,* vols 1-4, 2007, pp. 678-681.

[19] J. Darling and P. Smith, "High-Power Pulsed RF Extraction From Nonlinear Lumped Element Transmission Lines," *IEEE Transactions on Plasma Science*, vol. 36, Oct. 2008, pp. 2598-2603.

[20] R. Landauer, "Shock waves in nonlinear transmission lines and their effect on parametric amplification," *IBM J. Res. Dev.*, vol. 4, 1960, pp. 391-401.

[21] J. VanDevender, J. Crow, B. Epstein, D. McDaniel, C. Mendel Jr., E. Neau, J. Poukey, J. Quintenz, D. Seidel, and R. Stinnett, "Self-magnetically insulated electron flow in vacuum transmission lines," *Physica B+C*, vol. 104, Mar. 1981, pp. 167-182.

[22] M.C. Clark, B.M. Marder, and L.D. Bacon, "Magnetically insulated transmission line oscillator," *Applied Physics Letters*, vol. 52, 1988, p. 78.

[23] Y.Y. Lau, in High Power Microwave Sources, edited by V. L. Granatstein and I. Alexeff (Artech House, Norwood, 1987), Chap. 9, p. 309.

[24] Y.Y. Lau, J.W. Luginsland, K.L. Cartwright, D.H. Simon, W. Tang, B.W. Hoff, and R.M. Gilgenbach, "A re-examination of the Buneman-Hartree condition in a cylindrical smooth-bore relativistic magnetron," *Physics of Plasmas*, vol. 17, Mar. 2010, p. 3102.

[25] M. Franzi, "Private Communcation."

[26] R.M. Gilgenbach, Y.Y. Lau, D.M. French, B.W. Hoff, M. Franzi, D. Simon, and J.W. Luginsland, "Recirculating-planar-magnetrons for high power, high-frequency radiation generation," *2010 IEEE International Vacuum Electronics Conference (IVEC)*, Monterey, CA, USA: 2010, pp. 507-508.

[27] N.M. Jordan, R.M. Gilgenbach, B.W. Hoff, and Y.Y. Lau, "Metal-oxide-junction, triple point cathodes in a relativistic magnetron," *The Review of Scientific Instruments*, vol. 79, Jun. 2008, p. 064705.

[28] D. Chernin and Y.Y. Lau, "Stability of laminar electron layers," *Physics of Fluids*, vol. 27, 1984, pp. 2319-2331.

[29] B. Goplen, L. Ludeking, D. Smith, and G. Warren, "User-configurable MAGIC for electromagnetic PIC calculations," *Computer Physics Communications*, vol. 87, May. 1995, pp. 54-86.

[30] W. White, R. Gilgenbach, M. Jones, V. Neculaes, Yue Ying Lau, P. Pengvanich, N. Jordan, B. Hoff, R. Edgar, T. Spencer, and D. Price, "Radio frequency priming of a long-pulse relativistic magnetron," *IEEE Transactions on Plasma Science*, vol. 34, 2006, pp. 627-634.

[31] M. Jones, V. Neculaes, Y.Y. Lau, R. Gilgenbach, and W. White, "Cathode priming of a relativistic magnetron," *Applied Physics Letters*, vol. 85, Dec. 2004, pp. 6332-6334.

[32] B. Hoff, P. Mardahl, R. Gilgenbach, M. Haworth, D. French, Y. Lau, and M. Franzi, "Microwave window breakdown experiments and simulations on the UM/L-3 relativistic magnetron," *Review of Scientific Instruments*, vol. 80, Sep. 2009.

[33] I.D. Smith, "Induction voltage adders and the induction accelerator family," *Physical Review Special Topics - Accelerators and Beams*, vol. 7, Jun. 2004, p. 064801.

[34] M.G. Mazarakis, W.E. Fowler, K.L. LeChien, F.W. Long, M.K. Matzen, D.H. McDaniel, R.G. McKee, C.L. Olson, J.L. Porter, S.T. Rogowski, K.W. Struve, W.A. Stygar, J.R. Woodworth, A.A. Kim, V.A. Sinebryukhov, R.M. Gilgenbach, M.R. Gomez, D.M. French, Y.Y. Lau, J.C. Zier, D.M. VanDevalde, R.A. Sharpe, and K. Ward, "High-Current Linear Transformer Driver Development at Sandia National Laboratories," *IEEE Transactions on Plasma Science*, vol. 38, 2010, pp. 704-713.

[27] C. E. Nielson, A. M. Sessler, and K. R. Simon, "Proceedings of the International Conference on High-Energy Accelerators and Instrumentation" (CERN, Geneva, 1959), p. 239, A. A. Kolomenskii and A. N. Lebedev, "Proceedings of the International Conference on High-Energy Accelerators and Instrumentation" (CERN, Geneva, 1959), p. 115.

[36] R.G.E. Hutter, *Beam and wave electronics in microwave tubes*, Boston Technical Publishers, 1965.

[37] D.M. French, B.W. Hoff, Y.Y. Lau, and R.M. Gilgenbach, "Negative, positive, and infinite mass properties of a rotating electron beam," *Applied Physics Letters*, vol. 97, 2010, p. 111501.

[38] A. Peratt, C. Snell, and F. Felber, "A Particle-In-Cell Simulation of a Cyclic Beam Buncher," *IEEE Transactions on Plasma Science*, vol. 18, Jun. 1990, pp. 626-631.

[39] T. Hughes and B. Godfrey, "Instability in a Relativistic Electron Layer with a Strong Azimuthal Magnetic-Field," *Applied Physics Letters*, vol. 46, 1985, pp. 473-475.

[40] B. Godfrey and T. Hughes, "Long-Wavelength Negative Mass Instabilities in High-Current Betatrons," *Physics of Fluids*, vol. 28, 1985, pp. 669-676.

[41] G. Gisler, "Particle-In-Cell Simulations of Azimuthal Instabilities in Relativistic Electron Layers," *Physics of Fluids*, vol. 30, Jul. 1987, pp. 2199-2208.

[42] T.P. Fleming, M.R. Lambrecht, and K.L. Cartwright, "Numerical Simulations of a Relativistic Inverted Magnetron," *IEEE Transactions on Plasma Science*, vol. 38, 2010, pp. 1563-1573.

[43] R.A. Close, A. Palevsky, and G. Bekefi, "Radiation measurements from an inverted relativistic magnetron," *Journal of Applied Physics*, vol. 54, 1983, p. 4147.

[44] Y.Y. Lau, "A Unified Theory of the Diocotron, Cyclotron Maser, and Negative-Mass Instabilities," *IEEE Transactions On Electron DeviceS*, vol. 31, 1984, pp. 329-337.

[45] G. Döhler, "Peniotron interactions in gyrotrons I. Qualitative analysis," *International Journal of Electronics*, vol. 56, 1984, p. 617.

[46] B. Efron, "Bootstrap Methods: Another Look at the Jackknife," *The Annals of Statistics*, vol. 7, 1979, pp. 1-26.

[47] C.K. Birdsall and J.R. Whinnery, "Waves in an Electron Stream with General Admittance Walls," *Journal of Applied Physics*, vol. 24, 1953, p. 314.

[48] R. Freeman and A. Karbowiak, "An investigation of nonlinear transmission lines and shock waves," *J. Phys. D: Appl. Phys*, vol. 10, 1977, p. 633.

[49] H. Ikezi, J.S. DeGrassie, and J. Drake, "Soliton generation at 10 MW level in the very high frequency band," *Applied Physics Letters*, vol. 58, 1991, p. 986.

[50] A. Belyantsev and A. Kozyrev, "Influence of local dispersion on transient processes accompanying the generation of rf radiation by an electromagnetic shock wave," *Technical Physics*, vol. 43, Jan. 1998, pp. 80-85.

[51] N. Seddon and T. Bearpark, "Observation of the Inverse Doppler Effect," *Science*, vol. 302, Nov. 2003, pp. 1537-1540.

[52] G.N. Glasoe and J.V. Lebacqz, *Pulse Generators: MIT Radiation Laboratory Series #5*, Boston Technical Publishers, 1964.

[53] D. Shiffler, "Private Communication."

[54] C.W. Peters, R.L. Jaynes, Y.Y. Lau, R.M. Gilgenbach, W.J. Williams, J.M. Hochman, W.E. Cohen, J.I. Rintamaki, D.E. Vollers, and T.A. Spencer, "Time-frequency analysis of modulation of high-power microwaves by electron-beam voltage fluctuations," *Physical Review E*, vol. 58, Nov. 1998, p. 6880.

[55] Linear Technology, http://www.linear.com/designtools/software/ltspice.jsp.

[56] H. Ikezi, S.S. Wojtowicz, R.E. Waltz, and D.R. Baker, "Temporal contraction of solitons in a nonuniform transmission line," *Journal of Applied Physics*, vol. 64, Dec. 1988, pp. 6836-6838.

[57] TRS Technologies, Inc., http://www.trstechnologies.com/.

[58] D.M. French, M.D. Uhler, R.M. Gilgenbach, and Y.Y. Lau, "Conductive versus capacitive coupling for cell electroporation with nanosecond pulses," *Journal of Applied Physics*, vol. 106, 2009, p. 074701.

[59] J.C. Weaver and Y. Chizmadzhev, "Theory of electroporation: A review," *Bioelectrochemistry and Bioenergetics*, vol. 41, Dec. 1996, pp. 135-160.

[60] S. Koronkiewicz, S. Kalinowski, and K. Bryl, "Programmable chronopotentiometry as a tool for the study of electroporation and resealing of pores in bilayer lipid membranes," *Biochimica et Biophysica Acta (BBA) - Biomembranes*, vol. 1561, Apr. 2002, pp. 222-229.

[61] E. Neumann, M. Schaefer-Ridder, Y. Wang, and P.H. Hofschneider, "Gene transfer into mouse lyoma cells by electroporation in high electric fields.," *The EMBO Journal*, vol. 1, 1982, pp. 841-845.

[62] L.M. Mir, S. Orlowski, J. Belehradek, and C. Paoletti, "Electrochemotherapy potentiation of antitumour effect of bleomycin by local electric pulses," *European Journal of Cancer (Oxford, England: 1990)*, vol. 27, 1991, pp. 68-72.

[63] M. Cemazar and G. Sersa, "Electrotransfer of therapeutic molecules into tissues," *Current Opinion in Molecular Therapeutics*, vol. 9, Dec. 2007, pp. 554-562.

[64] W. Rogers, J. Merritt, J. Comeaux, C. Kuhnel, D. Moreland, D. Teltschik, J. Lucas, and M. Murphy, "Strength-duration curve for an electrically excitable tissue extended down to near 1 nanosecond," *IEEE Transactions on Plasma Science*, vol. 32, Aug. 2004, pp. 1587-1599.

[65] K. Schoenbach, B. Hargrave, R. Joshi, J. Kolb, R. Nuccitelli, C. Osgood, A. Pakhomov, M. Stacey, R. Swanson, J. White, S. Xiao, J. Zhang, S. Beebe, P. Blackmore, and E. Buescher, "Bioelectric effects of intense nanosecond pulses," *IEEE Transactions on Dielectrics and Electrical Insulation*, vol. 14, Oct. 2007, pp. 1088-1109.

[66] S. Beebe, J. White, P. Blackmore, Y. Deng, K. Somers, and K. Schoenbach, "Diverse effects of nanosecond pulsed electric fields on cells and tissues," *DNA AND CELL BIOLOGY*, vol. 22, Dec. 2003, pp. 785-796.

[67] C. Yao, Y. Mi, X. Hu, C. Li, C. Sun, J. Tang, and X. Wu, "Experiment and mechanism research of SKOV3 cancer cell apoptosis induced by nanosecond pulsed electric field," *Conference Proceedings: ... Annual International Conference of the IEEE Engineering in Medicine and Biology Society. IEEE Engineering in Medicine and Biology Society. Conference*, vol. 2008, 2008, pp. 1044-1047.

[68] A.G. Pakhomov, J.F. Kolb, J.A. White, R.P. Joshi, S. Xiao, and K.H. Schoenbach, "Long-lasting plasma membrane permeabilization in mammalian cells by nanosecond pulsed electric field (nsPEF)," *Bioelectromagnetics*, vol. 28, 2007, pp. 655-663.

[69] R. Sundararajan, "Nanosecond Electroporation: Another Look," *Molecular Biotechnology*, vol. 41, 2008, pp. 69-82.

[70] S. Beebe, P. Fox, L. Rec, K. Somers, R. Stark, and K. Schoenbach, "Nanosecond pulsed electric field (nsPEF) effects on cells and tissues: apoptosis induction and tumor growth inhibition," *IEEE Transactions on Plasma Science*, vol. 30, 2002, pp. 286-292.

[71] S.J. Beebe, P.M. Fox, L.J. Rec, L.K. Willis, and K.H. Schoenbach, "Nanosecond, high-intensity pulsed electric fields induce apoptosis in human cells," *FASEB J.*, Jun. 2003, pp. 02-0859fje.

[72] B.L. Ibey, S. Xiao, K.H. Schoenbach, M.R. Murphy, and A.G. Pakhomov, "Plasma membrane permeabilization by 60- and 600-ns electric pulses is determined by the absorbed dose," *Bioelectromagnetics*, vol. 30, 2009, pp. 92-99.

[73] K.H. Schoenbach, S. Xiao, R.P. Joshi, J. Thomas Camp, T. Heeren, J.F. Kolb, and S.J. Beebe, "The Effect of Intense Subnanosecond Electrical Pulses on Biological Cells," *IEEE Transactions on Plasma Science*, vol. 36, 2008, pp. 414-422.

[74] D.W. Jordan, M.D. Uhler, R.M. Gilgenbach, and Y.Y. Lau, "Enhancement of cancer chemotherapy in vitro by intense ultrawideband electric field pulses," *Journal of Applied Physics*, vol. 99, 2006, p. 094701.

[75] N. Seddon and E. Thornton, "A high-voltage, short-risetime pulse generator based on a ferrite pulse sharpener," *Review of Scientific Instruments*, vol. 59, Nov. 1988, pp. 2497-2498.

[76] C. Brooker, N. Altieri, G. Eastwood, R. Hoad, and J. Dolan, "90 kV 1800 A 85 ps rise time electromagnetic shock line for UWB applications," *Electronics Letters*, vol. 35, 1999, p. 2210.